

8-1-2021

Understanding Heterostructure Chemiresistive Gas Sensing at Room Temperature

Yale Wang
University of Wisconsin-Milwaukee

Follow this and additional works at: <https://dc.uwm.edu/etd>



Part of the [Materials Science and Engineering Commons](#), and the [Mechanical Engineering Commons](#)

Recommended Citation

Wang, Yale, "Understanding Heterostructure Chemiresistive Gas Sensing at Room Temperature" (2021).
Theses and Dissertations. 2848.
<https://dc.uwm.edu/etd/2848>

This Dissertation is brought to you for free and open access by UWM Digital Commons. It has been accepted for inclusion in Theses and Dissertations by an authorized administrator of UWM Digital Commons. For more information, please contact scholarlycommunicationteam-group@uwm.edu.

UNDERSTANDING HETEROSTRUCTURE
CHEMIREISTIVE GAS SENSING AT ROOM
TEMPERATURE

by
Yale Wang

A Dissertation Submitted in
Partial Fulfillment of the
Requirements for the Degree of

Doctor of Philosophy
in Engineering

at
The University of Wisconsin-Milwaukee

August 2021

ABSTRACT

UNDERSTANDING HETEROSTRUCTURE CHEMIRESISTIVE GAS SENSING AT ROOM TEMPERATURE

by

Yale Wang

The University of Wisconsin-Milwaukee, 2021
Under the Supervision of Professor Junhong Chen

Chemiresistive sensors are the most widely investigated gas sensors due to their ease in fabrication, cost-effectiveness, simplicity of operation, and offer advances in miniaturization. Up to date, typical and well-researched resistive-type sensing materials include semiconductor metal oxides, noble metals, carbon-based nanomaterials (e.g., graphene and carbon nanotubes), and conducting polymers. Gas sensors based on a single material were found difficult to meet the practical requirements for multi-sensing properties, including sensitivity, selectivity, speed of response/recovery, stability, limit of detection, and room temperature operation. Rational design through a combination of chemically or electronically dissimilar nanomaterials is an effective route to enhancing gas sensing performance. Because the chemical composition varies with position, especially at the interface between two dissimilar materials, the newly hybridized structure is defined as a heterostructure. During the past decades, there has been significant research effort in exploring the nanocomposite heterostructures for chemiresistive room-temperature gas sensors. However, sensing mechanisms for such heterostructures are still elusive

without solid analysis or direct characterization results. The objective of this dissertation study is to understand the sensing mechanisms of heterostructure-based chemiresistive gas sensors through in situ investigation and analysis under real operating conditions.

Various novel heterostructures have been developed for specific types of gas sensing, with a variety of in situ/operando techniques applied to investigate the sensing mechanisms toward different gases. Firstly, nickel oxide-tungsten oxide (NiO-WO₃) nanowire-based heterostructures with various component ratios were fabricated via a facile, sonication-based solution mixing method. The exhibited heterojunction effect is maximally observed for W3N1 (75 mol% WO₃-25 mol% NiO) and confirmed by observation of the increase in resistance due to the formation of a diode-like p-n junction at the NiO-WO₃ interface. The excellent hydrogen sulfide (H₂S) sensing performance for W3N1 is attributed to the p-n junction effect, sulfurization by H₂S (formation of tungsten sulfides (WS_{2-x}), and nickel sulfides (NiS_{1-x})), and the ideal ratio of the NiO component in the composite. The formation of reactive semi-metallic products due to sulfurization on the sensor surface was confirmed by in situ X-ray diffraction (XRD) analyses. Operando impedance measurements and resistor-capacitor (RC) equivalent circuit analyses during gas sensing experiments were performed to evaluate the effect of grain-grain boundary or the p-n junction on the sensing performance. It was found that for pure WO₃ and W3N1 samples, these contributing effects are in the same direction, resulting in a cooperative and highly sensitive performance, whereas, for other compositions, the samples exhibited competing influences, resulting in low sensitivity.

Secondly, the gold doped tin oxide/reduced graphene oxide (Au-SnO₂/rGO) ternary nanohybrid heterostructure was designed with improved room temperature hydrogen (H₂) sensing performance. The sputtered Au nanoparticles enhanced both sensitivity and recovery of the SnO₂-rGO platform. Such an enhancement was attributed to the increased surface area and the oxygen ions spillover effect of loaded Au nanoparticles. The catalytic effect of Au nanoparticles for hydrogen adsorption and desorption was then revealed through the temperature-dependent gas sensing test and the Arrhenius analysis. A better balance between sensitivity and recovery can be further achieved in the future by tuning the deposition conditions of Au nanoparticles. A prototype handheld device based on the Au-SnO₂/rGO composites was finally developed for hydrogen detection. The prototype device demonstrates the potential for real-time hydrogen monitoring. The availability of such sensors will contribute to promoting a sustainable hydrogen economy, protecting public safety, and enhancing lead-acid battery safety in a wide range of applications.

Thirdly, the nickel-doped tin oxide-reduced graphene oxide (Ni/SnO₂-rGO) ternary nanohybrid heterostructure was prepared with enhanced room temperature sulfur dioxide (SO₂) sensing performance. The Ni additives significantly improved the lower detection limit (ppb level) of the SnO₂-rGO platform. The SO₂ concentration calibration curve is well fitted by the Langmuir isotherm. The humidity effect on the sensing performance was also investigated. The results suggested that current nanohybrid materials still suffer from the humidity effect. Metal oxide nanocomposite doping enhanced the SO₂ sensing and activated the adsorption of water molecules, which diminished the sensor response to sulfur dioxide gas.

Finally, the Poly[3-(3carboxypropyl)thiophene-2,5-diyl]regioregular (PT-COOH)-GO binary nanocomposite heterostructure was prepared. The gas sensing properties were investigated toward NO₂, NH₃, SO₂, and CO. The PT-COOH based sensors exhibited tunable sensing performance through the drain voltage modulation. PT-COOH-GO sensors indicated enhanced NO₂ sensing performance with good sensitivity, recovery, and stable responses. The statistical signal analysis was conducted to obtain proof-of-concept results for gas discrimination through signal processing.

This study reveals the electronic conduction gas sensing model of multi-metal oxide -nanowires-based chemiresistive gas sensors through the combination of direct current (DC) and alternating current (AC) impedance measurements. The research also suggests that two-dimensional (2D) rGO with proper modifications can be efficient gas sensing materials toward various gaseous analytes. Combining in situ characterization and critical sensing factor analyses, results from the study will offer valuable and comprehensive insights for the rational design of superior heterostructure-based chemiresistive gas sensors.

© Copyright by Yale Wang, 2021
All Rights Reserve

TABLE OF CONTENTS

ABSTRACT.....	ii
TABLE OF CONTENTS.....	vii
LIST OF FIGURES	x
LIST OF TABLES	xvi
LIST OF ABBREVIATIONS.....	xvii
ACKNOWLEDGEMENTS.....	xx
CHAPTER 1. INTRODUCTION, LITERATURE REVIEW, AND OBJECTIVES OF RESEARCH.....	1
1.1 Introduction and Motivation.....	1
1.1.1 Sensor electrode fabrication	2
1.1.2 Gas sensing test system	3
1.2 State-of-the-art Research.....	3
1.2.1 Current in situ techniques for sensing mechanism investigation	3
1.2.1.1 Impedance analysis	6
1.2.1.2 Activation energy analysis.....	8
1.2.1.3 Operando spectroscopy.....	9
1.2.2 Heterostructure for room temperature gas sensing.....	11
1.2.2.1 Metal oxide heterostructure	11
1.2.2.2 Metal oxide-rGO heterostructure.....	12
1.2.2.3 Noble metal-metal oxide-rGO ternary nanocomposite.....	16
1.2.3 Enhancement effect of heterostructure on gas sensing.....	17
1.2.3.1 Catalytic effect.....	17
1.2.3.2 Conduction/Charge carrier transfer modulation	19
1.2.3.3 Molecular probing or sieving.....	21
1.3 Research Objectives and Outline of Thesis.....	23
CHAPTER 2. IMPEDANCE ANALYSIS ON METAL OXIDE NANOWIRES HETEROSTRUCTURE ENHANCED HYDROGEN SULFIDE SENSING EFFECT	25
2.1 Introduction	25
2.2 Experimental Method.....	29
2.2.1 Sensor fabrication.....	29
2.2.2 Gas sensing test	30
2.3 Results and Discussion.....	30
2.3.1 Characterization.....	30

2.3.2 Gas sensing results and proposed sensing mechanism	33
2.3.3 In situ characterization and impedance analysis	40
2.4 Conclusions	44
 CHAPTER 3. QUANTITATIVE ANALYSIS OF THE SYNERGISTIC EFFECT OF AU NANOPARTICLES ON TIN OXIDE-RGO NANOCOMPOSITES FOR ROOM TEMPERATURE HYDROGEN SENSING	 46
3.1 Introduction	46
3.2 Experimental Method	47
3.2.1 Material synthesis and sensor fabrication	47
3.2.2 Characterization and gas sensing test	48
3.3 Results and Discussion	49
3.3.1 Characterization	49
3.3.2 Gas sensing performance	51
3.3.3 Gas sensing mechanism investigation	54
3.4 Conclusion	59
 CHAPTER 4. TERNARY NI DOPED TIN OXIDE-RGO NANOCOMPOSITES FOR SULFUR DIOXIDE SENSING	 60
4.1 Introduction	60
4.2 Experimental Method and Results	63
4.2.1 Pure rGO gas sensors for SO ₂ sensing	63
4.2.1.1 Material synthesis and sensor fabrication	63
4.2.1.2 Electrical properties of pure rGO gas sensors	64
4.2.1.3 Gas sensing results and discussion	64
4.2.2 rGO-based binary nanocomposites gas sensors for SO ₂ sensing	67
4.2.2.1 Material synthesis and sensor fabrication	67
4.2.2.2 Sulfur dioxide sensing results and discussion	68
4.2.3 Control experiment on rGO-based binary gas sensors	70
4.2.3.1 Material synthesis and sensor fabrication	70
4.2.3.2 Characterization and discussion	71
4.2.3.3 Sulfur dioxide sensing results and discussion	75
4.2.4 SnO ₂ -rGO based ternary nanocomposites gas sensor	76
4.2.4.1 Material synthesis and sensor fabrication	76
4.2.4.2 Characterization and discussion	77
4.2.4.3 Sensing results and discussion	79
4.3 Humidity Effect on the Graphene-based Gas Sensor	82
4.3.1 Introduction and motivation	82
4.3.2 Material synthesis and sensor fabrication	82
4.3.3 Characterization and discussion	83
4.3.4 Sensing results and discussion	84
4.4 Conclusion	87

CHAPTER 5. TUNING THE GAS SENSING PERFORMANCE OF ORGRANIC POLYMER-GO NANOCOMPOSITES SENSORS THROUGH DRAIN VOLTAGE MODULATION.....	88
5.1 Introduction	88
5.1.1 Organic chemiresistive gas sensor.....	88
5.1.2 Signal processing for gas sensing application	90
5.2 Experimental Methods and Results	92
5.2.1 Material preparation and sensor fabrication	92
5.2.2 Material characterization	93
5.2.3 Gas sensing test	94
5.3 Gas Sensing Results and Discussion	95
5.3.1 PT-COOH gas sensor	95
5.3.2 PT-COOH-GO gas sensor	97
5.3.3 Statistical sensing signal analysis	101
5.4 Conclusion.....	103
CHAPTER 6. SUMMARY AND FUTURE WORK.....	104
6.1 Summary	104
6.2 Future work	106
REFERENCES.....	109
CURRICULUM VITAE.....	119

LIST OF FIGURES

Figure 1.1 Schematic of gas sensing test system used in this study.	3
Figure 1.2 In situ and operando methodology in gas sensing. ⁸ Copyright 2007 Wiley-VCH.	4
Figure 1.3 Overview of the operando techniques used by the gas sensor research. ⁹ Copyright 2017 University of Tübingen.	5
Figure 1.4 Commonly accepted sensitization mechanism of catalytic effect.	18
Figure 1.5 Proposed model for the oxygen activation and improved sensor performance on Au loaded SnO ₂ . Copyright 2016 American Chemical Society. ⁵⁸	19
Figure 2.1 (a) FESEM images and (b) X-ray diffraction spectra of (i) W, (ii) W ₃ N ₁ , (iii) W ₁ N ₁ , (iv) W ₁ N ₃ and (v) N powders. (c) O 1s and (d) Ni 2p high-resolution XPS spectra of pure WO ₃ , NiO, and NiO-WO ₃ nanoheterostructures.	32
Figure 2.2 (a) Dynamic response and recovery curve of NiO-WO ₃ heterostructures. (b) Dynamic response of the W ₃ N ₁ heterostructures to 0.2 ppm, 0.5 ppm, 1 ppm, 5 ppm, and 10 ppm H ₂ S gas at room temperature. (c) Sensitivity variation of the W ₃ N ₁ sensor as a function of H ₂ S concentration. (d) Dynamic response of W ₃ N ₁ against 10 ppm H ₂ S, CO, NH ₃ , and C ₆ H ₆ . (e) Comparative performance for W ₃ N ₁ towards 10 ppm H ₂ S, CO, C ₆ H ₆ , and NH ₃	34
Figure 2.3 Schematic illustration of the formation of the p-n junction between n-type WO ₃ and p-type NiO.	37
Figure 2.4 Schematic conduction pathway model during H ₂ S gas exposure for (a) W ₃ N ₁ and (b) W ₁ N ₃	39

Figure 2.5 Comparison of XRD peaks for samples before and after H ₂ S exposure (a) WO ₃ , (b) W3N1, (c) NiO.....	41
Figure 2.6 Impedance spectroscopy sensing plots of all samples against H ₂ S (a) WO ₃ , (b) W3N1, (c) W1N1, (d) W1N3, (e) NiO.....	42
Figure 2.7 Schematic illustration of the overall equivalent circuit (a) n-type, (b) p-type.	43
Figure 3,1 Schematic of the Au-SnO ₂ /rGO sensor device and measurement system.	48
Figure 3.2 (a) SEM image of Au-SnO ₂ /rGO sensor chip. (b) Line scan EDX data combined with SEM image of the Au-SnO ₂ /rGO sensor. (c) XRD pattern of SnO ₂ -rGO nanohybrids.	50
Figure 3.3 XPS spectra of a) Au-SnO ₂ /rGO nanohybrids. b) Sn 3d and c) Au 4f spectra of the Au-SnO ₂ /rGO nanohybrids. C 1s of d) the GO and e) the Au-SnO ₂ /rGO nanohybrids..	50
Figure 3.4 Responses to 1% H ₂ of a) rGO and SnO ₂ -rGO. b) rGO and Au-rGO. c) Au-SnO ₂ /rGO nanohybrids with different sputtered gold thickness. d) dynamic response curves of 12s sputtered Au-SnO ₂ /rGO to 100 ppm NO ₂ and 50 ppm H ₂ S. e) dynamic response curves of 12s sputtered Au-SnO ₂ /rGO to H ₂ with varying concentrations from 0.04% to 1% in 1 min. f) Calibration curves of 1 nm Au-SnO ₂ /rGO sensors to H ₂ gas.	52
Figure 3.5 SEM images of sputtered gold nanoparticles on silicon wafer with different sputtering time.	52
Figure 3.6 Schematic band diagrams of Au-SnO ₂ /rGO sensors (top figure) with the heterojunction formation at the interfaces (bottom figure).....	56

Figure 3.7 a) I-V curve and b-e) FET curves of the rGO, SnO ₂ -rGO, and Au-SnO ₂ /rGO sensors.....	56
Figure 3.8 a-b) The Arrhenius plot of $\ln d(\text{Res\%})/dt $ determined from the initial slope of the recovery cycle. Dynamic response curves of c) Au-SnO ₂ /rGO and d) SnO ₂ -rGO sensors to 1% H ₂ in the temperature range 21.5-100 °C.	57
Figure 3.9 Prototype handheld device with the demonstration results.	58
Figure 4.1 I-V curve and field-effect properties of rGO sensors.	64
Figure 4.2 FET curves of HGO samples.	64
Figure 4.3 SO ₂ sensing performance of a) 10s, b) 20s, c) 30s, and d) rGO sensor performance comparison.	65
Figure 4.4 (a) rGO sensor response upon exposure to 0.05 ppm and 0.1 ppm SO ₂ at 50°C and (b) upon exposure to a range of concentrations of SO ₂ under ambient temperatures.....	66
Figure 4.5 SO ₂ sensing curves of holey GO samples.	66
Figure 4.6 SO ₂ sensing performance of (a)SnO ₂ -rGO#1@200, (b) SnO ₂ -rGO#1@400, (c) SnO ₂ -rGO#2, and (d) NiO-rGO.....	70
Figure 4.7 I-V curves of (a). SnO ₂ -rGO and (b). NiO-rGO composites sensors.....	72
Figure 4.8 XRD patterns of (a) three SnO ₂ -rGO samples and (b) three NiO-rGO samples..	72
Figure 4.9 XPS spectra of SnO ₂ -rGO: (a) survey scan of three samples, (b) Sn 3d of SnO ₂ -rGO#Wet1, (c) C 1s of SnO ₂ -rGO#Wet1, (d) O 1s of SnO ₂ -rGO#Wet1.	74

Figure 4.10 XPS spectra of NiO-rGO: (a) survey scan of three samples, (b) C 1s of NiO-rGO#2, (c) Ni 2p of NiO-rGO#2.	75
Figure 4.11 SO ₂ sensing performance of (a)SnO ₂ -rGO#Wet1, (b) SnO ₂ -rGO#Wet2, (c) SnO ₂ -rGO#Wet3, and (d) NiO-rGO.	76
Figure 4.12 SEM images of a) pure rGO nanosheet, b) SnO ₂ -rGO, c) Ni/SnO ₂ -rGO#2, and d) Ni/SnO ₂ -rGO#1.	78
Figure 4.13 XRD patterns of a) NiSn composite before annealing, b) NiSn composite after annealing.	78
Figure 4.14 EDS spectra of Ni/SnO ₂ -rGO#1 sensors.	79
Figure 4.15 Sulfur dioxide sensing performance of a) NiO-SnO ₂ /rGO, b) Ni/SnO ₂ -rGO samples, and c) multi-cycle sensing of Ni/SnO ₂ -rGO sensor against 4 ppb SO ₂	80
Figure 4.16 Sensing response against 0.1 ppm SO ₂ and 10 ppm NH ₃ of a) SnO ₂ -rGO, and b) Ni/SnO ₂ -rGO#1 sensors.	81
Figure 4.17 a) Dynamic response curves of Ni/SnO ₂ -rGO#1 sample to SO ₂ with varying concentrations from 2 ppb to 40 ppb, b) Calibration curve of Ni/SnO ₂ -rGO#1 sensor.	81
Figure 4.18 XRD patterns of a) Ni _x Sn _y nanocomposites, b) Ni ₃ Sn ₁ nanocomposites.	83
Figure 4.19 SEM and EDS images of the three NiO/SnO ₂ nanocomposites.	84
Figure 4.20 Dynamic response curves of a) rGO against 40% RH, 60% RH and 80% RH humid air, different sensing materials against b) 40% RH, c) 80% RH humid air.	85

Figure 4.21 Humidity-dependent dynamic response curves of a) Ni1Sn1-rGO, b) Ni1Sn3-rGO.	86
Figure 5.1 Schematic diagram of the working principle of the human and artificial olfaction. ¹⁶¹ Copyright 2018 WILEY-VCH.	90
Figure 5.2 Schematic of the gas sensor signal processing.	91
Figure 5.3 a) Schematic architecture of the pure PT-COOH gas sensing device, b) Molecular structures of PT-COOH.	92
Figure 5.4 a) AFM, b-c) SEM images of the PT-COOH devices.....	93
Figure 5.5 SEM images of PT-COOH-GO devices in different scales.	94
Figure 5.6 Pure PT-COOH devices a) gate voltage-dependent output curves, b) transfer curve under -4 V drain voltage, c) drain voltage-dependent current drift curves, d) statistic bar chart of current drift.....	95
Figure 5.7 Sensing properties of pure PT-COOH against 10 ppm NO ₂ (a) and 1,000 ppm NH ₃ (b).....	96
Figure 5.8 PT-COOH-GO a) output and b) transfer curves.	97
Figure 5.9 Drain voltage-dependent baseline drift curves of PT-COOH-GO.	98
Figure 5.10 Sensing performance of PT-COOH-GO under -6 V drain voltage a) varying concentrations of NO ₂ , b) 500 ppm NH ₃ , c) 1 ppm SO ₂	99

Figure 5.11 Drain voltage-dependent 50 cycles response curves a) 1 ppm CO under -0.01 V, b) 500 ppm NH₃ under -0.5 V, c) 1 ppm NO₂ under -0.5 V, d) 1 ppm NO₂ under -6 V..... 100

Figure 5.12 PCA plots showing PT-COOH-GO nanocomposites with PC1 and PC2 using response of 3 gases (NH₃: 500ppm, NO₂: 1ppm, SO₂: 1ppm) as input data for feature calculation, a) first four features, b) first five features, and c) all six features. 102

LIST OF TABLES

Table 2.1 Corresponding Binding Energies (BE, eV) and Atomic Ratio Percentages (ARP, %) for Different Peaks of O 1s.	33
Table 2.2 Comparison of the Room-Temperature-Sensing Performance of Various Metal-Oxide-Based Gas Sensors Towards H ₂ S.	36
Table 2.3 Calculated Resistance Parameters and Their Sensitivity% in Air and H ₂ S Gas for Pure and Heterostructure Sensors.	43
Table 3.1 Quantitative Atomic ratio (%) analysis on the sputtered gold EDS results.....	53
Table 3.2 Comparison between the reported room temperature hydrogen sensors and our Au-SnO ₂ /rGO device	54
Table 4.1 Comparison of the chemiresistor sensing performance towards SO ₂	61
Table 4.2 Atomic % of three SnO ₂ -rGO samples.....	74
Table 4.3 Atomic % of Ni/SnO ₂ -rGO#1.....	79

LIST OF ABBREVIATIONS

AC	alternating current
AET	cysteamine
AFM	atomic force microscopy
ALD	atomic layer deposition
APTES	3-aminopropyltriethoxysilane
ARP	atomic ratio percentage
BE	binding energy
BET	Brunauer–Emmett–Teller
C ₆ H ₆	benzene
CH ₄	methane
CNT	carbon nanotube
CO	carbon monoxide
CO ₂	carbon dioxide
COOH	carboxylic group
CP	conducting polymer
CVD	chemical vapor deposition
DC	direct current
DFT	density functional theory
DRIFTS	diffuse reflectance infrared fourier-transform spectroscopy
EDS	energy-dispersive X-ray spectroscopy
E _F	fermi level

EIS	electrochemical impedance spectroscopy
EXAFS	extended X-ray absorption fine structure
FESEM	field emission scanning electron microscope
FET	field-effect transistor
FTIR	Fourier-transform infrared spectroscopy
GO	graphene oxide
H ₂	hydrogen
H ₂ S	hydrogen sulfide
HCHO	formaldehyde
HMDS	bis(trimethylsilyl)amine
LOD	limit of detection
NH ₃	ammonia
NO ₂	nitrogen dioxide
NP	nanoparticle
P3CT	poly[3-(6-carboxyhexyl)thiophene-2,5-diyl]
PANI	polyaniline
PC	principal component
PCA	principal component analysis
PDDA	polydiallyldimethylammonium chloride
PT	polythiophene
PTFE	polytetrafluoroethylene
QD	quantum dot
RGO	reduced graphene oxide

RT	room temperature
SO ₂	sulfur dioxide
UHV	ultrahigh vacuum
UV	ultraviolet
V ₂ O ₅	vanadium pentoxide
WO ₃	tungsten oxide
WS ₂	tungsten disulfide
XANES	X-ray absorption near edge structure
XAS	X-ray absorption spectroscopy
XPS	X-ray photoelectron spectrometer
XRD	X-ray diffraction

ACKNOWLEDGEMENTS

I would like first to acknowledge my advisor, Prof. Junhong Chen, for his considerable guidance and patience during my Ph.D. study at the University of Wisconsin-Milwaukee. Being his student in the past five years has been a privilege, and I would like to extend my thanks for everything he did for me. His insightful feedback pushed me to sharpen my thinking and brought my work to a higher level. It has been a wonderful experience to work and study in his group.

I would like to thank my colleagues from my internship at NanoAffix for their excellent collaboration and kind help. I would particularly like to single out the PI of the project I worked on, Dr. James Hill. I thank him for his patient support and for guiding all the experimental conditions to further my research.

I would like to acknowledge the financial support from the U.S. National Science Foundation (IIP-1701203 and CBET-1606057), U.S. Environmental Protection Agency (68HERC20C0031), and National Institute of Environmental Health Sciences (R44ES028656).

My sincere thanks go to my thesis committee members Dr. Deyang Qu, Dr. Benjamin Church, Dr. Yongjin Sung, and Dr. James Hill, for kindly accepting my invitation and all the valuable comments and questions on my dissertation study. I also would like to thank many mentors I've had along my journey: Dr. Shun Mao, Dr. Haihui Pu, and Dr. Arnab Maity for the initial learning of nanomaterial gas sensing, Dr. Xiaoru Guo and Xiaoyu Sui for the assistance of nanomaterial synthesis and characterizations, Dr. H. A. Owen for technical support with the SEM analyses, Dr. S. E. Hardcastle for technical support with the XRD, Raman characterizations and XPS analyses, Dr. Hyun-June Jang for the initial learning of organic materials and organic field-effect transistors, and Xin Chen for the assistance of signal processing. I would also like to thank all the other members of my research group for their help. In the meantime, I really would like to express my

appreciation to Dr. Johnson and Dr. Wahlen from UWM University Counseling Center. I could not have reached this step without their care in patience. Also, I would like to thank my parents for their love and support; they are always standing by me throughout my life.

CHAPTER 1. INTRODUCTION, LITERATURE REVIEW, AND OBJECTIVES OF RESEARCH

1.1 Introduction and Motivation

An electrically transduced gas sensor generates the electrical sensing signal through interfacial interactions between the sensing material and the gas analyte. In chemiresistive gas sensors, a semiconductor sensing material is deposited across two or more electrodes, and the sensitivity is measured by the change in the electrical resistance or current of the material in the presence of the analyte gas. The resistance of the material may increase or decrease upon exposure to the gas depending on the dominant charge carrier and the type of gas interacting with the material interface. The advantages of chemiresistors include ease in fabrication, cost-effectiveness, simplicity of operation, and also offer advances in miniaturization.¹ Up to date, typical and well-researched resistive-type sensing materials include semiconductor metal oxides, noble metals, carbon-based nanomaterials (e.g., graphene and carbon nanotubes), and conducting polymers. Pure unitary metal oxide gas sensors suffer from the high operating temperature and poor cross-sensitivity toward various interfering gases. The sensitivity and stability of pure carbon-based nanomaterials were inadequate. The sensors based on pure noble metals are not scalable for mass application due to the high cost and the scarcity nature. The aging effect of the pure conducting polymer makes the long-term stability of the resulting sensor is also rather unsatisfactory. To resolve the problems mentioned above, the introduction of secondary materials was proved effective to achieve satisfactory sensing performance. Since the chemical composition varies with position, especially at the interface between these two materials, the newly formed structure was defined as heterostructure.²

During the past decades, there has been significant research effort in exploring the nanocomposites heterostructure for chemiresistive room-temperature gas sensors. However, most of the sensing mechanisms of such heterostructures remain elusive without solid analysis or direct characterization results. In situ or operando experiments are needed to explore these sensing mechanisms.

Ultrahigh Vacuum (UHV) level is required in the surface science approach to maintaining a clean and well-characterized interface of known concentration and structure.³ However, this could not be correlated with the real operating ambient of gas sensors. Temperature and humidity are two critical factors in the sensor operating environment that could influence the sensing performance significantly. Analysis of these two factors also could assist us in obtaining a more comprehensive understanding of the sensor under real operating conditions.

1.1.1 Sensor electrode fabrication

The general fabrication process for the gold interdigitated electrodes used in this study is as follows. The wafer was cleaned via oxygen plasma treatment and coated with bis(trimethylsilyl)amine (HMDS) in the primer oven. The photoresist was spin-coated onto the wafer surface. Subsequently, the wafer was exposed to the laser writer with the predefined sensor pattern in the program and immersed in the diluted developer solution to remove the extra photoresist. Gold was deposited onto the developed wafer through the Kurt J. Lesker Electron Beam Deposition System. The gold interdigitated electrode was obtained after immersing in the Remover 1165 solution and the excess gold lift-off process.

1.1.2 Gas sensing test system

Figure 1.1 indicates the schematic of the gas sensing test system used in this dissertation research. The mass flow controllers are connected to a personal computer and modulated through the LABVIEW program. Different humidity levels will be achieved through the different mixing ratios between the dry and the wet carrier gas flow. A ceramic heating pad and a related digital controller were integrated into the test system. We could test the sensors under different temperature levels from room temperature to above 100 °C. Before sensing measurement, the humidity and temperature of the total airflow (500 sccm) in the sensing chamber were checked via a hygrometer/thermometer (VWR Traceable Hygrometer).

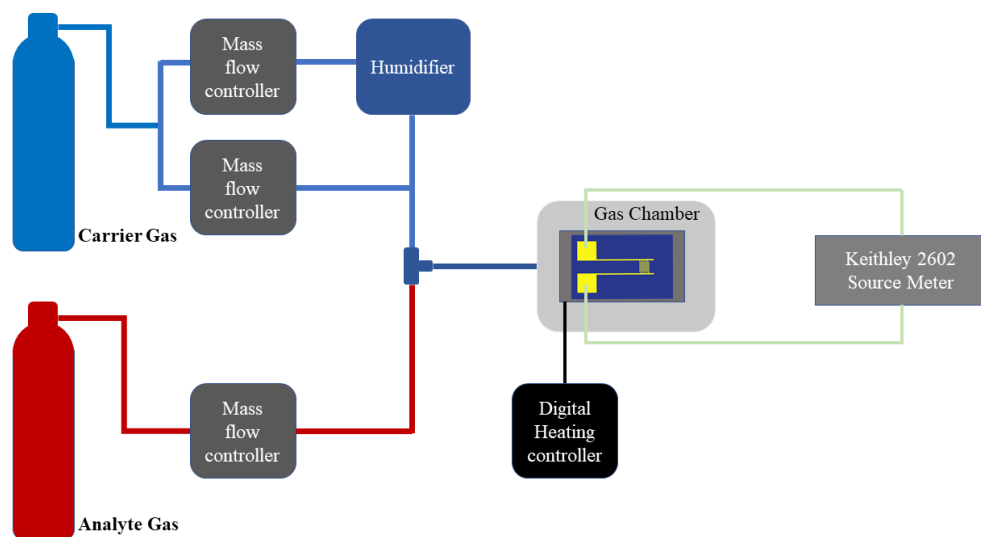


Figure 1.1 Schematic of gas sensing test system used in this study.

1.2 State-of-the-art Research

1.2.1 Current in situ techniques for sensing mechanism investigation

The terms “in situ” and “operando” were derived from the field of heterogeneous catalysis.⁴⁻⁶

Miguel A. Bañares named the methodology in order to specifically capture the idea of observing

a catalyst under actual working conditions.⁷ As shown in Figure 1.2, in situ and operando methodology are not related to any specific characterization or measurement techniques. They are associated with the requirement of the operating conditions of each technique. In situ experiment means the measurement needs to be conducted under the same working environment as the operating sensors. However, the gas sensing performance of these materials may be characterized in a separate experiment. The operating conditions of operando experiment are more restricted than in situ. Operando experiment on gas sensing materials means the characterization of sensors is coupled simultaneously with the measurement of gas sensing performance.

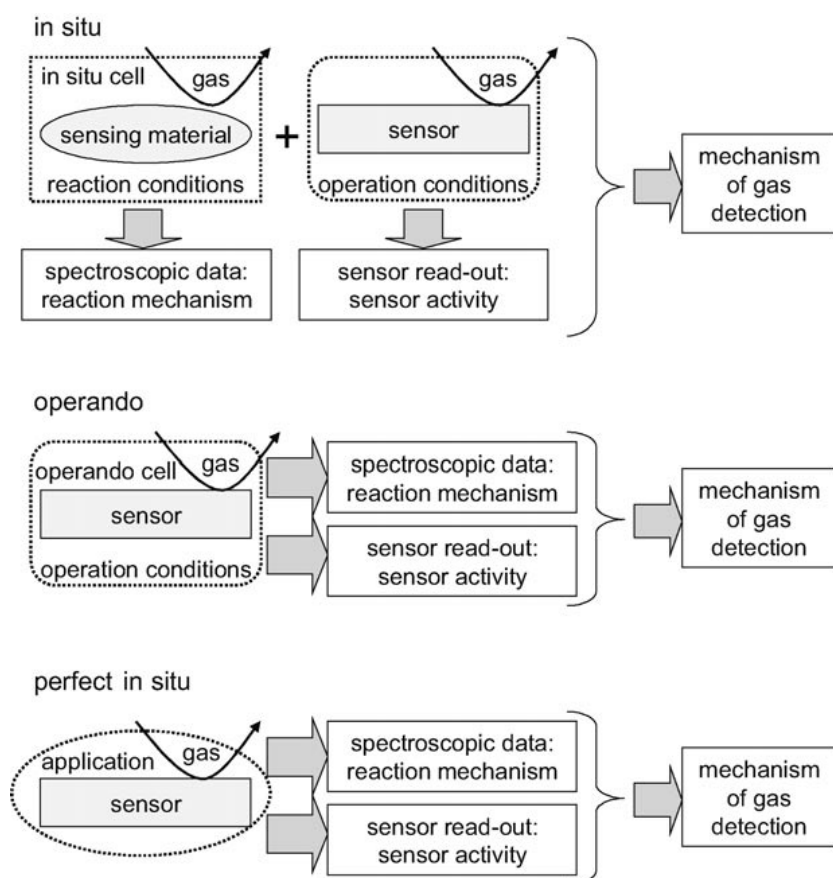


Figure 1.2 In situ and operando methodology in gas sensing.⁸ Copyright 2007 Wiley-VCH.

The operando methodology on gas sensor devices attempts to correlate the sensing performance with the chemical or electrical characterization data acquired under the same conditions on the

same sample. The ideal situation for gas sensing mechanism investigation is four types of information, including I. gas-phase reaction products, II. species adsorbed on the surface, III. changes in the oxide surface and interface between sensing material and electrode, and IV. sensing performance was obtained simultaneously.⁸

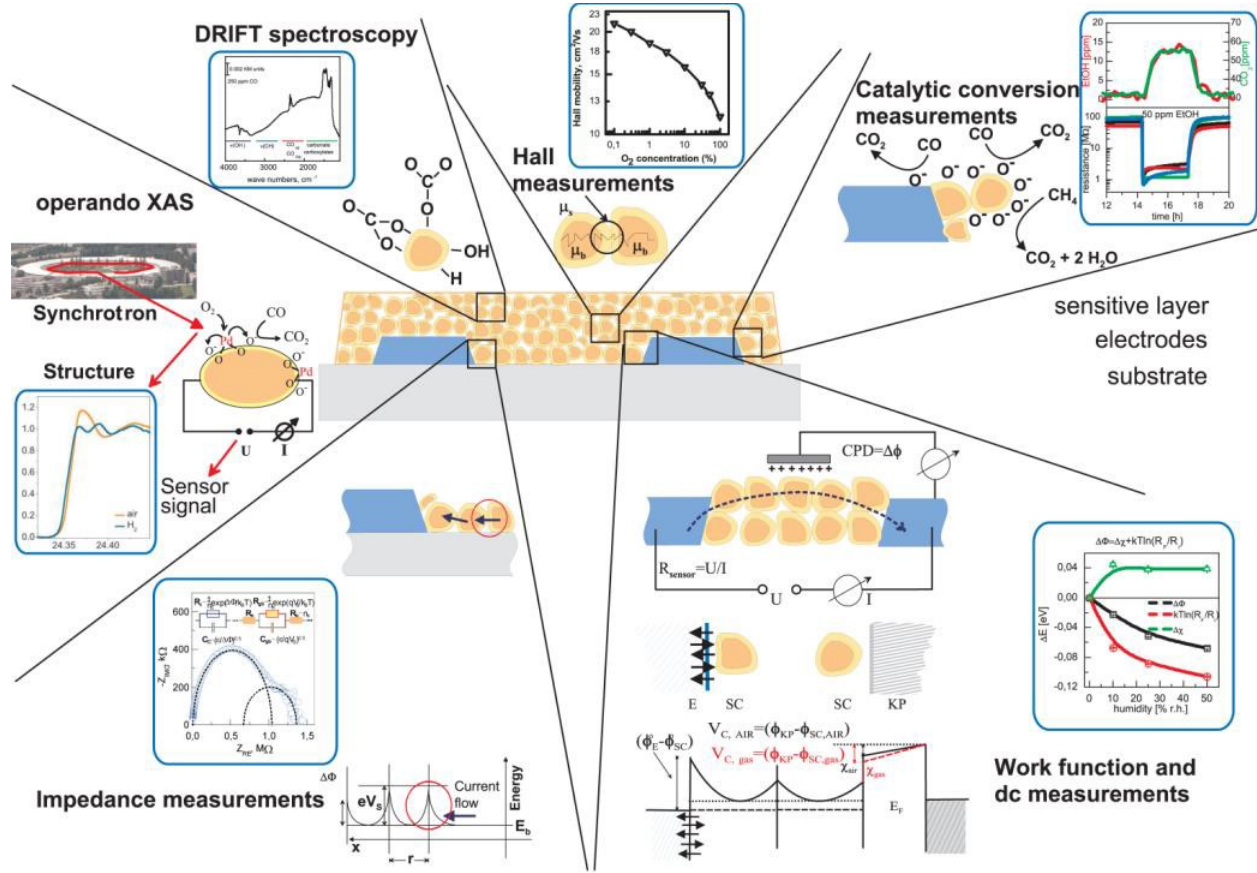


Figure 1.3 Overview of the operando techniques used by the gas sensor research.⁹ Copyright 2017 University of Tübingen.

Figure 1.3 illustrated an overview of the operando techniques applied in gas sensing investigation. Type I information could be acquired through online gas analysis, such as catalytic conversion measurement. Operando spectroscopy tools such as X-ray Adsorption Spectroscopy (XAS), Diffuse Reflectance Infrared Fourier-Transform Spectroscopy (DRIFTS) were applied to

investigate surface species and functional groups investigation. The information of the electrical charges in the material surface or heterostructure interface could be demonstrated through impedance measurements. DC measurements were conducted to research the gas sensing performance. However, it is quite hard to obtain these four types of information simultaneously. A detailed introduction of these techniques will be described next.

1.2.1.1 Impedance analysis

The interfaces within the heterostructures provide the critical modulation effect on chemiresistive gas sensing properties. Impedance spectroscopy is a useful method of investigating the electrical properties of materials and their interfaces.¹⁰ The most common method of relating the impedance analysis results to the electronic behavior of the physics system is the equivalent circuit method.¹¹ For example, single nanowires or mechanically mixed nanowires with clear interfaces are quite suitable for impedance spectroscopy analysis to reveal the conduction mechanism.

Impedance analysis revealed that the contributing resistive components inside the heterostructures from grain, grain boundary, p-n junction, and metallic species could be either cooperating or compensating, depending on the specific molar ratio of individual oxides and the overall conduction nature (p/n type) of the oxides. It is argued that by selecting a specific optimized molar ratio between constituent WO_3 and NiO nanorods, it is possible to minimize the compensating conduction components (decreasing response) and maximize the cooperating conduction (enhancing response) to develop a room-temperature, high-performance, alarm-based hydrogen sulfide (H_2S) gas detector. Balasubramani et al. applied electrochemical impedance spectroscopy (EIS) to measure the H_2S gas response of the fabricated reduced graphene oxide-zinc oxide (rGO-

ZnO) composites sensors.¹² Nyquist plot indicated that the grain boundary resistance plays a major role in gas-sensing characteristics.

Suresh Kumar and his group reported the H₂S gas sensor based on the manganese-doped zinc oxide (Mn-doped ZnO) spin-coated films.¹³ Electrochemical impedance was recorded with a frequency range from high to low (1 MHz to 1 Hz) and 10 mV sinus amplitude and without dc bias. The equivalent circuit consists of $R_1 + R_2/C_2 + R_3/C_3$. Where the R_1 represents a resistance between sensing films and silver electrode, R_2 , C_2 represents respective grain bulk resistance and capacitance, R_3/C_3 described as respective resistance and capacitance of grain boundaries between Mn/ZnO grains. The fitted values were reported with respect to concentrations of H₂S gas, and this clearly indicates the decrease of R_1 , R_2 , and R_3 with the increase in C_1 , C_2 , C_3 , and particularly R_2 compared with R_1 and R_3 values drastically decreased with the increase in the concentration of H₂S. This signifies that grain boundary resistance values are slightly decreased when compared to grain bulk and resistance between the silver electrode and sensing films. They also investigated the H₂S sensing properties of the Mn-doped SnO₂ nanoparticles (NPs) through impedance spectroscopy. They concluded that grain boundary potential barrier height decreases with the increase in the concentration of H₂S as conformed from the imaginary part of the impedance.¹⁴

Al-Hardan et al. synthesized chromium (Cr)-doped ZnO for oxygen gas sensing application. The sensing mechanism was investigated using impedance spectroscopy.¹⁵ The single semicircle with a center nearly on the x-axis was observed. This behavior led to a distinguished single relaxation time τ , that could be estimated from the maximum height of the impedance arc where $\tau\omega_{\max} = RC\omega_{\max}$ (with $\omega_{\max} = 2\pi f_{\max}$)¹⁰. Navale and his group explored the interaction of nitrogen dioxide (NO₂) gas molecules with hierarchical nanostructured ZnO sensors through an electrochemical impedance spectroscopy measurement by Navale and his group.¹⁶ The reported equivalent circuit

consists of bulk resistance (R1), capacitance (C1), grain boundary resistance (R2), and capacitance (C2). The results highlighted an interaction of gases with adsorbed oxygen at grain boundaries which is enhanced by the drift of ionic species. This enhancement in interaction leads to the observation of an inverted Cole-Cole plot.

The conduction mechanisms of the single and multiple SnO₂ nanowire-based sensors were studied by Schipani's group.¹⁷ The equivalent circuit was simplified by removing the capacitor element as the capacitance is around 0.01 pF, and the substrate is represented by constant phase elements (CPE) at the bottom. It was concluded that the junctions between nanowires had a larger contribution toward the resistance change than the conduction channel width modulation in the nanowires themselves for multiple nanowire sensors. EIS has been playing a critical role in investigating the sensing and conduction mechanism of toxic gas sensors through insights distinguishing responsible electrical components. Caution should be exercised in selecting the typical equivalent circuit model for the data produced for the simple reason that the "best fit" condition alone cannot fit the experimental measurements. It must physically make sense of what is already known for the material used and ideally modeled using the appropriate mathematical model.¹⁸

1.2.1.2 Activation energy analysis

The activation energy is generally referring to the widely used Arrhenius equation,

$$k = A \cdot \exp \left(-\frac{E_a}{RT} \right)$$

where k is the rate constant of an activated process of any kind, A is the high-temperature limit of k , called the pre-exponential factor, E_a is the activation energy, R is the gas constant, and T is the absolute temperature.¹⁹ The activation energies in chemical kinetics were typically determined by

the Arrhenius plot, which displays the logarithm of a reaction rate constant against the reciprocal of the temperature.²⁰

The activation energy analysis has been applied to gas sensing mechanism investigation since the last decade. The kinetics of indium oxides (In_2O_3)-based thin film gas sensor response to reducing and oxidizing gases were analyzed by Korotcenkov and his group. Through the activation extraction, it was concluded that water and oxygen adsorption/desorption processes are the main factors controlling the rate of response and recovery of the In_2O_3 gas sensors.²¹

Majumder et al. synthesized the magnesium zinc ferrite NPs and investigated the gas sensing properties. The enhanced response/recovery properties of the macro-porous region compared with mesoporous structures were revealed through response/recovery Arrhenius plots analysis. The results indicated the different chemisorbed oxygen species within these two different adsorption sites.²² Weiller et al. reported a facile method for preparing useful chemical sensors from chemically derived graphene.²³ They determined the activation energy of sensor recovery from the initial slope of the off cycle.

Ural and his group fabricated palladium (Pd)-functionalized multi-layer graphene nanoribbon devices for hydrogen sensing. The activation energy of hydrogen desorption was extracted through the Arrhenius analysis.²⁴ The dominant recovery mechanism could be attributed to the desorption of hydrogen from Pd NPs.

1.2.1.3 Operando spectroscopy

The drastic developments in in-situ and operando characterization techniques were marked in the last decades. Up to date, various spectroscopy techniques were modified for the operando study of

chemical information related to gas sensing. XAS and DRIFTS are the most typical spectroscopy techniques developed for operando gas sensor research.

X-ray absorption spectroscopy (XAS) is one of the most powerful methods characterizing the structure and the electronic properties of samples. It is quite useful for monitoring the chemical reactivity of functional surface additives, including noble metals.⁸ The X-ray adsorption spectrum of a solid with a fine structure is normally separated into two parts: The X-ray Absorption Near Edge Structure (XANES) and the Extended X-ray Absorption Fine Structure (EXAFS). The XANES spectra typically illustrate the oxidation state of the absorbing element and the local geometric structure of the materials. The EXAFS provides information on the structure around the absorbing atoms.⁹

The role of Au additives in SnO₂-based thick film gas sensors was revealed through a combination of operando spectroscopic and phenomenological experiments.²⁵ The XANES results indicated that Au is in the metallic state without any change upon exposure to CO and H₂ in air. These findings illustrated a different enhancement effect of Au-SnO₂ to the Pd or Pt additives.

Reflection at surfaces includes two types of reflection: specular reflection and diffuse reflectance. Diffuse reflectance will be the dominant process for the individual grains on a layer that are small with respect to the wavelength of the radiation.⁹ Diffuse reflectance infrared Fourier transform spectroscopy (DRIFTS) enables operando measurements on SMOX-based gas sensor and could be applied to the heated sensing element, which provides the advantages over Fourier-transform infrared spectroscopy (FTIR).

A surface vacancy-based reception model of undoped SnO₂ was proposed by using the operando DRIFTS and isotopically labeled gases.²⁶ The oxygen ions at specific surface sites were removed

upon exposure to reducing gases (CO , H_2 , H_2O). Different surface terminations were found from the SnO_2 prepared under different calcination temperatures.

1.2.2 Heterostructure for room temperature gas sensing

The physical interface between two dissimilar materials with different bandgap and work-function values is often referred to as a heterojunction. The dissimilar of the Fermi levels within the interfaces generally will cause charge transfer and formation of a charge carrier depletion/accumulation layer. Depending on the carrier type (n/p type), a composite heterojunction can be formed with similar types (n-n, p-p) or dissimilar types (n-p). Once the p-n junction is formed at the connecting boundary of the p-type and n-type metal oxide grains, the different bandgap of the two metal oxides will induce the band to bend to equalize the Fermi level, and a depletion layer will be formed due to the mutual charge transfer. This will decrease the width of the charge conduction channel and increase the potential barrier between the two grains. Thus, a larger change in resistance occurs in the presence of gases, thereby showing enhanced sensitivity.

1.2.2.1 Metal oxide heterostructure

Semiconductor metal oxides-based (SMOX) resistive-type sensors are widely applied in many applications, such as environmental monitoring, energy storage/transportation, food industry, and public security due to high sensitivity and low cost. To improve the selectivity and other sensing performances of the traditional SMOs gas sensors, the combination of different metal oxides to form heterostructures was proposed in the last decades.²⁷

Yang et al. prepared iron oxide (Fe_2O_3)- ZnO nanocomposites via a sol-gel method.²⁸ The room temperature ammonia (NH_3) sensing properties were investigated with different compositions Fe:

Zn. The optimal sensor with Fe: Zn = 2% indicated superior response and selectivity. The enhancement was attributed to the promotion of the adsorption of the NH_3 molecules resulting from the addition of Fe_2O_3 nanoparticles.

Patil and co-workers demonstrated the sensitivity NH_3 sensors based on the chromium oxide (Cr_2O_3)-ZnO thick film at room temperature. They found the sensitivity was improved after Cr_2O_3 decoration via the solution dipping method. The sensor also indicated fast response and recovery in less than 100 seconds.

SnO_2 -ZnO core-shell nanofibers were synthesized by Kim et al. through a novel two-step method with the combination of electrospinning and atomic layer deposition (ALD) technique. The sensing properties to NO_2 were investigated at room temperature. The improved sensitivity and dynamic repeatability were attributed to the combination of homo- and hetero-interfaces formed at the junctions.²⁹

Hu and his group fabricated the acetone sensors based on the branch-like vanadium oxide (VO_2)@ZnO hierarchical heterostructures.³⁰ The sensors exhibited significant and fast response and excellent selectivity to acetone. The superior sensing performance was contributed from the electrical modulation at the hetero-interfaces and the superior surface area from the hierarchical structures.

1.2.2.2 Metal oxide-rGO heterostructure

Two-dimensional nanomaterials are promising chemiresistive host materials due to their good compatibility with modern electronic devices and high surface area. Graphene is one of the typical 2D materials with an atomically thin single layer of carbon atoms covalently bound in a honeycomb lattice and the basic building block of graphite.³¹ The extreme single gas molecule

sensitivity and excellent electronic signal transduction property (high carrier mobility and high signal-to-noise ratio) make pure graphene a promising electrical sensing material for gas sensing application.³² Reduced graphene oxide (rGO) was considered as an alternative candidate p-type semiconductor to pure graphene with more ease of mass production for gas sensing. In contrast to graphene, the presence of surface functional groups such as carboxyl, epoxy, and hydroxyl has been taken as the enhancement factor for analyte gas molecule adsorption.^{33, 34} Furthermore, these groups also make rGO a versatile platform for nanocomposite synthesis in combination with a variety of semiconducting metal oxides.³⁵

Tin oxide (SnO_2) is one of the most widely investigated n-type semiconductor nanomaterials for gas sensing application in the last several decades. Chen and his group investigated the gas sensing properties of rGO nanosheets decorated with SnO_2 nanocrystals.³⁶ This novel hybrid platform showed enhanced sensitivity and selectivity to NO_2 gas at room temperature, indicating the promise in tuning the sensitivity and selectivity of rGO-based gas sensors. Zhang et al. prepared the SnO_2 NPs-rGO nanocomposites through a facile hydrothermal method.³⁷ The gas sensors based on the nanocomposites showed significant enhancement in sensitivity and high response speed against NO_2 at low temperature (50 °C). Through the I-V curve characterization, the enhanced sensing properties were attributed to the heterojunction formed between SnO_2 and rGO interfaces. The initial conductivity of the devices was reduced by introducing SnO_2 NPs, which leads to a larger potential variation induced by gas analyte adsorption. Zhang and his group also conducted a systematical comparative study on the NO_2 sensing properties of three SnO_2 NPs-rGO hybrids prepared via different assembly methods.³⁸ SnO_2 NPs-rGO prepared by a two-step hydrothermal treatment indicated higher and faster response behavior compared with the other two hybrids. The comprehensive characterization results correlated the sensing behavior with the microstructures of

materials. The possible reasons for different sensing performances were related to the number of oxygen vacancies, distribution uniformity of SnO₂ NPs, and porous structure. Gupta et al. investigated the sulfur dioxide (SO₂) sensing properties of bare SnO₂, rGO-SnO₂, and multi-wall carbon nanotubes (MWCNTs)-SnO₂ nanocomposites.³⁹ RGO-SnO₂ nanocomposite sensors indicated the best sensing response over the other two types of materials at 60 °C. The corresponding higher sensitivity of rGO-SnO₂ compared to MWCNTs-SnO₂ was related to the larger surface of the 2D rGO nanosheet provide for the SnO₂ NPs distribution.

Zinc oxide (ZnO), as a typical n-type semiconductor, is broadly employed in chemiresistive gas sensing applications. It has merits with excellent sensing response, easy fabrication, non-toxic, and good thermal and chemical stability.⁴⁰ One of the earliest ZnO-rGO based gas sensors was reported by Singh et al.⁴¹ They synthesized the ZnO-rGO via a single-step hydrothermal method and studied the gas sensing performance against carbon monoxide (CO), NH₃, and nitric oxide (NO). The net sensing mechanism was proposed as the combination of the gas molecules' percolation and adsorbed gas molecules modulation on ZnO surface and ZnO-rGO interfaces. Deng and his group demonstrated room temperature formaldehyde (HCHO) sensors based on ZnO quantum dots (QDs) decorated graphene nanocomposites.⁴² The sensitivity of the ZnO QDs/graphene composite sensor is four times higher than the pure graphene against 100 parts per million (ppm) HCHO room temperature. Therefore, the synergistic effect of graphene and ZnO was attributed to the enhancement. The proposed intermediate product surface formate species (-HCOO⁻) was confirmed by DRIFT spectra. Komarneni et al. synthesized ultrathin ZnO nanorods/rGO nanocomposites by a two-step additive-free solution-based method. The optimal sensor based on the nanocomposites showed a higher and faster response to ppm-level of NO₂ at room temperature. The photoluminescence (PL) spectra and the X-ray photoelectron spectrometer (XPS) results

clarified the strong electronic interaction between ZnO and rGO. The excellent sensing performance was suggested from the interfacial electron transfer through band energy alignment. Tungsten oxide (WO_3) has also attracted considerable research interest in gas sensing application as a typical n-type semiconductor. Peng and co-workers investigated the NO_2 gas sensing properties of the rGO/ WO_3 nanocomposite at room temperature.⁴³ The superior n-type sensing response corresponds to the few rGO additions to the WO_3 film. Brunauer–Emmett–Teller (BET) analysis results clarified the improvement was not correlated with surface morphology. The proposed sensing mechanism of the optimal rGO/ WO_3 sensors was attributed to the formation of an extra conductive path by the embedded rGO. A highly selective NH_3 gas sensor based on rGO/ WO_3 nanocomposite was reported by Mangalaraj et al.⁴⁴ RGO was introduced with WO_3 through a simple ultrasonication method. Increased surface area and porous structure contributed to the improved response. The enhanced selectivity was attributed to the p-n junction modulation. Besides the aforementioned three well-researched semiconductor materials, the gas sensing properties of other typical semiconductor metal oxides combined with rGO were investigated. RGO-conjugated copper oxide (Cu_2O) nanowire mesocrystals were synthesized via nonclassical crystallization under hydrothermal conditions by Sow et al.⁴⁵ The typical three-dimensional (3D) nanowire mesocrystals structure was advantageous for the improved NO_2 sensitivity and detection limit. Zeng et al. reported room temperature NO_2 gas sensors with high sensitivity and a fast recovery based on the rGO-Nickel oxide (NiO) nanocomposites.⁴⁶ The accelerated recovery rate was proposed as the combination of the higher electron mobility of rGO and the effective electron transfer between NiO and rGO. The room temperature NH_3 sensing performance of rGO decorated titanium dioxide (TiO_2) was investigated by Li et al.⁴⁷ The as-synthesized rGO- TiO_2 nanocomposites indicated good sensitivity and superior selectivity to NH_3 . However, the speed of

response/recovery was sluggish. The excellent selectivity was explained by the preferential adsorption of the acidic titania surface to base ammonia and the p-n junction between rGO and TiO_2 .

1.2.2.3 Noble metal-metal oxide-rGO ternary nanocomposite

Noble metals such as Pd, platinum (Pt), and Au were researched as effective dopants for gas sensing due to well-known catalytic activities. They can enhance the gas sensing performance through analyte gas molecule adsorption or dissociation facilitation or charge carrier transfer modulation.⁴⁸ Metal oxide/graphene binary nanocomposites were proved as superior platforms for room temperature gas sensing. The combination of noble metal clusters with the metal oxide/graphene platforms indicates promising room temperature sensing properties due to the aforementioned gas-phase activities of noble metals.

Yang et al. reported novel room temperature NH_3 gas sensors based on the Pd/ SnO_2 /rGO ternary nanocomposite.⁴⁹ The sensor indicated a high and steady response to a low concentration of NH_3 . The enhanced sensing mechanism of this ternary nanocomposite sensor was explained as the electrical conduction modulation. The Pd/ SnO_2 /rGO ternary nanocomposite was investigated for hydrogen sensing by Peng and his group.⁵⁰ They compared the hydrogen sensing performance of Pd/rGO and Pd/ SnO_2 /rGO ternary nanocomposites. The sensor based on the ternary nanocomposite showed an improved response and good selectivity at room temperature. The sensing mechanism was described as the catalytic dissociation effect of Pd to hydrogen gas and the formation of p-n junctions between SnO_2 and rGO.

Zhang et al. demonstrated a hydrogen sensor based on the Pd-ZnO-rGO ternary hybrid.⁵¹ They investigated the hydrogen sensing properties with concentrations from 1 part-per-billion (ppb) to

500 ppm. The sensor indicated good response/recovery characteristics at the optimal temperature 50 °C. The hydrogen sensing mechanism was proposed as the synergistic effect of the ternary hybrid and the charge depletion layer modulation.

Varma and Jyoti synthesized silver-copper oxide/reduced graphene oxide (Ag-CuO/rGO) nanocomposite via the hydrothermal method and fabricated the related sensor by a drop-casting method.⁵² They investigated the NO₂ sensing properties at various operating temperatures. The Ag-CuO/rGO based sensor indicated optimal NO₂ sensing performance at room temperature. The sensing mechanism within the Ag-CuO/rGO devices was attributed to three main factors. The benefits from the high surface area of CuO for gas sensing were considered as the first factor. Second, the formation of heterojunctions between CuO and rGO can also facilitate the response. Last, the enhanced response of this ternary hybrid sensor may be due to the ionized oxygen spillover effect induced by the Ag catalyst.

1.2.3 Enhancement effect of heterostructure on gas sensing

1.2.3.1 Catalytic effect

The catalytic effect of heterostructures is mainly attributed to high sensitivity and fast response or recovery via chemical or electrical sensitization. The rational design of this type of heterostructure is based on the concept from catalysis. The contact between loaded catalysts and gas molecules is critically associated with the structure of the host materials and the distribution of the catalyst nanocrystals. The large, exposed surface area makes a gas diffusion-favored structure preferential.

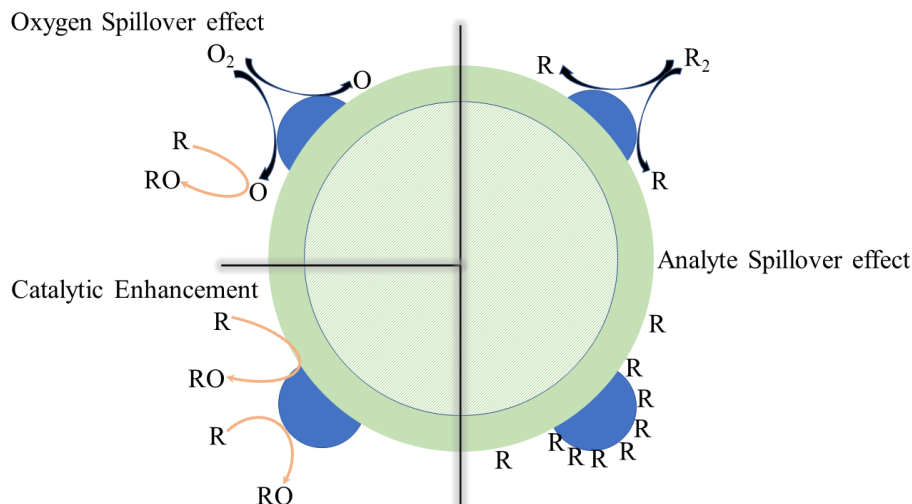


Figure 1.4 Commonly accepted sensitization mechanism of catalytic effect.

Catalytic effects stem from the dopant normally associated with a spillover effect on the surface of the catalysts or interface between the catalysts and host materials (Figure 1.4). The ionization of the oxygen molecules (O_x^-) in the ambient condition is widely recognized as the initial steps of the sensing pathway associated with metal oxide-based sensing materials. The oxygen molecules were found preferentially adsorbed and dissociated on the Ag catalyst in Ag-CuO nanocomposites at room temperature.⁵² The ionized oxygen species were spilled over to CuO surface and facilitated the charge transfer once the analyte gases were injected. This oxygen spillover effect was proved by the XPS results, where the oxygen-deficient region was effectively increased with Ag incorporation. The oxygen spillover effect was also proposed on Au loaded SnO_2 for carbon monoxide sensing, as shown in Figure 1.5 The whole responding process consists of three fundamental steps: (i) molecular oxygen is adsorbed on the gold surface, (ii) during the spillover process from the Au to the SnO_2 surface oxygen dissociates and is ionized by electrons from the conduction band of SnO_2 , and (iii) CO reacts with ionosorbed oxygen on the SnO_2 surface, releasing electrons back to the conduction band of SnO_2 . Increased oxygen instead of CO adsorption on Au surface was supported by DRIFT spectra.

The facilitated analyte gas molecules dissociation and surface reaction acceleration are recognized as the analyte spillover effect. The most well-known examples are Pt or Pd for H_2 sensing.^{53, 54} The various metal catalysts were synthesized, including Pt, Pd, Au, Ag, Ti, and Ni, loaded on ZnO nanorods.⁵⁵ The hydrogen sensing results revealed that Pt and Pd were a more effective catalysts for SMOX-based H_2 sensors at room temperature. A similar hydrogen spillover effect was also reported on Pd-SnO₂⁵⁶ and Pt/TiO₂⁵⁷ using temperature-programmed desorption and reduction.

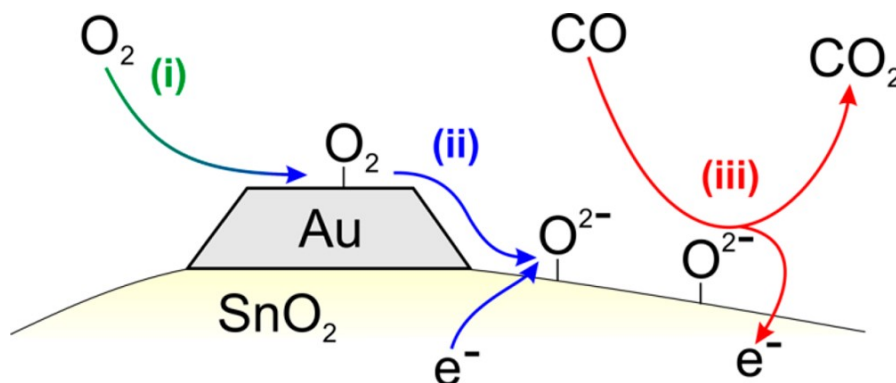


Figure 1.5 Proposed model for the oxygen activation and improved sensor performance on Au loaded SnO₂. Copyright 2016 American Chemical Society.⁵⁸

There are also other types of catalytic enhancement effects reported. The enhancement of CO oxidation through increasing the number of oxygen vacancies by Pd doping was theoretically investigated.⁵⁹

1.2.3.2 Conduction/Charge carrier transfer modulation

The improved speed of response and recovery or lowered operating temperature by simply utilizing the high charge transport capability of the highly conductive materials are ascribed as charge transfer effects.⁶⁰ The sensor response in 2 seconds with full recovery upon exposure to 50 ppm H_2S was reported based on SnO₂/rGO hybrids.⁶¹ The improvement was attributed to the co-effects of superior gas adsorption of SnO₂ nanocrystals and the excellent room temperature carrier transport capability of rGO. As aforementioned, the sensing properties of the combination of metal

oxides, such as SnO_2 ⁶¹, ZnO ⁴², NiO ⁴⁶, and Fe_3O_4 ⁶², with 2D rGO nanosheet were benefited from the superior conductivity of rGO at room temperature.

The electrical conductivity also could be modulated by the heterojunction within the interfaces between two dissimilar semiconductors. The formation of heterojunctions is always accompanied by the Fermi level alignment and the formation of carrier depletion/accumulation layer at the interfaces. The regulation of the interface potential energy barrier may enlarge the sensing response to gas analytes. Sensitive formaldehyde gas sensors based on indium oxides-sensitized zinc oxide (In_2O_3 - ZnO) were demonstrated.⁶³ By introducing narrow bandgap semiconductor In_2O_3 into the heterostructure, the sensor indicated a promising response to formaldehyde under the visible light condition at room temperature. Based on the understanding of the gas sensing enhancement effect from heterojunctions, the effect of TiO_2 quantum dot with NiO nanosheets was discussed in detail from different concentrations to quantum dot diameters.⁶⁴ The binding energy shift value and the peak area ratio of the Ni-O-Ti bond increased with smaller TiO_2 sizes and first increased and then decreased with the increased content, which was consistent with the change of the sensitivity.

The combination of different heterojunctions for gas sensing was also investigated in the ternary nanocomposites. The ternary rGO hybrids with the construction of n-n junction (ZnO/SnO_2) were reported for NO_2 sensing at room temperature.⁶⁵ The ternary ZnO/SnO_2 -rGO hybrids indicated the advantages of detecting NO_2 . The higher Fermi level of ZnO (5.2 eV) to SnO_2 (4.55 eV) led to the electron transfer from SnO_2 to ZnO , which promotes the ionization of oxygen at the ZnO surface. The dominant role of heterojunctions over morphology in gas sensing was studied with the Cr_2O_3 - SnO_2 nanocomposites.⁶⁶ The role of the contact between the oxides was identified via broking the original core-shell structures. The sensors prepared with the same ratios of Cr_2O_3 to SnO_2 indicated

identical sensitivity with a core-shell structure or crushed homogeneous film structure. However, the response type and sensitivity could be varied with different concentrations of each oxide. The results suggested the contacts between the different oxides dominantly contributed to the sensor behavior.

1.2.3.3 Molecular probing or sieving

The most effective way to improve the selectivity is by introducing a one-lock one-key binding between the sensing probe and the gas analyte. Inorganic and organic sensing probes have gained more research interests since the last decade. A simple chemiresistive NO₂ gas sensor based on the sodium bisulfite (NaHSO₃) functionalized 3D sulfonated rGO hydrogel was developed via a one-step hydrothermal method.⁶⁷ The response to NO₂ was well enhanced with the NaHSO₃ probe functionalization. The selectivity property also was regulated through temperature modulation using a microheater.

The 3-aminopropyltriethoxysilane (APTES) probe was introduced in the porous WO₃ nanotubes through a facile soaking process for NO₂ sensing.⁶⁸ The WO₃@APTES sensor indicated excellent response and selectivity to NO₂ due to the specific interaction between APTES and NO₂. The hydrophobic group of APTES also provided the humidity-resistant effect and ensured the operation even in a heavily polluted environment.

The selectivity property of the gas sensor also could be improved by introducing the sieving layer to avoid the interaction between the interfering gases and the sensing materials. Due to the uniform porous structure and sub-nanometer size of pores, the research efforts on the metal-organic framework (MOF) materials were increasing exponentially.

Zeolite imidazolate frameworks (ZIF) are a class of MOFs that are topologically isomorphic with zeolites. Polyoxometalates (POMs) are a class of molecular metal-oxo cluster compounds based mainly on Mo, W, and V elements. A highly selective HCHO sensor based on POM@ZIF-8@ZnO was fabricated. The specific role of ZIF-8 was sieving and the concentration of the HCHO analyte while rejecting other big interfering volatile organic compounds (VOC) molecules. The cross-sensitivity of HCHO over ethanol is 15.0.

The gas-sensing performance of ZnO@ZIF-8 core-shell heterostructures towards propene and ethene was also investigated.⁶⁹ ZnO nanorods were coated with a thin film of ZIF-8 via a sacrificial template-assisted method. The sensors indicated promising room temperature sensitivity and well-reduced cross-sensitivity to water vapor (humidity).

1.3 Research Objectives and Outline of Thesis

The objective of this dissertation study is to understand the sensing mechanisms of heterostructure-based chemiresistive gas sensors through in situ investigation and/or to analyze critical factors under real operating conditions. Various novel heterostructures are developed for specific types of gas sensing. A variety of in situ/operando techniques and analyses were applied to investigate the sensing mechanisms toward different gases.

Chapter 1 presents the background introduction and the literature review on in situ/operando techniques for gas sensing mechanism investigation and heterostructure-based chemiresistive gas sensors.

Chapter 2 describes the NiO-WO₃ nanowires-based heterostructure with improved hydrogen sulfide sensitivity at room temperature. In situ XRD and operando impedance measurements are performed to explore the sensing mechanism.

Chapter 3 presents the Au-SnO₂/rGO ternary nanohybrid heterostructures with accelerated and enhanced hydrogen sensing performance. Temperature-dependent experiments and Arrhenius analysis are applied to explore the sensing enhancement effect of gold nanoparticles.

Chapter 4 describes the Ni/SnO₂-rGO ternary heterostructures with an impressive low limit of detection toward sulfide dioxide gas at room temperature. The humidity-dependent experiment is conducted to better understand the sensor operation condition.

In Chapter 5, the organic polymer PT-COOH-rGO nanocomposite heterostructure was prepared. The gas sensing properties of this heterostructure were explored. Statistical signal processing methods were applied to illustrate the proof-of-concept results for gas discrimination.

A summary of the dissertation study and future research directions are presented in Chapter 6. This study provides insights into the heterostructure sensing mechanisms and offers guidelines for the rational design of heterostructures for gas sensing.

CHAPTER 2. IMPEDANCE ANALYSIS ON METAL OXIDE NANOWIRES HETEROSTRUCTURE ENHANCED HYDROGEN SULFIDE SENSING EFFECT

2.1 Introduction

Hydrogen sulfide (H_2S) is a highly toxic and flammable gas that is widely produced in coal mines and oil industries and used in sewerage pipe detection. Upon exposure, this gas affects the human nervous system and can become life-threatening at high concentrations. The effects of H_2S exposure at 2 ppm include nausea, headaches, or loss of sleep; at 20 ppm, fatigue, and headache; and between 50-100 ppm, respiratory tract irritation, digestive upset, and loss of appetite. Therefore, accurately detecting H_2S in both laboratories and human living places is essential.

H_2S typically has a rotten-egg odor, which can be detected by humans at concentrations as low as 0.5 ppb. This odor threshold concentration is much lower than the Occupational Safety and Health Administration (OSHA) ceiling point (20 ppm),⁷⁰ but olfactory fatigue occurs at continuous low-concentration inhalation as well as at high concentrations. Because human odor-level detection is not a reliable method for effectively detecting H_2S in the atmosphere, there is a demand for a highly efficient, low-cost H_2S gas sensor operable at room temperature for continuous monitoring in various workplaces to ensure employee safety.

Recently, various quasi 1D metal oxide semiconductor nanostructures (e.g., nanorods, nanowires, nanotubes, nanobelts) of various binary oxides have been found to be promising materials for gas sensing. Compared with traditional thin-film technology, the advantages of 1D nanostructures include higher surface-to-volume ratio, good stability, excellent crystallinity, and excellent signal transduction in the presence of gaseous species for their less defective structures.⁷¹ It is argued that

better sensitivity can be achieved with n-type 1D metal oxides through the modulation of initial resistance in background air. This can be realized when various surface oxygen species (O_2^- , O^- , O^{2-}) have been adsorbed on a simple oxide surface and depleted the electrons by creating a surface depletion potential width (λ_D). These adsorbed oxygen species further shrink the actual electron conduction diameter (the non-depleted core inside the nanorod, $D_{\text{Cond}} \sim D - 2 \lambda_D$, where D is the actual diameter) due to the surface depletion region. In addition, the heterojunction of two dissimilar oxides with different work functions could create a larger depletion area at the interface of two dissimilar oxides, which eventually enhances the initial resistance. The conduction pathway is modulated by the coverage of second oxides on the surface of the host oxides, catalytic nature, work function difference, and the thickness of the second oxide. In addition, heterostructures can remarkably improve the selectivity by optimizing the mixing ratio between dissimilar oxides.

WO_3 has been investigated as a sensing material for H_2S in recent years. Pure WO_3 films and noble metal decorated WO_3 nanomaterials have been reported for H_2S sensing. Granqvist and his group produced nanocrystalline WO_3 films using an advanced gas deposition method. After sintering at 750 K, the WO_3 film sensor exhibited extremely high sensitivity towards H_2S at room temperature. This good response is due to the formation of the tetragonal phase through sintering, but the detailed sensing mechanism remains unclear.⁷²⁻⁷⁴ Kim and his co-worker investigated the CH_4 and H_2S gas-sensing properties of pristine or Au nanoparticles-doped WO_3 nanowires at a high operating temperature. The increased sensitivity was attributed to the catalytic effect of the Au nanoparticles. The slower response time was caused by some delayed reactions in relation to the Au nanoparticles.⁷⁵

One drawback of the traditional metal oxide semiconductor gas sensor is its high operating temperature, which leads to high power consumption and limits the lifetime of the sensor. Hence,

there is a need to investigate sensing performance at room temperature. Sensing performance can be improved when semiconductor metal oxides form heterojunctions with other oxides, especially different types of metal oxides.⁷⁶ These modifications can substantially change the surface properties, as well as the electronic properties, because they enhance the depletion layer at the heterointerfaces. A heterojunction will form at the boundaries between two dissimilar materials; once the electrical contact at the interface is formed, the electrons at the higher energy level will flow across the interface to the lower-level states to equilibrate the Fermi energy levels.

The H₂S gas-sensing properties of metal-oxide heterostructures have been reported by many researchers over the past few years. Wang et al. synthesized 1D nanosized core/shell CuO-SnO₂ nanomaterials using a hydrothermal method. The p-n junctions are formed from p-type CuO nanoparticles uniformly coated on the n-type SnO₂ nanorods. The gas sensor based on these p-n junction nanomaterials indicated good sensitivity and selectivity against H₂S gas at 60 °C.⁷⁷ Gupta et al. demonstrated an H₂S gas sensor based on randomly distributed nano p-n junction between CuO and WO₃.⁷⁸ Modification of a WO₃ thin film with CuO resulted in enhanced sensitivity towards H₂S (sensitivity of 53,400% towards 10 ppm H₂S at 300 °C).

Lee et al. investigated the H₂S sensing properties of CuO-functionalized WO₃ nanowires at 300 °C.⁷⁹ The enhanced gas-sensing property of these p-n junction nanomaterials is likely the result of two factors: (1) The p-n junctions formed at the grain boundaries of p-type CuO and n-type SnO₂/WO₃ resulted in a potential barrier. The barrier blocked the electrons transporting through the nanomaterials, which increased the initial resistance of the sensors in air. (2) The formation of metallic CuS due to the interaction of CuO with H₂S resulted in a drastic decrease in the resistance of these sensors.

In addition, Zhou et al. prepared CuO-NiO core-shell microspheres using a simple two-step hydrothermal method.⁸⁰ At the optimal operating temperature of 260 °C, the gas sensors displayed the highest sensitivity of 460% towards 100 ppm H₂S gas. The improved response is due to the catalytic effect of NiO shell and the formation of heterojunctions at the boundaries between NiO and CuO, which resulted in a higher number of adsorbed oxygen molecules on the surface.

Few studies have explored the sulfurization reaction on the NiO or WO₃ surface during H₂S gas-sensing, especially at room temperature. Considering the work function of NiO is 9.4 eV, which is higher than that of CuO (8.5 eV), the massive work function difference between NiO and WO₃ may provide a broader depletion area formed at the heterojunction interface and lead to a larger resistance change during gas sensing. It could be deduced that the combination of 1D NiO and WO₃ nanostructures could potentially boost H₂S gas-sensing performance at room temperature.

In the recent literature, various 1D-1D heterostructures have been reported for efficient gas sensing, including 0D oxide-coated 1D structures, brush-like 1D-1D composite, and coaxial 1D-1D core-shell oxide composites with different fabrication processes using electrospinning, thermal evaporation, hydrothermal, and atomic layer deposition.⁸¹⁻⁸⁶ These processes are time-consuming, expensive, and power-hungry, and thus there is a demand to process heterostructures more quickly and less expensively while at the same time maintaining their crystal purity and improved sensing performance. Here we report a sensor based on NiO-WO₃ nanowire heterostructures synthesized through a facile-solution-based mixing method followed by gentle heat treatment. This process maintains high-quality crystallinity in constituent oxides without forming any secondary phase in the composite form. With this heterojunction nanowire composite, enhanced H₂S gas-sensing properties have been realized compared with pure nanowires. The typical sensitivity was 230% towards 10 ppm H₂S, and the lower detection limit could reach the ppb level. This type of gas

sensor showed better sensing performance (room-temperature sensitivity, selectivity, and limitation of detection (LOD)) when compared with most of the literature reports.

The detailed conduction mechanisms of pure and heterostructure oxides have been investigated through operando impedance spectroscopy analysis and equivalent circuit modeling. In addition to the adsorption-desorption mechanism, a unique surface sulfurization process during H₂S gas exposure is responsible for destroying the p-n junction effect by creating various quasi-metallic by-products (NiS, WS_{2-x}). This leads to a larger decrease in resistance from initial high base resistance, signifying the formation of the p-n heterojunction of specific composites. The sulfurization phenomena are only unique towards H₂S, thereby improving the selectivity against other reducing or oxidizing gases. The crystal phase formation of these quasi-metallic species at the surface has been further confirmed by in-situ X-ray diffraction (XRD) analysis.

2.2 Experimental Method

2.2.1 Sensor fabrication

The WO₃ and NiO nanowires (denoted as W and N, respectively) were provided by Sigma Aldrich (product number 774545, 774537). To prepare the xWO₃ – (1-x)NiO (where 0 ≤ x ≤ 1) heterojunction, the individual nanowire samples were prepared at the same concentration (0.01 M), with DI water as the solvent. Then, the samples were mixed separately in three different volume ratios, such as 3:1 (WO₃: NiO), 1:1, and 1:3, denoted as W3N1, W1N1, and W1N3, respectively. Finally, the heterostructure dispersions were obtained after 30 min ultra-sonication. Interdigitated Au electrodes were fabricated using e-beam lithography on a silicon substrate with a SiO₂ thin top layer. A tiny drop of the nanowire heterostructure dispersion was drop-casted on the Au electrode and the metal oxide nanowires bridged the Au fingers after solvent evaporation. After deposition,

the pure metal-oxide nanowire sensors were annealed at 200 °C for 1h in Ar flow (1 lpm) to improve the contacts among the sensing materials and between the sensing materials and the Au electrodes.

2.2.2 Gas sensing test

At first, a sensor chip was placed into an air-tight test chamber connecting with electrical feedthroughs. Then a constant dc voltage was applied to the electrode connected by nanowires or nanowire composites. One typical gas sensing test cycle had three continuous steps: First, a clean compressed dry air flow was introduced into the sensing chamber as the baseline of the whole test. Normally, the preset time for this step is 10 minutes or even longer till the baseline of current becomes stable. Second, the different target gases diluted in air were injected through the flowmeter into the test chamber with the same flow rate as the first step to generate the sensing signal. The exposure time for the target gas was 5 minutes. Finally, the target gas was turned off and clean air was introduced again for sensor recovery for 10 minutes.

2.3 Results and Discussion

2.3.1 Characterization

The morphology and crystal structure of the WO_3 and NiO and all the heterostructures were studied using scanning electron microscopy (SEM) (Hitachi S4800) and X-ray diffraction (XRD) spectroscopy. The surface chemical composition was characterized by X-ray photoelectron spectroscopy (XPS) (HP 5950A).

For in situ XRD detection, those five powder samples were deposited onto the sample holder for X-ray scanning. For sulfurization confirmation, the sensor chips containing sensing materials were

directly placed on the sample holder for XRD analysis after exposure to H₂S. The signal background of gold electrodes and the silicon substrate of sensor chips has been removed during the data analysis.

SEM images of the WO₃, W3N1, W1N1, W1N3, and NiO are shown in Fig. 2.1a(i)-(v), respectively. It can be observed that the diameters of the pure WO₃ and NiO are around 300 nm and 60 nm, respectively. The length of the WO₃ is around 1~3 μ m. Figure 2.1a(i) shows an SEM image of a typical WO₃ nanowire bridging a pair of Au electrode fingers in a sensor device. From Fig. 2.1a(i)-(v), the ratio of WO₃ and NiO in the images match the molar ratio calculated before, suggesting the formation of uniform dispersion.

The XRD patterns for WO₃, NiO, and NiO-WO₃ heterostructures are shown in Figure 2.1b. The peaks from pure NiO are weak and broad, suggesting that the crystallinity of the NiO nanowires is not very good. The XRD patterns of pure WO₃ can be indexed to cubic phase (JCPDS card 75-2187). There are no obvious peak shifts or any trace of other phases, besides pure NiO and WO₃, from other nanostructures. Therefore, the crystal structure of the three heterostructures is considered to have originated primarily from the mixture of cubic NiO and WO₃ with separate phases.

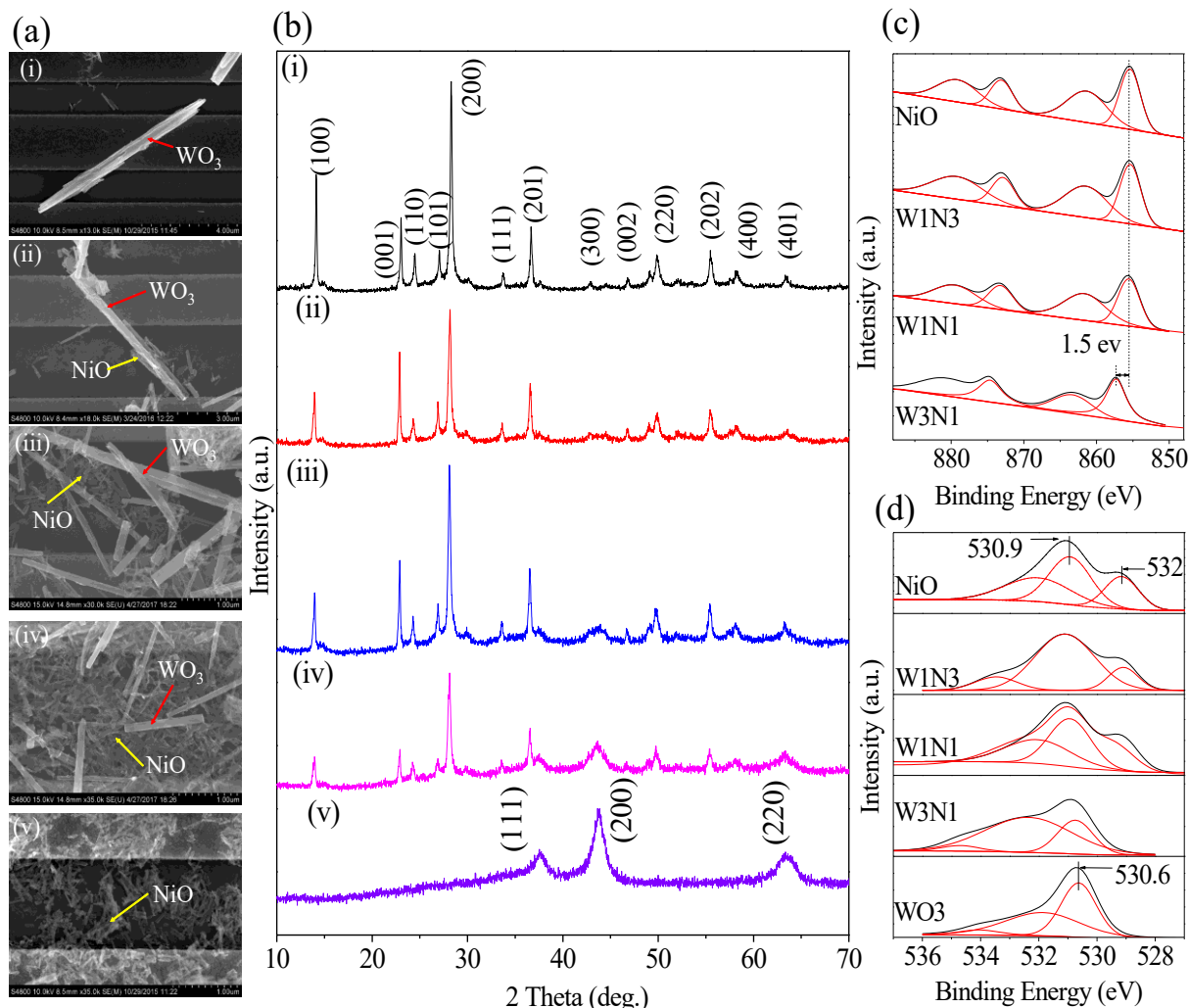


Figure 2.1 (a) FESEM images and (b) X-ray diffraction spectra of (i) W, (ii) W3N1, (iii) W1N1, (iv) W1N3 and (v) N powders. (c) O 1s and (d) Ni 2p high-resolution XPS spectra of pure WO₃, NiO, and NiO-WO₃ nanoheterostructures.

The XPS spectra of different samples were studied to investigate further valence chemistry and binding energy of constituent elements of the as-prepared metal oxide heterostructure samples. The carbon peak is reset as 285.0 eV. The O 1s XPS spectra of various samples are enlarged in Figure 2.1c. The XPS spectra of O 1s core-level electrons measured from pure NiO and WO₃ both display three peaks. The binding energies of 529.1 eV in NiO and 530.6 eV in WO₃ correspond with the lattice oxygen in crystalline NiO and WO₃, respectively.⁸⁷ Here, O 1s signals present shoulders located at the high binding energy (532.0-534.7 eV) side of each main peak for every

sample, which can be attributed to the OH species on the surface. The O 1s peaks at 530.9 eV in NiO, and 531.9 eV in WO₃ belong to the deficient or chemisorbed oxygen.⁸⁸ Note that because of the different chemical environments of O in heterostructure oxides, each characteristic peak has some shift in the three mixed heterostructure samples. Table 2.1 lists the corresponding binding energies and atomic ratios for different characteristic peaks of O 1s in these five oxide samples. The ratio of lattice oxygen increases gradually with the increase of WO₃ content in three heterostructure samples, suggesting more surface oxygen vacancies had formed.

Table 2.1 Corresponding Binding Energies (BE, eV) and Atomic Ratio Percentages (ARP, %) for Different Peaks of O 1s.

Samples	O_{lattice}		O_{ads}		O_{OH}	
	BE	ARP(%)	BE	ARP(%)	BE	ARP(%)
NiO	529.2	23.5	530.9	42.9	532.0	33.7
W1N3	529.1	14.8	531.1	72.9	533.5	12.2
W1N1	529.4	21.8	530.9	28.8	532.0	49.4
W3N1	530.7	26.7	532.4	68.3	534.7	5.0
WO₃	530.6	47.4	531.9	46.2	534.1	6.3

2.3.2 Gas sensing results and proposed sensing mechanism

Hydrogen sulfide is a colorless, toxic, and flammable reducing gas. Figure 2.2a shows the dynamic response of pure WO₃, pure NiO, and NiO-WO₃ heterostructures towards 10 ppm H₂S measured at room temperature. The bare NiO nanowires do not indicate any response against 10 ppm H₂S, just as reported in our previous study.⁸⁹ The sensitivity was enhanced significantly for W3N1, as discussed later in greater detail.

The NiO-WO₃ heterostructures show n-type gas-sensing behavior towards reducing H₂S gas due to the conductance difference in WO₃ and NiO. The bandgap of WO₃ (2.8 eV) is smaller than that of NiO (3.8 eV), which means the conductance of WO₃ is better; this made the WO₃ more dominant in sensing signal variation. The sensitivity decreases as the molar ratio of NiO increases further. This can be explained as the spillover effect caused by the non-responsive insulating layer of NiO on the surface of WO₃.

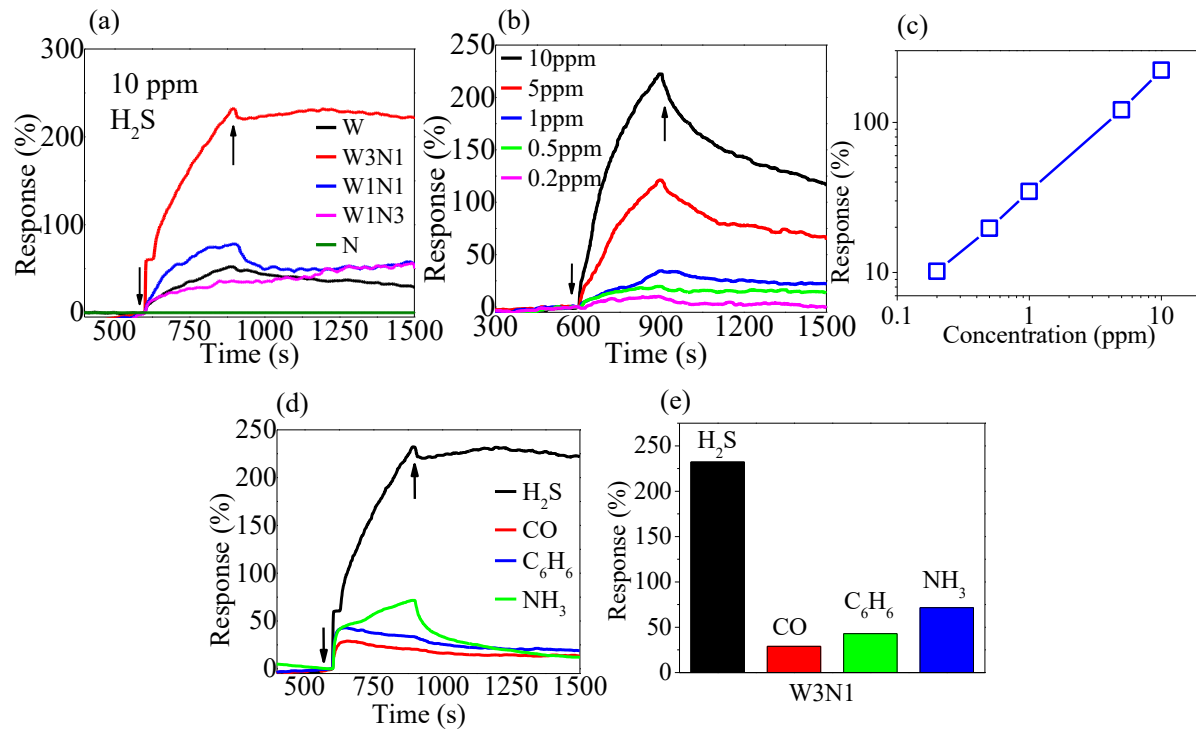


Figure 2.2 (a) Dynamic response and recovery curve of NiO-WO₃ heterostructures. (b) Dynamic response of the W3N1 heterostructures to 0.2 ppm, 0.5 ppm, 1 ppm, 5 ppm, and 10 ppm H₂S gas at room temperature. (c) Sensitivity variation of the W3N1 sensor as a function of H₂S concentration. (d) Dynamic response of W3N1 against 10 ppm H₂S, CO, NH₃, and C₆H₆. (e) Comparative performance for W3N1 towards 10 ppm H₂S, CO, C₆H₆, and NH₃.

. Figure 2.2b indicates the dynamic response of the W3N1 gas sensor exposed to different concentrations of H₂S at room temperature. The selectivity and sensitivity toward hydrogen sulfide were significantly higher than toward other gases, as shown in Figure 2.2 d-e, possibly due to the

lower dissociation energy of H₂S. The dissociation energy of the hydrogen sulfide (91.2 kcal/mol) is less than carbon monoxide (256.3 kcal/mol), benzene (112 kcal/mol), and ammonia (107.6 kcal/mol); as a result, the sensing response perfectly matches the dissociation energy ranking of these four gases.

Table 2.2 briefly summarizes the gas-sensing performance of various metal-oxide-based sensors toward H₂S at room temperature. The sensitivity of our NiO-WO₃ heterostructures is comparable with that reported in the literature. It is worth noting that the synthesis method of our work is less expensive compared with others reported in the literature (listed in Table 2.2).

When the Fermi level (E_F) of one semiconductor material is different from that of another (i.e., due to the work function difference), the electrons flow across the grain boundary after the contact between these two semiconductors until the Fermi energies have equilibrated at the interface. For the connection between p- and n-type semiconductors, as illustrated in Figure 2.3, the primary carrier (holes and electrons for p- and n-type semiconductors, respectively) diffuses across the interface, leading to its depletion and the band bending across the interface. For the metal-oxide-based FET sensors, O₂ molecules can adsorb on its surface upon exposure to air and thus extract electrons from the conduction band (E_{CB}) in the metal oxides, turning into oxygen ions residing on the surface.

Table 2.2 Comparison of the Room-Temperature-Sensing Performance of Various Metal-Oxide-Based Gas Sensors Towards H₂S.

Material	Method	Conc. (ppm)	Sensitivity (%)	Response/ Recovery time(s)	LOD (ppb)	ref
In ₂ O ₃	Carbothermal method	10	40%	~60/~7,200	200	⁹⁰
Zn/ZnO	Thermally evaporated deposition	8	60%	~270/~7,50	1,000	⁹¹
Cu/SWCNTs	Spin-coating	20	30%	10/20		⁹²
CuO/SWCNTs	Drop-casting	10	45%		100	⁹³
SnO ₂ multitube arrays		5	50%	14/30	5,000	⁹⁴
SnO ₂ -CNT	CVD	50	30%	~60/~60	9,000	⁹⁵
quasi-2D CuO/SnO ₂	Electrochemical deposition	50	80%	180/500	500	⁹⁶
CeO ₂	Tube film coating	10	60%	50/75	50	⁹⁷
CuO ₂ -FGS	Syringe dispensing	0.1	40%	120/300	5	⁹⁸
NiO/WO ₃	Mechanical mixing	10	230%	270/~7,200	200	this work

Physically, both the molecular (O₂⁻) and atomic (O⁻, O²⁻) oxygen ions can be formed, while the coverage of the latter will increase at elevated temperatures.⁹⁹ The p-n junction formation on the heterostructure surface will decrease the barrier for electrons transfer from metal oxide to the adsorbed O₂, which will lead to the formation of molecular oxygen ions (O₂⁻) at room temperature.

For the nanowire materials, this p-n junction formation will make the major carrier transfer channel narrower.

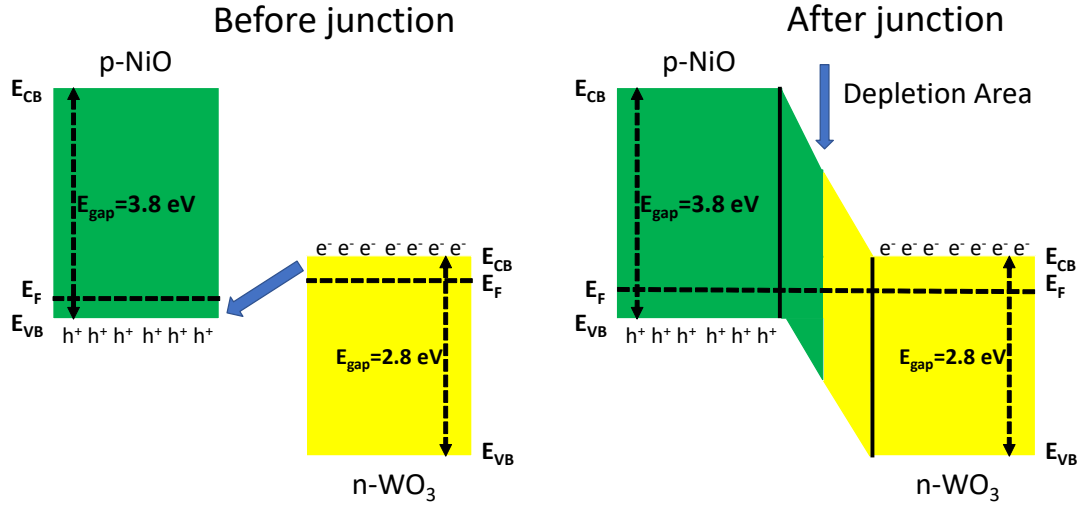
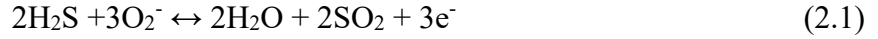


Figure 2.3 Schematic illustration of the formation of the p-n junction between n-type WO_3 and p-type NiO.

From the gas-sensing performance, it was found that the W and W3N1 samples show n-type behavior, whereas W1N1, W1N3 and NiO samples indicate p-type behavior. This suggests that the gas-sensing performances for these two types are predominantly controlled by the relative amount of the W and N sites. It is also evident from the microstructure that the NiO nanowires are sequentially percolating the WO_3 nanowires with the increased NiO content, a generalized grain distribution model of these two typical heterostructures (W3N1 and W1N3) is shown in Figure 2.4 ab, respectively. For the W3N1 samples (Figure 2.4a), the current is predominantly controlled by the W sites, whereas the N sites control the rest of the heterostructure sensors (W1N1 and W1N3). For all the sensing materials, W3N1 exhibits maximum sensing performance.

In general, three major factors play a role in enhancing sensing performance. The H_2S sensing mechanism for metal oxide sensors can be ascribed by two different mechanisms, adsorption-

desorption and sulfurization-desulfurization. Due to the room-temperature operation, the adsorbed oxygen gas species on the oxide surface is molecular oxygen ions (O_2^-). Thus, the adsorption-desorption mechanism becomes



while for the sulfurization mechanism, the NiO and WO_3 grain surface can show the following set of reactions



where x stands for the stoichiometric ratio.

Due to first the reaction by Reaction 1 (adsorption), the resistance of the pure WO_3 decreases as the number of majority carriers (electrons) increases. Whereas for p-type NiO, the resistance increases due to the electron-hole recombination-induced reduction of the majority carrier (hole). For sulfurization reactions (Reactions 2 and 3), due to the formation of semi-metallic (narrower bandgap materials) $NiS_{(1-x)}$ and $WS_{(2-x)}$,⁸⁷ a much more conducting path can be created on the surface of the sensors upon H_2S gas exposure. Physically, both mechanisms can simultaneously occur in pure metal oxide samples.

However, the formation of the heterojunction between the NiO and WO_3 , induced by the electrons from the WO_3 side diffusing to the NiO side and the holes from the NiO side towards the WO_3 site, leads to a large potential barrier, and, especially, a very high initial resistance of W3N1 samples in the air compared with other samples. This is consistent with similar work reported in the literature about the formation of p-n junctions.^{100, 101} In the presence of H_2S gas, this large potential barrier decreases due to the adsorption-desorption mechanism but drastically collapses due to the surface sulfurization (formation of $WS_{(2-x)}$) process; both effects, in turn, cause a large

decrease in resistance. Therefore, for the W3N1 samples, the sensing mechanism is enhanced by the collapse of heterojunction, which decreases the resistance considerably.

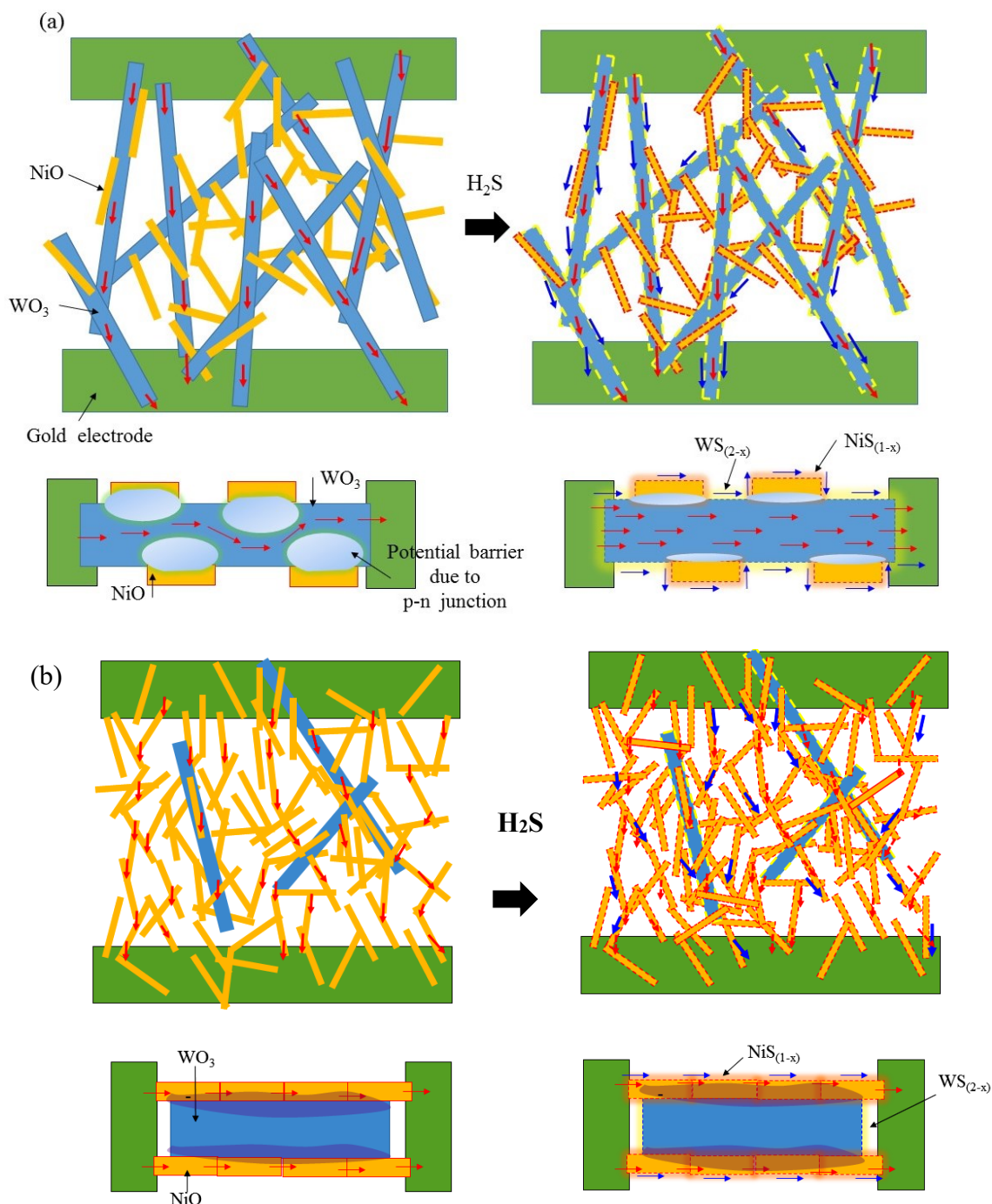


Figure 2.4 Schematic conduction pathway model during H_2S gas exposure for (a) W3N1 and (b) W1N3.

For the p-type W1N1 and W1N3 heterostructures (Figure 2.4b), the sensing performance is dominantly controlled by the smaller NiO grains, since the WO₃ grains are segregated from the electrode. Similarly, due to the adsorption-desorption mechanism, the resistance of the NiO grain/grain boundary should be increased, while the resistance decrease in the grain surface is also possible from the sulfurization process. As a result, the total change in resistance in H₂S gas exposure depends on which of these two competing processes (opposite change in resistance) is dominant. For the W3N1 heterostructure, the NiO-coated WO₃ nanowires can easily interconnect with finger electrodes and thus enhance the sensitivity by the same direction change in resistance from the adsorption-desorption mechanism, heterojunction effect, and sulfurization process, whereas the sensitivity decreases for W1N1, W1N3, and NiO samples due to the opposite compensation effect.

2.3.3 In situ characterization and impedance analysis

To further confirm the sulfurization process, in-situ XRD analyses were performed with the samples after exposure to H₂S. Figure 2.5a-c shows the XRD plot of all the tested sensors before and after the injection of the H₂S gas. Significantly, the new intense peaks for WS_(2-x) were confirmed for the W and W3N1 samples, but the NiS peaks were weaker for the rest of the samples. From the literature, Gibbs free energies of NiS and WS₂ formation are found as -61.6 kJ/mol and -232.1 kJ/mol, respectively.^{87, 102} Therefore, the propensity of the sulfurization reaction of NiO is weaker than WO₃. Thus, a good combination and the same directional changes due to the adsorption-desorption mechanism, heterojunction effect, and sulfurization process enabled the W3N1 sample to achieve higher sensitivity than any other samples.

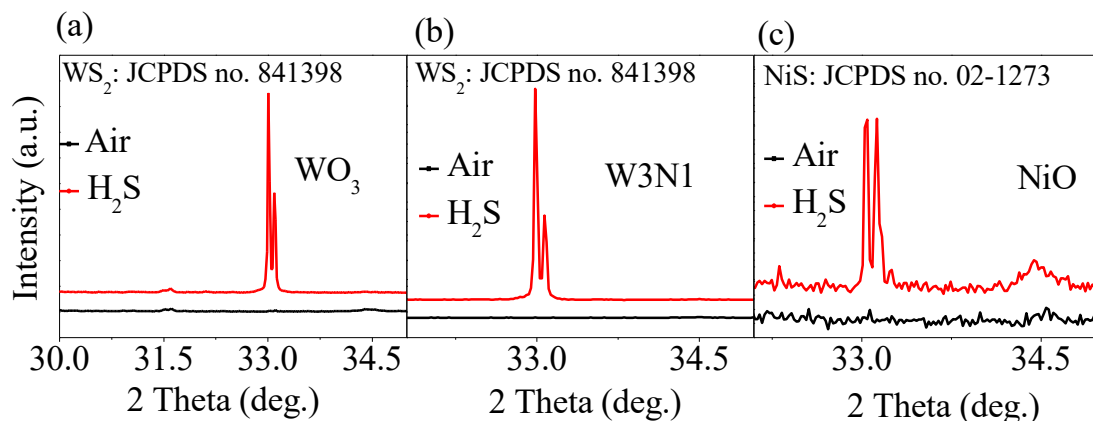


Figure 2.5 Comparison of XRD peaks for samples before and after H₂S exposure (a) WO₃, (b) W3N1, (c) NiO.

To further confirm these cooperating and competing effects and to visualize the individual effects, operando impedance analysis (amplitude 10 mV) was performed before and after gas exposure for all pure and heterostructure sensors.

Figure 2.6 a-e shows the measured Nyquist plot for the sensor in air and in 10 ppm H₂S gas. The electrical equivalent circuit model is adopted from the contribution of nanowire grain, inter-boundary, or junction among nanowires. These can be expressed as a set of RC parallel circuit components. For n-type materials, dominant contributions for sensing come from nanowire grain and grain boundary, and they can be expressed as a set of RC (RC_{grain} and $RC_{\text{grain boundary}}$) circuits (shown in Figure 2.7a). For p-type material, the situation is different: when the electrons are adhered by adsorbed molecular oxygen (O_2^-) from a p-type oxide surface, a vast amount of hole is accumulated on the surface, which leads to a thin conducting “shell”-like accumulation layer and creates a lower conducting “core” inside the oxide. This core-shell parallel electrical circuit can be represented by two RC parallel circuits connecting in parallel (Figure 2.7b).

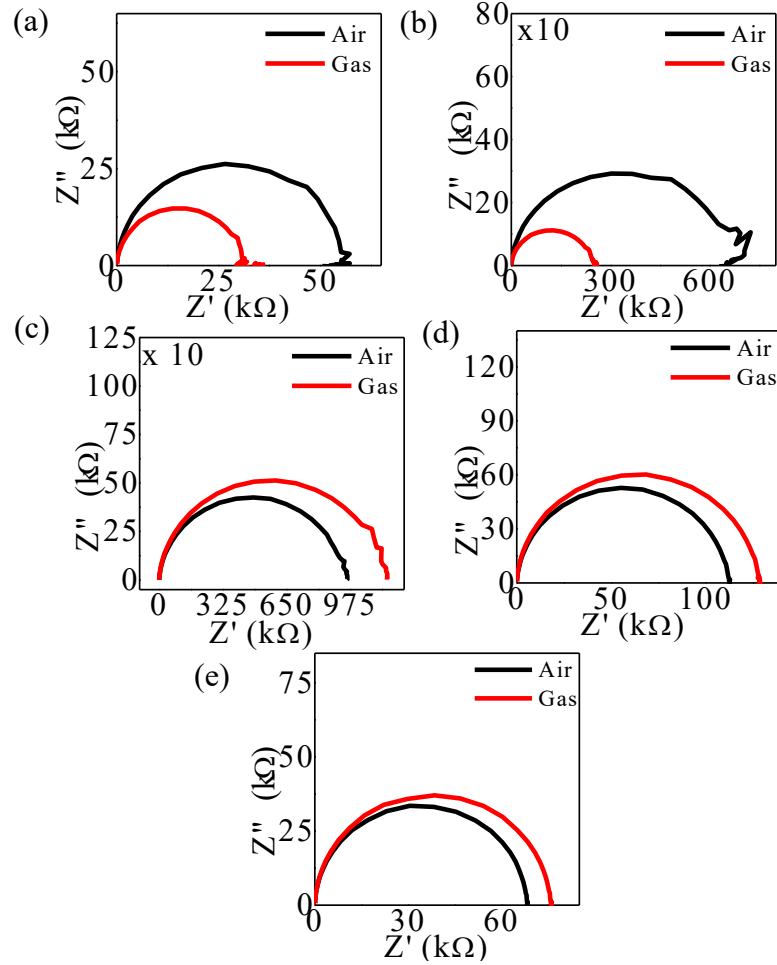


Figure 2.6 Impedance spectroscopy sensing plots of all samples against H_2S (a) WO_3 , (b) W3N1 , (c) W1N1 , (d) W1N3 , (e) NiO .

In addition to these contributions, the “neck” contributions among nanowires need to be considered. As our nanowires are loosely sintered at low temperature ($\sim 200^\circ\text{C}$), the “neck” regions are widely opened and thus should have another contribution (represented by an additional RC circuit (RC_{neck})). The equivalent circuit can then be simplified from equivalent contributions from the “core-shell” ($\text{RC}_{\text{core-shell}}$) and RC_{neck} (Figure 2.7b) connected in series. For the mixed p-n heterostructure of NiO-WO_3 , the actual model will be a superposition of all these components and p-n junctions across nanowires, which are responsible for major resistive components on the sensor surface (represented by $\text{RC}_{\text{junction}}$). For simplicity, we followed the circuits for mixed heterostructures per

their gas-sensing performance (n- or p-type). Thus, Figure 2.7ab represents the circuit schematic of heterostructure oxides that show n- and p-type sensing behavior, respectively.

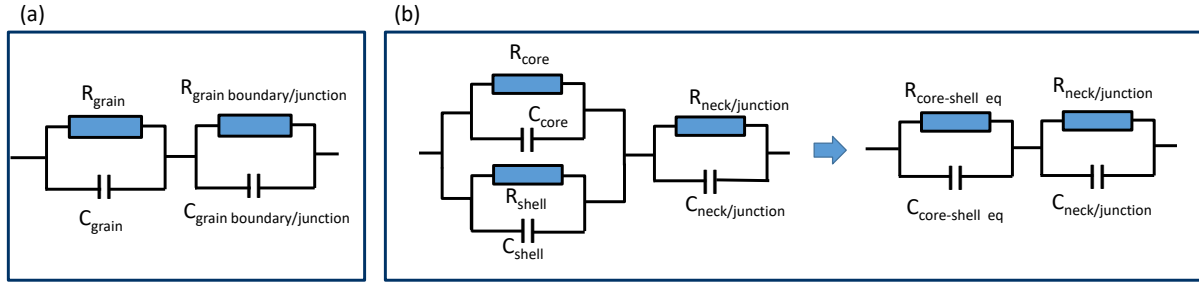


Figure 2.7 Schematic illustration of the overall equivalent circuit (a) n-type, (b) p-type.

Table 2.3 Calculated Resistance Parameters and Their Sensitivity% in Air and H₂S Gas for Pure and Heterostructure Sensors.

Condit	W		W3N1		W1N1		W1N3		N	
ion	R _G	R _{GB}	R _G	R _{JNC}	R _{CS}	R _{JNC}	R _{CS}	R _{JNC}	R _{CS}	R _{NCK}
	(KΩ)	(KΩ)	(KΩ)	(KΩ)	(KΩ)	(KΩ)	(KΩ)	(KΩ)	(KΩ)	(KΩ)
Air	1.5	55.2	571.	114.90	637.9	328.6	110.7	2.1	67.2	1.2
			9							
Gas	1.5	29.6	195.	60.403	1117.	55.1	127.2	1.8	74.6	0.3
			2							
S%	-0.2	-46	-65.8	-47	75	-83	14.6	-14.5	10.4	-69.2
Total	-45.1		-62.8		21		14		9.5	
S%										

Using the equivalent circuit model, as previously discussed, the impedance data are fitted to extract these parameters in the air and upon H₂S gas exposure. Table 2.3 shows the calculated resistances from each component for pure and heterostructure sensors and the calculated sensitivities from individual resistance components and total resistance change. Here, the negative and positive signs signify the resistance decreases and increases in the presence of gas exposure. As found from the analysis, both grain and grain boundary/junction resistance decreased for W and W3N1, whereas

other heterostructures (W1N1 and W1N3) and N samples showed a competing behavior of corresponding resistive components, leading to lower sensitivity.

2.4 Conclusions

A NiO-WO₃ nanowire p-n heterojunction random network structure was fabricated using a facile, sonication-based solution mixing method for different volume ratios, followed by gentle low-temperature annealing (200 °C). The XRD data shows the phase purity of constituent oxides in discrete and composite form is maintained well. SEM images showed that a shorter NiO nanowire distributed around a relatively longer WO₃ nanowire (1D-1D structure) and formed heterojunction coating. The resulting heterojunction effect was maximally observed for W3N1 (75 mol% WO₃-25 mol% NiO) and confirmed by observation of the increase in resistance due to the formation of a diode-like p-n junction at the WO₃-NiO interface.

The optimal room-temperature H₂S gas-sensing with excellent selectivity was observed for the W3N1 sensor, which exhibited a sensitivity of ~230% for 10 ppm H₂S—this is one to two orders of magnitude higher than individual oxides and other composite samples. The excellent sensing performance for W3N1 is attributed to the p-n junction effect, sulfurization by H₂S (formation of WS_{2-x} and NiS_{1-x}), and the ideal ratio of the NiO component in the composite. The formation of reactive semi-metallic products due to sulfurization was confirmed by XRD analyses for H₂S adsorbed on the sensor surface.

Further investigations from in-situ impedance measurement and RC equivalent circuit analyses during gas sensing were performed to evaluate the grain-grain boundary or the contributing effect of the p-n junction in sensing performance. It was found that for the pure WO₃ and W3N1 sample, these contributing effects are in the same direction, resulting a cooperating and highly sensitive

performance, whereas other samples (W1N1, W1N3 and N) exhibited competitive influences, resulting in a lower sensitivity. The W3N1 sensor also exhibited good selectivity to H₂S compared with other interfering gases, such as CO, C₆H₆, and NH₃. This could be explained by additional semi-metallic conducting effects from H₂S-mediated sulfurization and lower dissociation energy of H₂S.

This simple, economical, and energy-saving method could be potentially attractive for the development of various 1D-1D p-n junction composite sensors for room-temperature, low-cost, alarm-based gas sensors to detect various toxic gases, inflammable compounds, and explosives.

CHAPTER 3. QUANTITATIVE ANALYSIS OF THE SYNERGISTIC EFFECT OF AU NANOPARTICLES ON TIN OXIDE-RGO NANOCOMPOSITES FOR ROOM TEMPERATURE HYDROGEN SENSING

3.1 Introduction

Hydrogen (H_2) has been considered and investigated as one of the most promising sustainable fuels since it produces no air pollutants in fuel cells. However, hydrogen is very flammable and could lead to an explosion at a high concentration (4%) in air.¹⁰³ As hydrogen is colorless, odorless, and highly flammable under ambient conditions, it must be reliably monitored in real-time during its production, delivery, storage, and utilization.

Graphene has been widely reported as a promising gas sensing material due to the extreme single gas molecule sensitivity, large surface-to-volume ratio, and excellent electronic signal transduction property (high carrier mobility and high signal-to-noise ratio).³² However, lack of selectivity and poor sensitivity to hydrogen limit its application for hydrogen sensing.¹⁰⁴ As is well known, the sensing performance of graphene could be improved through functionalization with metal oxides or noble metals. Tin oxide (SnO_2) is one of the most widely investigated metal oxides for gas sensing applications owing to its high response, low cost and good stability.^{37, 61, 105} The SnO_2 nanocrystals-rGO sensing platform reported in our previous work demonstrated advantages such as tunable sensing performance and room temperature operation.³⁶ Since SnO_2 -rGO based sensing material still suffers from cross-sensitivity to NO_2 ,³⁷ CO ¹⁰⁶ and H_2S ,⁶¹ further surface modification to the SnO_2 -rGO platform is needed to improve the selectivity. Noble metals, especially palladium

(Pd)^{24, 107, 108 109, 110} and platinum (Pt),^{111, 112} were widely used in H₂ sensors due to their high solubility and ability to dissociate hydrogen molecules. However, a highly enhanced sensitivity due to activated hydrogen dissociation also leads to poor sensor recovery. The practical balance between sensing and recovery performances is an ongoing pursuit.

Gold is another noble metal dopant for gas sensing, which is more abundant than platinum on earth with a lower cost than palladium.^{25, 113-118} Zhang et al. synthesized the Au-loaded SnO₂ composite by a hydrothermal method and investigated the hydrogen sensing properties of the sensor based on the composite.¹¹³ The Au-loaded SnO₂ composite showed high sensitivity, a low detection limit, and excellent selectivity for H₂ but at an elevated temperature of 250 °C to activate the adsorption process. Therefore, it is promising to combine the gold dopant with the SnO₂-rGO sensing template to achieve desirable hydrogen sensing performance at room temperature.

3.2 Experimental Method

3.2.1 Material synthesis and sensor fabrication

SnO₂/rGO nanohybrids were prepared first. In a typical synthesis, GO (8 mg) was dispersed in DI water (10 ml), in which 45 µl of HCl (37%) was added. Then SnCl₂•2H₂O (50 mg) was dissolved in the DI water (10 ml) with 30 mins stirring at 90 °C. Afterward, the aqueous solution of SnCl₂•2H₂O was added to the GO dispersion under magnetic stirring at 90 °C for 1 h. After cooling down to room temperature, the SnO₂-rGO nanohybrids were washed with DI water several times and dried at 60 °C overnight. Finally, SnO₂-rGO powders were obtained.

Au doped SnO₂/rGO nanohybrids were prepared through the sputter coating method. 20 mg SnO₂-rGO powders were dissolved in 50 ml DI water under ultrasonication. Then, 2 µl of dispersion was drop-casted on the interdigitated electrodes, which was reported previously.¹¹⁹ After drying at

room temperature, Au nanoparticles were deposited onto the surface of these sensors using a sputter coater (K550X, Quorum Technologies). The sputtering current was 20 mA and the sputtering time was varied from 3 to 12 s for different gold area densities. These sensors were annealed at 200 °C for 1 h in Ar flow (1 lpm) to improve the contact between the nanohybrids and the gold electrodes. Pure rGO and SnO₂-rGO sensors were also prepared as control samples.

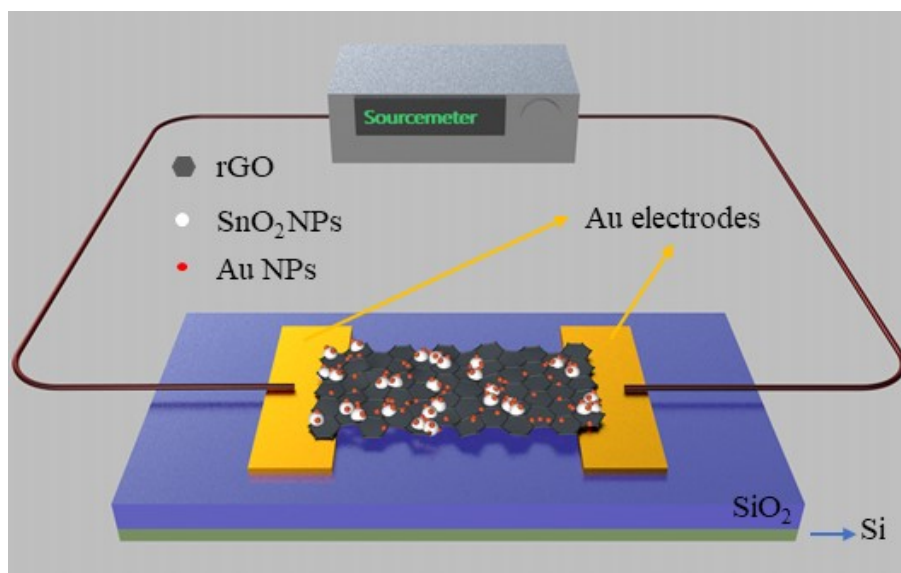


Figure 3,1 Schematic of the Au-SnO₂/rGO sensor device and measurement system.

3.2.2 Characterization and gas sensing test

The morphologies of the materials were observed by a Hitachi (S4800) field-emission scanning electron microscopy (FE-SEM). The energy-dispersive X-ray spectroscopy (EDS) line scanning data were obtained using a Bruker detector on the Hitachi S-4800 FE-SEM. X-ray diffraction (Bruker D8 Discover X-ray diffractometer) was performed to identify the crystalline phases. X-ray photoelectron spectroscopy (XPS) was conducted by using VG ESCA 2000 with an Mg K α as the source and the C1s peak at 284.5 eV as an internal standard.

Figure 3.1 shows a schematic of the Au-SnO₂/rGO sensor device and the circuit for electrical measurements. A typical gas sensing test cycle had three steps. The first step was the introduction of clean carrier gas into the sensing chamber and was used to obtain a baseline measurement. The typical preset time for this step was 10 minutes or until the baseline became stable. The second step was the addition of various target gases being injected through the flowmeter into the test chamber with the same flow rate as the first step to generate the sensing signal. The exposure time for the target gas was 5 minutes. Finally, the third step involved the target gas is turned off and a 100% composition of the carrier gas being introduced again for sensor recovery. The third step lasts for at least 10 minutes.

3.3 Results and Discussion

3.3.1 Characterization

The crystallization of the SnO₂/rGO nanocomposite was examined by X-ray diffraction (XRD). The XRD patterns (Figure 3.2c) of the SnO₂/rGO nanocomposite display clear reflections from the (110), (101), (211) and (112) planes of rutile SnO₂, indicating the formation of SnO₂ crystals.¹²⁰ Scanning electron microscopy (SEM) was used to analyze the morphology of Au-SnO₂/rGO nanohybrids and the sensor chip (Figure 3.2a). The rGO nanosheets bridging two gold electrodes were modified with well-dispersed SnO₂ and Au nanoparticles on the surface. The existence of Sn and Au elements could be verified through the line scan (Figure 3.2b) of Energy-dispersive X-ray (EDX) analysis. X-ray photoelectron spectroscopy (XPS) was conducted to examine the elemental composition and chemical states of the species in the GO and Au-SnO₂/rGO nanohybrids.

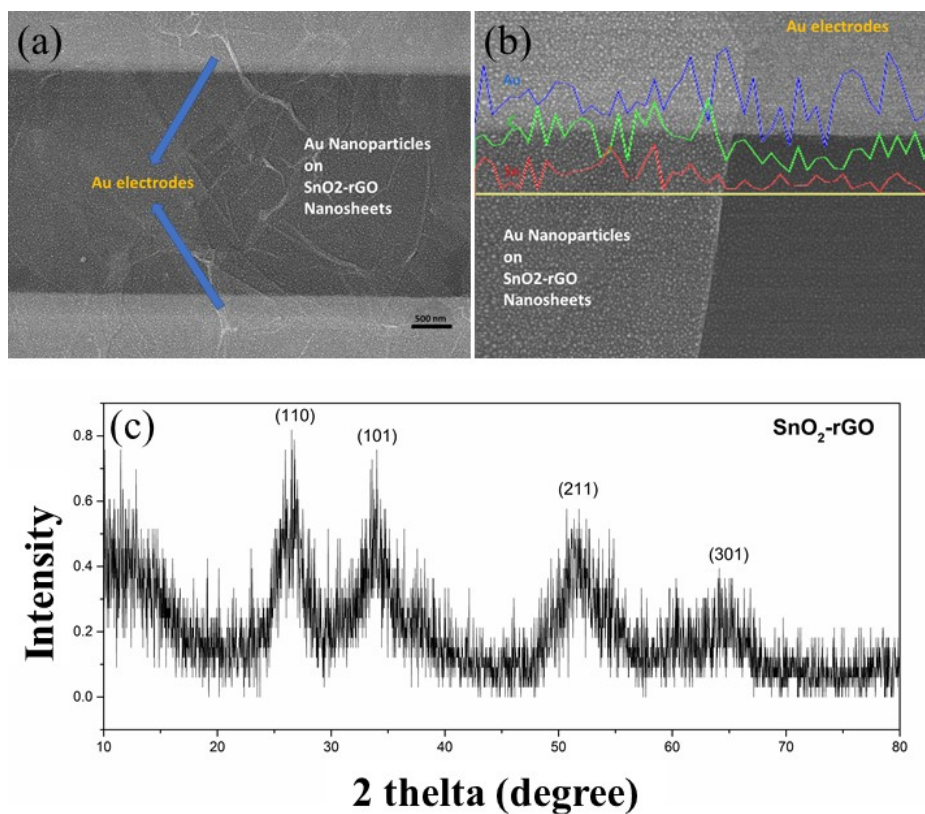


Figure 3.2 (a) SEM image of Au-SnO₂/rGO sensor chip. (b) Line scan EDX data combined with SEM image of the Au-SnO₂/rGO sensor. (c) XRD pattern of SnO₂-rGO nanohybrids.

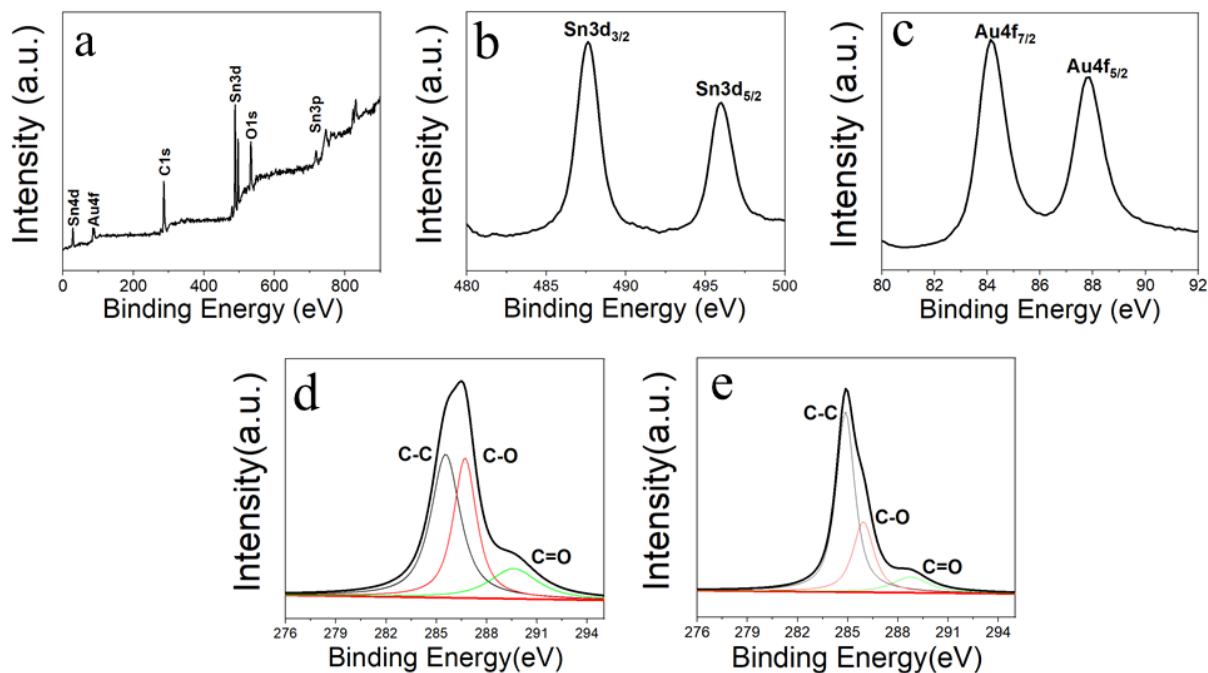


Figure 3.3 XPS spectra of a) Au-SnO₂/rGO nanohybrids. (b) Sn 3d and (c) Au 4f spectra of the Au-SnO₂/rGO nanohybrids. (d) C 1s of GO and (e) the Au-SnO₂/rGO nanohybrids.

The wide-survey XPS spectrum (Figure 3.3a) of the Au-SnO₂/rGO nanohybrids reveals the existence of Au, Sn, O, and C elements. Figure 3.3b indicates two characteristic peaks at 496.0 eV and 487.5 eV, which are attributed to the binding energy of Sn 3d_{5/2} and Sn 3d_{3/2}, respectively.¹²¹ The XPS spectrum of Au (Figure 3.3c) presents two main peaks at 84.1 eV and 87.8 eV, which are related to Au4f_{7/2} and Au4f_{5/2}, respectively, suggesting the existence of metallic Au on the surface.¹²² XPS C1s spectrum has been reported as an effective method to estimate the reduction level of graphene oxide.¹²³ The C1s spectra of GO (Figure 3.3d) and Au-SnO₂-rGO (Figure 3.3e) all consist of three characteristic peaks, corresponding to C-C, C-O, and C=O groups.¹²⁴ The intensities of C-O (285.9 eV) and C=O (288.8 eV) in Figure 3.3e are all reduced compared to the intensities of the relevant peaks from GO C1s spectra. This reduction reveals the reduced amount of oxygen from GO to Au-SnO₂/rGO nanohybrids, which agrees well with Raman analysis (Fig. S2).

3.3.2 Gas sensing performance

To unveil the effect of gold nanoparticle doping on hydrogen gas sensing, we investigated the sensor response towards hydrogen gas with or without dopants in a laboratory-built testing system. Here, we define the sensitivity as $\text{Response (\%)} = [(I_g - I_a)/I_a \times 100]$, where I_g is the current in the presence of H₂ and I_a is the base current in the air. The small enhancement (1.5%) of hydrogen detection through SnO₂ nanoparticles decoration is indicated in Figure 3.4a. This is due to the small coverage of chemisorbed oxygen on the SnO₂ surface at room temperature.¹¹¹ Figure 3.4b shows the typical response curves of rGO and Au-rGO to 1% H₂. Pure rGO sensors exhibit a weak response (2.5%) to 1% H₂ which is consistent with the previous report.¹⁰⁴ rGO modified with sputtered Au nanoparticles shows improved sensitivity and partial recovery, most likely due to the

higher-energy binding sites provided by Au nanoparticles; full recovery was not achieved in 10 minutes under room temperature.

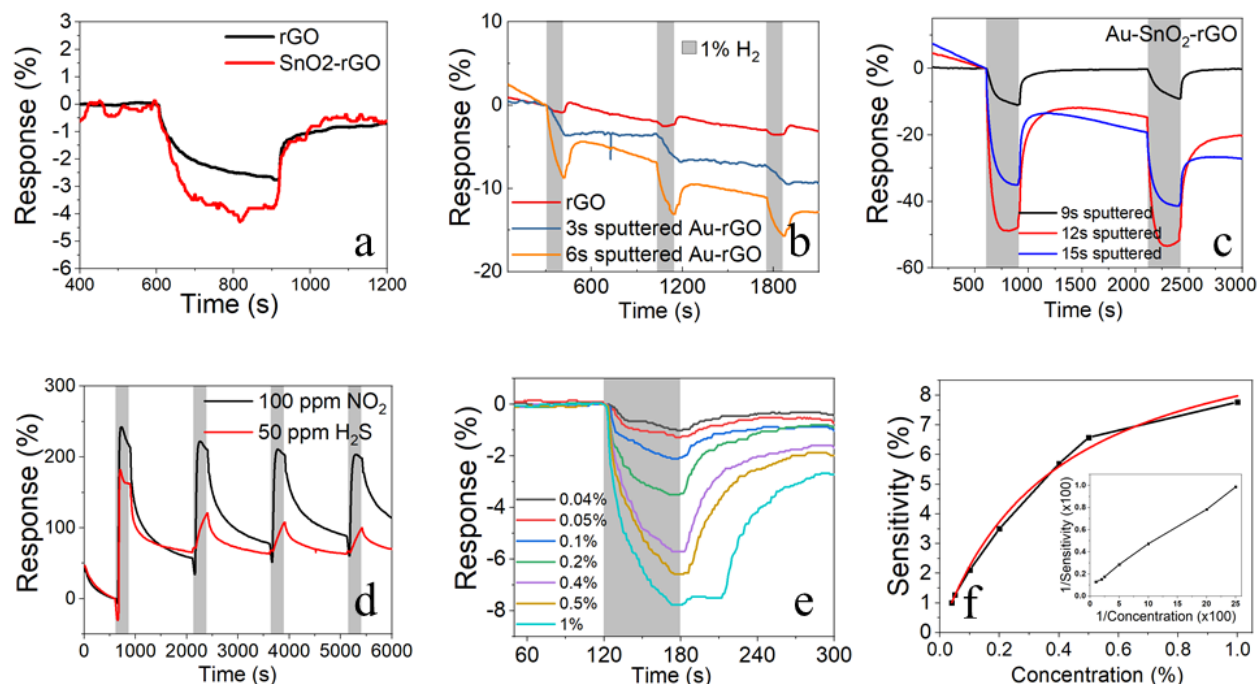


Figure 3.4 Responses to 1% H₂ of a) rGO and SnO₂-rGO. b) rGO and Au-rGO. c) Au-SnO₂/rGO nanohybrids with different sputtered gold thickness. d) dynamic response curves of 12s sputtered Au-SnO₂/rGO to 100 ppm NO₂ and 50 ppm H₂S. e) dynamic response curves of 12s sputtered Au-SnO₂/rGO to H₂ with varying concentrations from 0.04% to 1% in 1 min. f) Calibration curves of 1 nm Au-SnO₂/rGO sensors to H₂ gas.

Figure 3.4b-c shows the dynamic response of Au-SnO₂/rGO nanohybrids to 1% H₂ with different Au loading amounts related to different sputtering time length. Figure 3.5 indicates the good uniformity of the gold nanoparticles on the silicon wafer through sputtering. The quantitative EDS analysis results of the surface elements are shown in Table 3.1.

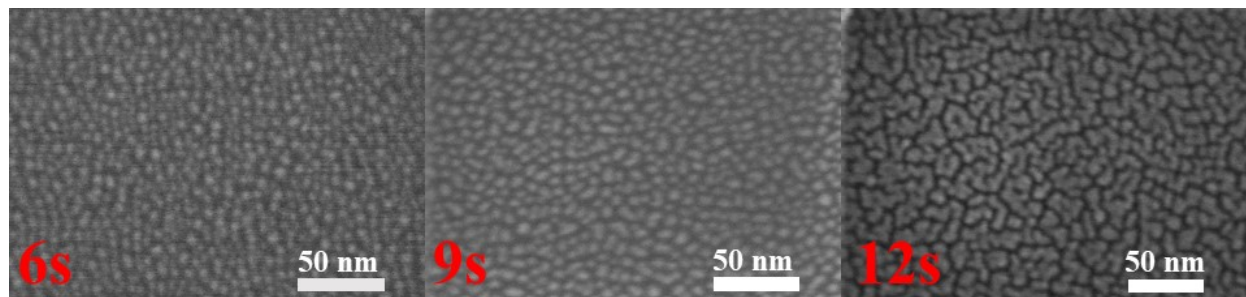


Figure 3.5 SEM images of sputtered gold nanoparticles on silicon wafer with different sputtering time.

Table 3.1 Quantitative Atomic ratio (%) analysis on the sputtered gold EDS results.

Element	Si	O	Au	C
6s	61.82	29.61	0.05	8.51
9s	61.44	29.36	0.06	9.14
12s	63.15	29.72	0.08	7.05

The sensitivity reached 47% after baseline subtraction for 12s sputtered Au loaded SnO₂-rGO sensors in 5 minutes of hydrogen exposure at 21.5 °C (RT). The sensing responses to 100 ppm NO₂ and 50 ppm H₂S (Figure 3.4d) showed a quick decay in sensitivity and deactivation after several cycles, which is likely due to the strong binding of NO₂/H₂S molecules that consumes the chemisorbed oxygen and leads to the poisoning effect on the sensing surface.¹²⁵⁻¹²⁷ The poisoning effect may be related to the drained out of the chemisorbed oxygen or binding sites after several sensing cycles. The hydrogen concentration-related dynamic response curves and the calibration curves are indicated in Figure 3.4e-f.

$$\text{Sensitivity} = \frac{a}{1 + \frac{b}{\text{Concentration}}}$$

Figure 3.4f is well fitted by the Langmuir isotherm¹²⁸, where a is a constant equal to 11.1353 without unit and b is another constant equal to 0.3955 has the same unit as the concentration (%). This can be explained from the relationship between the surface coverage and gas partial pressure in Langmuir isotherm, which has been confirmed by the linear fitting of 1/Sensitivity vs. 1/Concentration shown in Figure 3.4f inset. The excellent sensing performance is competitive when compared with other reported room temperature hydrogen sensors as summarized in Table 3.2.

Table 3.2 Comparison between the reported room temperature hydrogen sensors and our Au-SnO₂/rGO device

Ref	Sensing Material	H ₂ %	Response ($\Delta R/R_0$) %	Response time (sec.)	Recovery time (sec.)	Temperature
¹¹¹	Pt-SnO ₂ /rGO	1	200 in 1.5mins	4	3	50
²⁴	Pd-MLGN	0.8	~70	~5	~300	RT
¹⁰⁷	Pd nanowires	1	5.9	16	~50	RT
¹¹⁰	PMMA-Pd-G	1	46	~60	~600	RT
⁵⁰	Pd/SnO ₂ /rGO	1	55	>100	>1800	RT
¹⁰⁸	Pd@ZIF-8	1	3	8	10	RT
¹²⁹	Pd-SnO ₂ /MoS ₂	0.5	18	<30	<20	RT
This work	Au-SnO ₂ /rGO	1	47	60	180	RT

*The hydrogen exposure time for response % calculation are all converted to 5 mins, response time was defined as the time length to reach 90% of the total response in 5mins, recovery time was defined as the time over which 90% of the maximum response % is recovered.

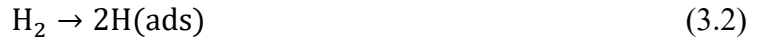
3.3.3 Gas sensing mechanism investigation

To better understand the sensing mechanism, the transfer properties are analyzed with respect to the hydrogen adsorption. The p-type behavior suggests that the dominant charge carriers in the Au-SnO₂/rGO nanocomposite are holes. Both SnO₂ and Au nanoparticles could be regarded as the catalytic materials in hydrogen sensing under different sensing steps. Since SnO₂ is an n-type material and rGO is a p-type material, p-n junctions are formed at the interface. The electrons flow

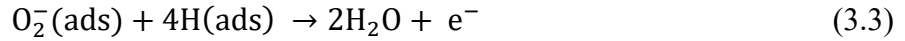
from SnO₂ to rGO nanosheets due to the smaller work function of SnO₂ nanoparticles compared with rGO (Fig. 3.6).^{129, 130} The larger work function differences between Au NPs and SnO₂ NPs compared to SnO₂ NPs and rGO lead to the backflow of electrons from rGO to Au, resulting in the recovery of the conductivity of Au-SnO₂/rGO nanocomposite in the I-V curve (Fig. 3.7a). The electrons on the surface of Au NPs and SnO₂ accelerated the adsorption of oxygen in ambient air. O₂⁻ could be formed on the SnO₂ surface at room temperature.^{131, 132}



Au nanoparticles on the SnO₂ and rGO surfaces could also act as catalytic sites which accelerate the dissociation of H₂ and O₂ molecules.¹¹³



The dissociated hydrogen can migrate and combine with the adsorbed oxygen to form water molecules with the overall reactions as,



The accelerating effect of Au nanoparticles on hydrogen dissociation can give rise to the enhanced response but poor recovery of Au-rGO sensors (Fig. 3.4b). The better recovery of Au-SnO₂/rGO sensors indicates that the loaded Au nanoparticles on SnO₂ are more related to oxygen spillover⁵⁸ rather than hydrogen dissociation, and thus the reactions (3.2) and (3.3) should be present in a small proportion compared to (3.4). The dissociation of hydrogen leads to partial non-recovery at room temperature due to the higher binding energy (Fig. 3.4c). However, the synergistic effect among rGO, SnO₂ and Au nanoparticles promotes the great balance between the sensitivity and recovery performance of sensors.

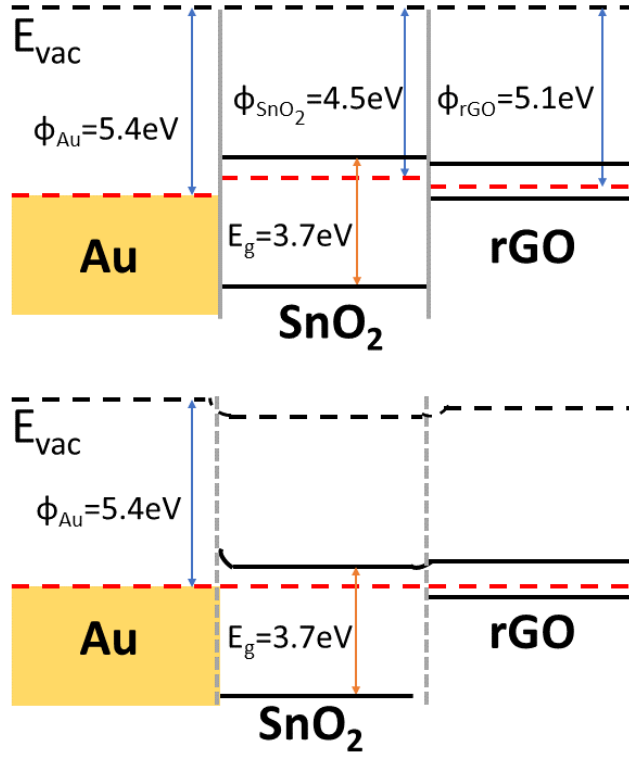


Figure 3.6 Schematic band diagrams of Au-SnO₂/rGO sensors (top figure) with the heterojunction formation at the interfaces (bottom figure).

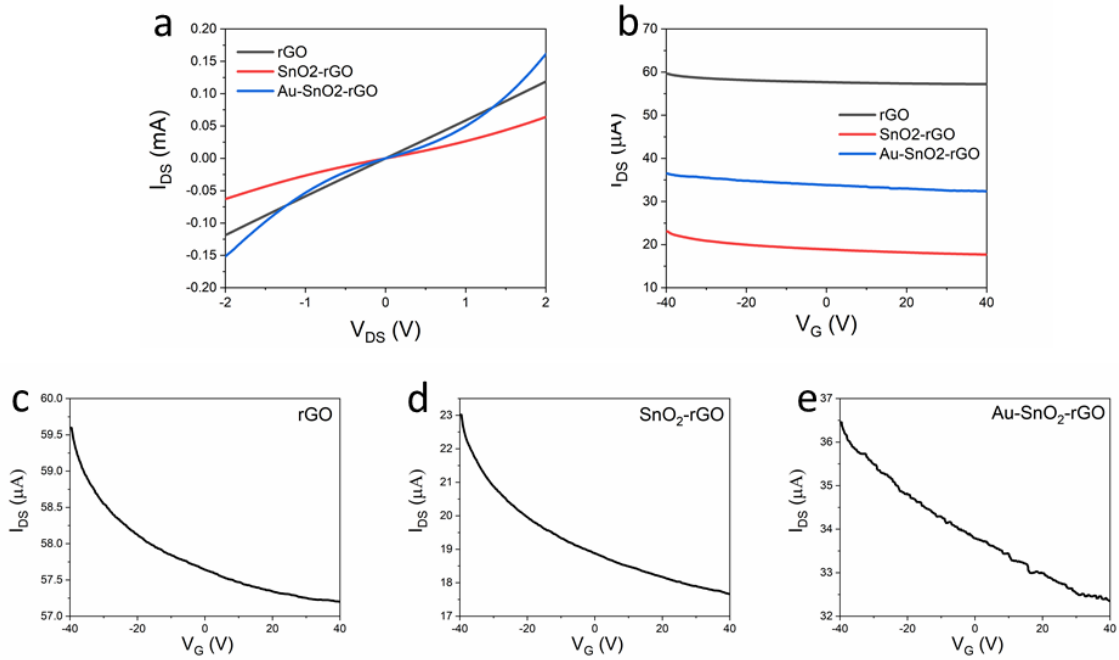


Figure 3.7 a) I-V curve and b-e) FET curves of the rGO, SnO₂-rGO, and Au-SnO₂/rGO sensors.

The enhanced sensing performance facilitated by Au NPs was generally attributed to the catalytic effect of Au NPs on the hydrogen molecular dissociation and the hydrogen spillover effect. However, the acceleration effect of Au NPs on hydrogen adsorption/desorption was rarely investigated kinematically. Arrhenius plots are often used to analyze the effect of temperature on the rates of chemical reactions and determine the related activation energies. Ural and his group extracted the hydrogen desorption activation energy from Pd nanoparticles to reveal the dominant recovery mechanism through Arrhenius plot analysis.²⁴ Weiller et al. determined NO₂ sensor recovery activation energy using the initial slope of the recovery cycle and further understood the binding sites on reduced graphene oxides.²³ In this report, the hydrogen adsorption/desorption kinetics were extracted and analyzed through a temperature-dependence study and the Arrhenius plot analysis, which refines the understanding of the observed acceleration effect of gold nanoparticles on hydrogen sensing.

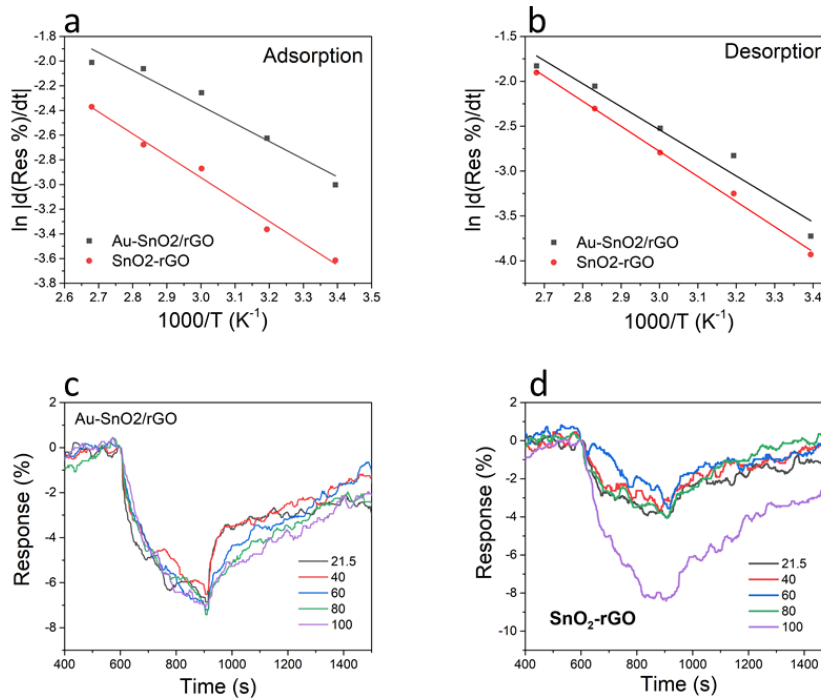


Figure 3.8 a-b) The Arrhenius plot of $\ln |d(\text{Res \%})/dt|$ determined from the initial slope of the recovery cycle. Dynamic response curves of c) Au-SnO₂/rGO and d) SnO₂-rGO sensors to 1% H₂ in the temperature range 21.5-100 °C.

The temperature-dependent sensing test was conducted to analyze the adsorption and desorption kinetics quantitatively.¹³³ Figure 3.8a-b shows the Arrhenius plot of the rate of relative current change determined from the initial slope of the response and recovery cycle from room temperature 21.5 °C (RT) to 100 °C. The activation energies, E_a , for hydrogen adsorption are extracted as 152.9 meV (SnO₂-rGO) and 124.0 meV (Au-SnO₂-rGO). The E_a of SnO₂-rGO and Au-SnO₂-rGO for hydrogen desorption are also extracted as 241.0 meV and 221.6 meV, respectively. The sensors with loaded Au nanoparticles indicate reduced activation energies in both hydrogen adsorption and desorption. The reduction in the activation energy for desorption leads to a shorter recovery time (~600 s) than that of SnO₂-rGO (>600 s) at varying temperatures.



Figure 3.9 Prototype handheld device with the demonstration results.

A hydrogen detection prototype handheld device (Figure 3.9) was further developed. Based on the calibration data (Fig. 3.4f), a portable digital meter was programmed. The digital meter was tested against 0.04%, 0.1%, 0.4%, and 1% hydrogen diluted with compressed air in the gas chamber. The

real responses of the handheld device are very close to the standard values (Fig. 3.9) with errors within $\pm 20\%$.

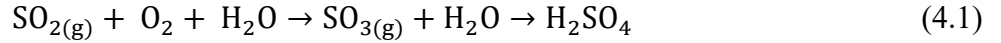
3.4 Conclusion

In summary, the Au-SnO₂/rGO ternary nanohybrids were designed with improved room temperature H₂ sensing performance. The sputtered Au nanoparticles enhanced both sensitivity and recovery of the SnO₂-rGO template. Such an enhancement was attributed to the increased surface area and the oxygen ions spillover effect of loaded Au nanoparticles. The catalytic effect of Au nanoparticles for hydrogen adsorption and desorption was then revealed through the temperature-dependent sensing test and Arrhenius analysis. Better balance between sensitivity and recovery can be further achieved in the future by tuning the deposition conditions of Au nanoparticles. A prototype handheld device based on the Au-SnO₂/rGO composites was finally developed for hydrogen detection. This prototype device demonstrates the potential for real-time hydrogen monitoring. The availability of such sensors will contribute to promoting a sustainable hydrogen economy, protecting public safety, and enhancing lead-acid battery safety in a wide range of applications.

CHAPTER 4. TERNARY NI DOPED TIN OXIDE-RGO NANOCOMPOSITES FOR SULFUR DIOXIDE SENSING

4.1 Introduction

Sulfur dioxide (SO₂) is one of the most common air pollutants generated from thermal power plants, industrial complexes, and vehicles. The interaction of SO₂ with moist air results in acid rain (equation 4.1), which has significant impacts on the environment.



The Clean Air Act requires the United States Environmental Protection Agency (EPA) to set national ambient air quality standards (NAAQS) for sulfur dioxide and five other pollutants considered harmful to public health and the environment. An SO₂ concentration of 100 ppm was suggested to be immediately dangerous to health by the U.S. National Institute for Occupational Safety and Health. The threshold limit of short-time exposure and long-time exposure is 5 and 2 ppm, respectively. Therefore, it is necessary to monitor the ppm levels of SO₂ in real-time.

SnO₂-based materials were investigated for sensitive SO₂ detection.¹³⁴⁻¹³⁶ However, the high operating temperature is a disadvantage with respect to power consumption and long-time stability. Pure reduced graphene oxide was investigated for room temperature SO₂ sensing by Kaur et al.¹³⁷ The rGO-based sensor indicated reasonable p-type response down to 5 ppm and good stability. The combination of rGO with SMOX¹³⁸ or other carbon materials¹³⁹ showed low concentration SO₂ detection capability. In conclusion, carbon-based materials, especially rGO-based heterostructures, exhibited promising room temperature SO₂ sensing properties. However, there is still much room for improvement in the sensitivity ((R_a-R_g)/R_a) of these sensors (average 1.28% ppm⁻¹). The best performance in sensitivity was reported on rGO-SnO.^{2,39} The selectivity was

improved through Ni doping ($\text{NiO}^{134, 135}$ & NiS^{140}). A comparison of the chemiresistive SO_2 sensors is listed in Table 4.1. Based on the reported results, the introduction of Ni additives into the SnO_2 -rGO sensing platform is promising to achieve sensitive, stable, and selective SO_2 sensing performance at room temperature.

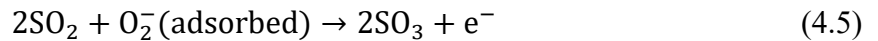
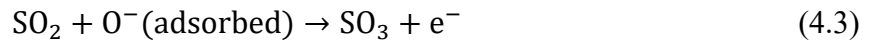
Table 4.1 Comparison of the chemiresistor sensing performance towards SO_2

Materials	Sensitivity	Response time	Recovery time	Selectivity	Limit of detection	Temp ($^{\circ}\text{C}$)	Ref
SnO_2 thick film mixed MgO and V_2O_5 (n-type)	44.2% \downarrow (1ppm) $(R_a - R_g)/R_a$	$\sim 180\text{s}$	625s (70%)	N/A	0.1ppm	400	136
NiO/SnO_2 (n-type)	55 \downarrow (500ppm) $(R_a - R_g)/R_g$	80s	70s	Acetone CO_2 Methane	50ppm	180	134, 135
rGO- SnO_2	22 (500ppm) $(R_a - R_g)/R_g$	144s	210s	CH_4 , CO_2	10ppm	60	39
rGO (p-type)	5.93% \downarrow (5ppm) $(R_a - R_g)/R_a$	110s	170s	H_2S	5ppm	RT	137
g- $\text{C}_3\text{N}_4/\text{rGO}$ (n-type)	3% \downarrow (2ppm) $(I_g - I_a)/I_a$	207s	212s	N/A	0.685ppm	RT	139

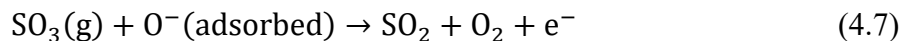
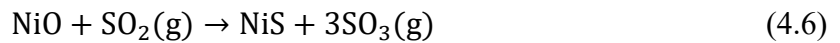
Ni-MoS ₂ (p-type)	7.4%↓ (5ppm) (R _a -R _g)/R _a	50s	56s	CO ₂ , H ₂ , CO	0.25ppm	RT	140
CoZn-NCNTs (p-type)	28.9%↓ (30ppm) (R _a -R _g)/R _a	78s	~300s	NH ₃ , NO ₂ , CO	0.5ppm	RT	141
TiO ₂ /rGO	10.1%↓ (1ppm) (R _a -R _g)/R _a	73s	128s	N/A	1ppb	RT	138

The sensing reactions of traditional SMOX and rGO towards SO₂ were shown in equation 4.2-4.8. Different types of sensing mechanisms were proposed on SO₂ sensing. For the ionized oxygen-involved sensing mechanism (traditional metal oxide), SO₂ reacts with the oxygen ions, which transfers electrons back to the metal oxide, just like a reducing gas. For the direct charge transfer sensing mechanism, SO₂ as an oxidizing gas extracts or consumes the electrons from the materials, which is anticipated for oxidizing gases.

n-type metal oxide (SnO₂, TiO₂)^{134, 138, 142}:



p-type Nickel oxide (NiO)¹³⁴:



Reduced graphene oxide^{137, 139}, MoS₂¹⁴⁰:



4.2 Experimental Method and Results

4.2.1 Pure rGO gas sensors for SO₂ sensing

4.2.1.1 Material synthesis and sensor fabrication

The pure rGO sensors were fabricated with the purchased commercial graphene oxide (GO). First, 2 μ l AET solution was drop cast on the clean gold electrode for 15 minutes. After being washed with DI water and dried, the modified electrodes were immersed into the 0.01mg/ml GO solution for three different time periods (10s/20s/30s). Then the electrodes were annealed at 400 °C for 5 minutes to improve the electrical contact and to reduce GO.

The fabrication process of holey rGO (HGO) devices is described as follows. First, 2.5 mg of GO was homogeneously dispersed in 0.75 ml of DI water with sonication. Then, 0.25ml (#1 sample)/0.325 ml (#2 sample) of 30% H₂O₂ solution was added to the GO dispersion separately, and the mixture was stirred by a magnetic bar at 100 °C for 10h. A centrifugation process was conducted three times with DI water, and purified holey GO was redispersed in DI water. 0.01 mg/ml of GO dispersion was prepared for device fabrication. 2 μ l GO dispersion was drop cast on the electrodes and dried at room temperature. Another type of device was fabricated with the assistance of AET solution; 2 μ l AET solution was drop cast on the clean gold electrode for 15 minutes. After being washed with DI water and dried, the modified electrodes were immersed into the 0.01mg/ml GO solution for 15 s. All dried devices were annealed at 400 °C for 5 minutes. Then, HGO#1Drop, HGO#1AET, HGO#2Drop, and HGO#2AET were fabricated.

4.2.1.2 Electrical properties of pure rGO gas sensors

The linear I-V curves below indicate the good electrical contact between rGO nanosheets and gold electrode fingers.

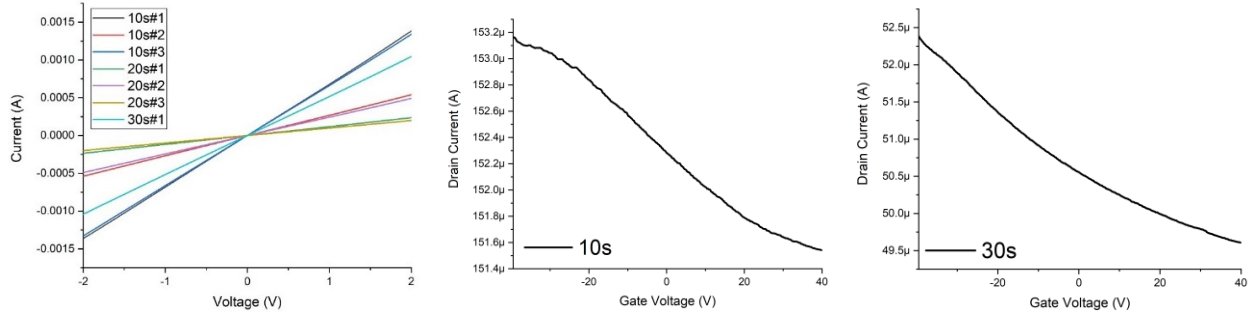


Figure 4.1 I-V curve and field-effect properties of rGO sensors.

The field-effect properties of the rGO sensors were tested by sweeping the gate voltage from -40V to 40V. The on/off ratios of the rGO sensors are all less than 1.1.

The field-effect properties of the HGO devices are shown in Figure 4.2. As expected, holey GO samples indicated a higher FET on/off ratio (1.2 on average) than pure rGO samples, as we proposed.

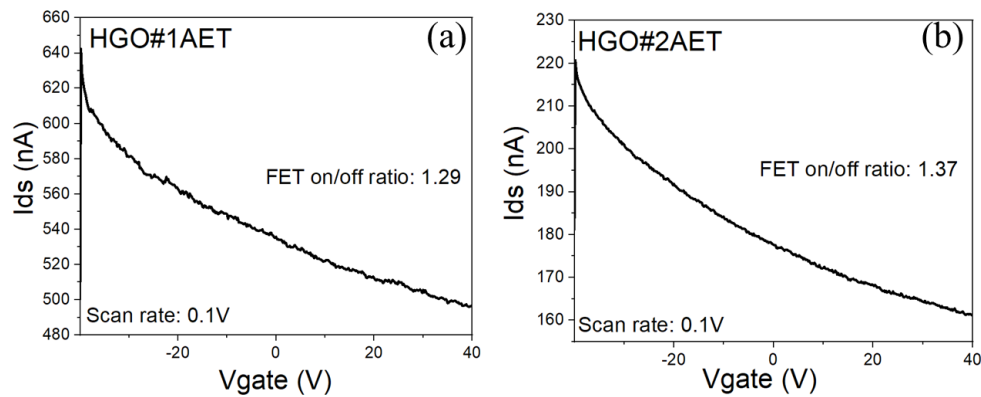


Figure 4.2 FET curves of HGO samples.

4.2.1.3 Gas sensing results and discussion

One typical gas sensing test cycle had three continuous steps: First, a clean carrier gas flow was introduced into the sensing chamber as the baseline of the test. Typically, the preset time for this

step is 10 minutes or even longer till the baseline of current becomes stable. Second, different target gases diluted in the carrier gas were injected through the flowmeter into the test chamber with the same flow rate as the first step to generate the sensing signal. The exposure time for the target gas was 5 minutes. Finally, the target gas was turned off, and the carrier gas was introduced again for sensor recovery for 10 minutes.

Different concentrations of sulfur dioxide were diluted and injected into the gas chamber. The sensitivity of pure rGO sensors indicated in Figure 4.3 below could be extracted. There are no obvious differences between the three series of sensors. The responses% are $\sim 2.5\%$ (10ppm) and $\sim 0.5\%$ (5ppm), respectively. All the rGO sensors did not respond to 1ppm sulfur dioxide.

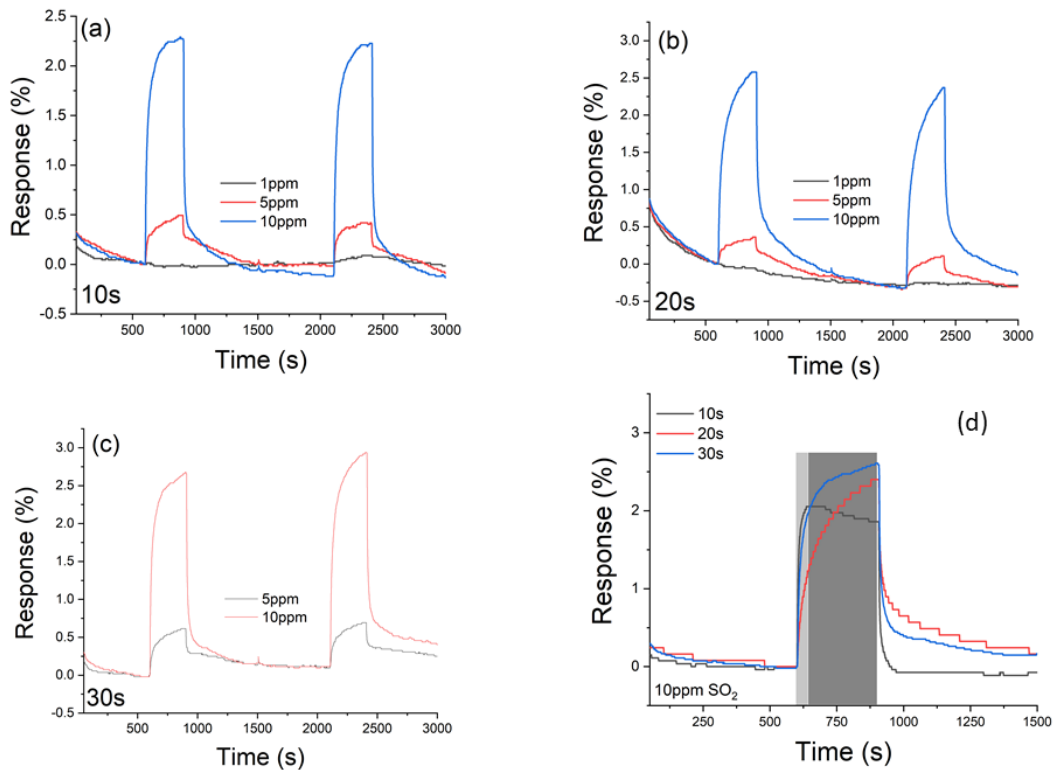


Figure 4.3 SO₂ sensing performance of a) 10s, b) 20s, c) 30s, and d) rGO sensor performance comparison.

Through the comparison of the sensing curves (Fig. 4.3), we can see that the response speed during the target gas injection was different between the three series of sensors. This might be related to

the different ratios between the low energy binding sites and high energy binding sites within these three series of sensors.

Ideally, the sensor would operate under ambient conditions because raising or lowering the temperature would increase the complexity and cost of the sensor. Fortunately, the sensor performed much better under ambient temperatures than at elevated temperatures, as shown in Figure 4.4. Figure 4.5 shows the sensing response of holey GO samples against 1ppm SO₂. HGO samples did not indicate an improved resistive response even with better FET performance.

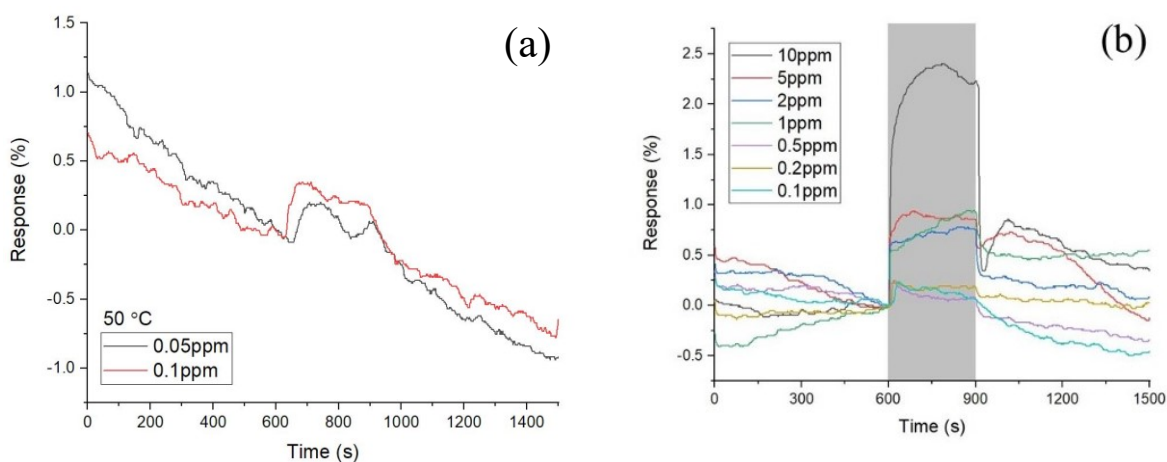


Figure 4.4 (a) rGO sensor response upon exposure to 0.05 ppm and 0.1 ppm SO₂ at 50°C and (b) upon exposure to a range of concentrations of SO₂ under ambient temperatures.

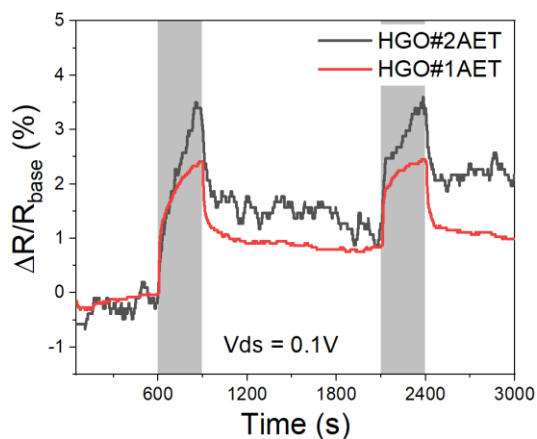


Figure 4.5 SO₂ sensing curves of holey GO samples.

4.2.2 rGO-based binary nanocomposites gas sensors for SO₂ sensing

4.2.2.1 Material synthesis and sensor fabrication

Two types of SnO₂-rGO were fabricated: one type through a hydrothermal synthesis method and the other type through a facile wet chemistry method. The hydrothermal method was prepared as follows. 10 ml of GO (0.9 mg/ml) suspension was sonicated for 30 min to form a homogeneous solution. Simultaneously, 14.5 mg of SnCl₂•2H₂O and 13.5 mg of urea were dissolved into 20 ml of deionized (DI) water under magnetic stirring for 10 min at room temperature. Then the prepared GO solution was added dropwise into the tin precursor solution under vigorous stirring for an hour. Subsequently, the colloidal solution was transferred to a 50 ml Teflon-lined stainless-steel autoclave and heated at 180 °C for 16 h. After cooling down, the composite was washed with deionized water three times and collected with the centrifuge. Then, 10 ml of SnO₂-rGO#1 suspension was prepared for drop cast sensor fabrication. The wet chemical method of SnO₂-rGO#2 was prepared by in situ hydrolysis of Sn²⁺ on GO, using polydiallyldimethylammonium chloride (PDDA) as the surfactant to mitigate agglomeration of the formed hybrid: 10 ml of GO (0.5 mg/ml) and 0.2 ml of PDDA were mixed together and sonicated for 15 min to form a homogeneous suspension. Subsequently, 0.07 ml of HCl (36 wt%) and 15 mg of SnCl₂•2H₂O were added. The mixture was vigorously stirred at 90 °C for 1 h. The resulting stable black suspension was centrifuged and washed with DI water three times. Finally, the obtained SnO₂-rGO#2 was dispersed in 5 ml of DI water for further use.

The general process of sensor fabrication for both types of SnO₂-rGO is similar. A 2 µl SnO₂-rGO suspension was drop cast on the clean gold electrodes and dried at room temperature. Then the electrodes were annealed in Ar at 400 °C for 5 min to reduce GO and improve the electrical contact between the electrodes and our materials. Additionally, a batch of SnO₂-rGO#1 sensors were

annealed in Ar at 200 °C for 1h to understand the influence of different annealing conditions on the sensing performance.

In a typical synthesis process of NiO-rGO composites, 40 ml of GO (0.5 mg/ml) was sonicated to form a homogeneous solution. Then 0.45 g $\text{Ni}(\text{NO}_3)_2 \cdot 6\text{H}_2\text{O}$ and 0.07 g urea were slowly added into the above aqueous solution under magnetic stirring. Subsequently, the homogeneous solution was transferred into a Teflon-lined stainless-steel autoclave and maintained at 120 °C for 24 h. After being allowed to cool to room temperature, the target products were completely washed and centrifuged with DI water three times. Then, the products were fully dried at 60 °C for 24 h and calcined at 250 °C in Ar. The NiO-rGO was dispersed in 20 ml of DI water for sensor fabrication. 2 μl NiO-rGO suspension was drop cast on the gold electrodes and dried at room temperature. Then the electrodes were annealed in Ar at 400°C for 5 min.

4.2.2.2 Sulfur dioxide sensing results and discussion

The carrier gas for the sensing test was argon. Different concentrations of sulfur dioxide were diluted and injected into the gas chamber. All three series of SnO_2 -rGO sensors show partial recovery after being exposed to 5 ppm SO_2 , as shown in Figure 4.6a-c. They all indicate a typical p-type metal oxides response as the resistance increased while exposed to sulfur dioxide which suggests the rGO is the main semiconducting conductive channel between the electrode fingers. SnO_2 -rGO#1 annealed at 200°C for 1h shows a higher and more stable response (~2% @ 1ppm) than the sensors that were annealed under argon at 400°C (~0.7% @ 1ppm). SnO_2 -rGO#2 (Figure 4.6c) sensors had the most stable signal with the highest sensitivity among all three types of SnO_2 -rGO sensors. Figure 4.6c indicates the repeatable sensing curves against 1 ppm SO_2 at the

sensitivity of ~4%. The sensitivity against 1 ppm SO₂ improved from ~0.1% (pure rGO) to ~4% (SnO₂-rGO#2).

NiO and rGO are typically p-type semiconductor materials when applied as gas sensors because of the main carrier holes. However, NiO-rGO sensors indicate a typical n-type metal oxides response (Figure 4.6d) as the conductivity increased when the sensors were exposed to sulfur dioxide. This might be due to the different sensing mechanisms of NiO and rGO, as shown in Equations 4.7 and 4.8, respectively. The electrons transferred from NiO to rGO due to the higher Fermi level of the NiO, which decreased the concentration of major carriers and created lower electron conductivity in the rGO conducting channel. With more electrons accumulated in rGO, the dominant sensing mechanism is that SO₂ extracted electrons from rGO and increased the concentration of major carrier holes, increasing the conductivity. The sensitivities of NiO-rGO sensors are ~75% (1 ppm) and ~5.5% (0.1 ppm), respectively. Partially recovered curves appear even for 0.1 ppm SO₂, which indicates the much stronger binding between the composite and gas molecules. This result suggests the potential for detecting lower concentrations of sulfur dioxide under ambient conditions.

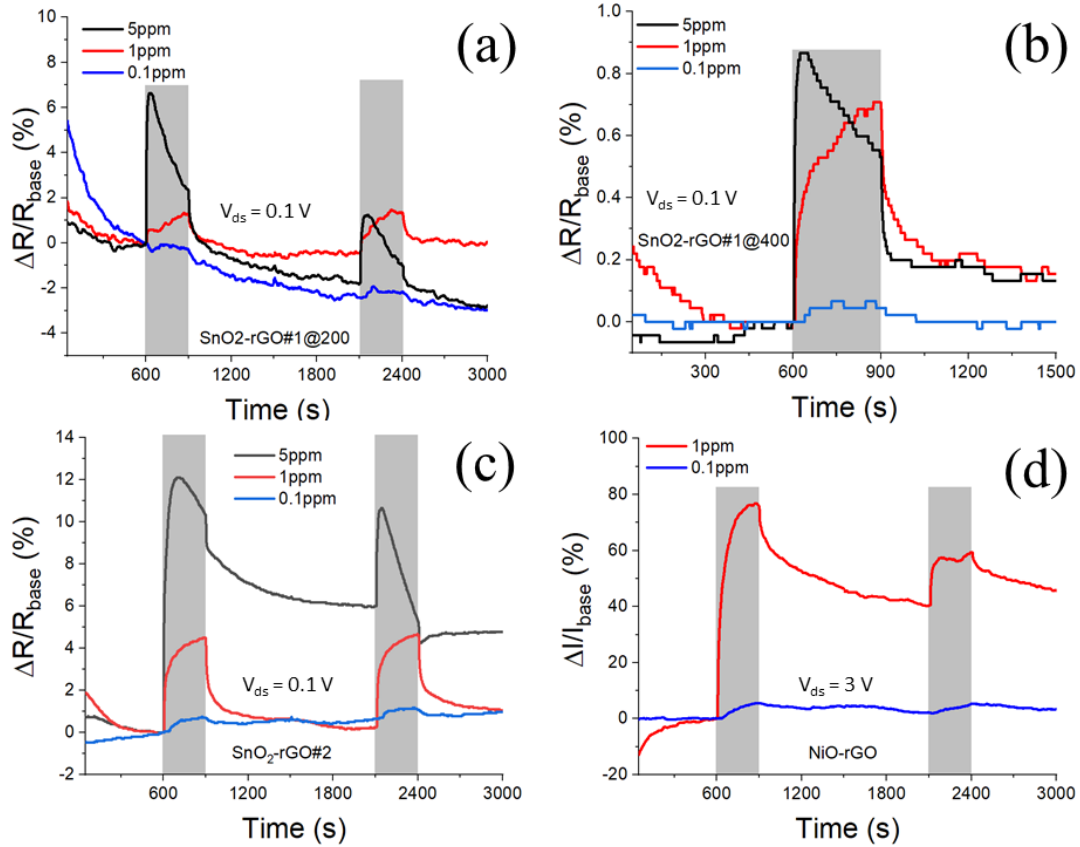


Figure 4.6 SO₂ sensing performance of (a) SnO₂-rGO#1@200, (b) SnO₂-rGO#1@400, (c) SnO₂-rGO#2, and (d) NiO-rGO.

4.2.3 Control experiment on rGO-based binary gas sensors

4.2.3.1 Material synthesis and sensor fabrication

We synthesized two control samples of SnO₂-rGO#Wet through the same facile wet chemistry method mentioned before. The SnO₂-rGO#Wet control samples were prepared by in situ hydrolyses of Sn²⁺ on GO, using PDDA as the surfactant to assist the dispersibility of the formed hybrid: 10 ml of GO (0.5 mg/ml) and 0.2 ml of PDDA were mixed together, followed by ultrasonication for 15 min to form a homogeneous suspension. Subsequently, 0.07 ml of HCl (36 wt%) and 30 mg (wet2 sample)/7.5 mg (wet3 sample) of SnCl₂•2H₂O were added separately. The mixture was vigorously stirred at 90 °C for 1 h. Then, the resulting stable black suspension was

centrifuged and washed with DI water three times. Finally, the obtained SnO₂-rGO#Wet2 and SnO₂-rGO#Wet3 were dispersed in 5 ml of DI water for further use separately.

The general process of sensor fabrication is described as below. 2 μ l SnO₂-rGO suspension was drop cast on the clean gold electrodes and dried at room temperature. Then the electrodes were annealed in Ar at 200 °C for 1 hour to reduce GO and improve the electrical contact between the electrodes and our materials.

In typical synthesis of NiO-rGO composites, 10 ml of GO (0.5 mg/ml) was sonicated to form a homogeneous solution. Then 112.5 mg (#1 sample)/56.25 mg (#2 sample)/225 mg (#3 sample) Ni(NO₃)₂•6H₂O and 12.5 mg urea were slowly added into the above aqueous solutions under magnetic stirring separately. After that, the homogeneous solutions were transferred into Teflon-lined stainless-steel autoclaves and maintained at 120 °C for 24 h. After being cooled to room temperature, the target products were thoroughly washed and centrifuged with DI water three times. Then, the products were fully dried at 60 °C for 24 h and calcined at 250 °C in Ar for 1 h. Finally, the obtained NiO-rGO#1, NiO-rGO#2, and NiO-rGO#3 samples were dispersed in 5 ml of DI water for sensor fabrication separately. 2 μ l NiO-rGO suspension was drop cast on the gold electrodes and dried at room temperature. Then the electrodes were annealed in Ar at 400°C for 5 min.

4.2.3.2 Characterization and discussion

The I-V curves shown in Figure 4.7 indicate the formation of good contact between composites and gold electrode fingers because they are almost completely linear.

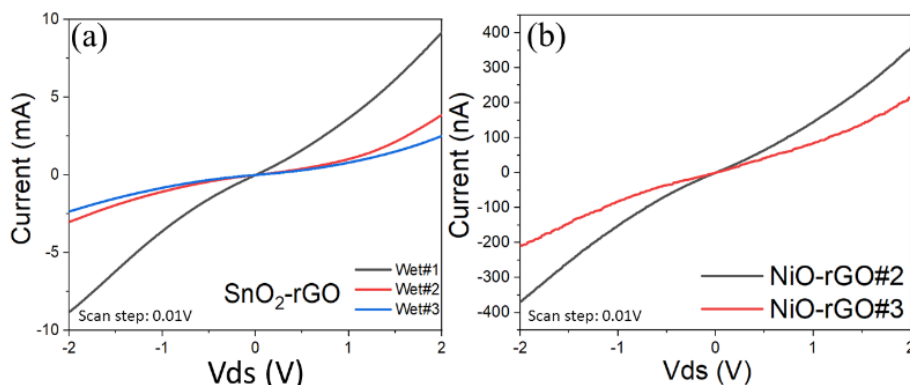


Figure 4.7 I-V curves of (a). SnO_2 -rGO and (b). NiO-rGO composite sensors.

The XRD results of three SnO_2 -rGO samples are shown in Figure 4.8a. The low signal-to-noise ratio indicates the low crystallinity of these three samples, which might be due to the short-time powder grounding in sample preparation and lack of heat treatment (powder samples were collected before sensor annealing). All intensive peaks of these three samples can be well indexed to Cassiterite SnO_2 (COD: 96-100-0063), suggesting the successful formation of SnO_2 crystals.

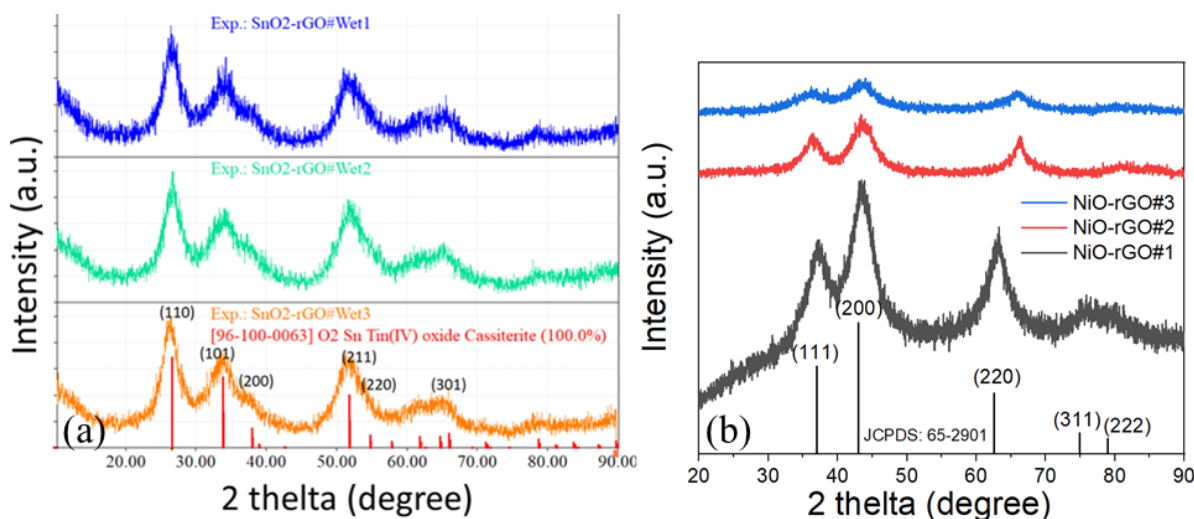


Figure 4.8 XRD patterns of (a) three SnO_2 -rGO samples and (b) three NiO-rGO samples.

Figure 4.8b shows the XRD patterns of the NiO-rGO samples. All three samples indicated the typical peaks at 37.1° , 43.1° , 62.6° , 75.0° , and 79.0° which can be indexed to (111), (200), (220),

(311), and (222) crystal planes of a NiO phase, respectively, which matches well with the standard pattern (JCPDS: 65-2901).

Figure 4.9a shows the survey spectral of three SnO₂-rGO samples, indicating that Sn, O, and C are major elements of these samples. There are no obvious differences in each element's electronic state between these three samples. Figure 4.9b shows the Sn 3d_{5/2} and 3d_{3/2} spectra of SnO₂-rGO#Wet1 sample. The binding energies of Sn 3d_{5/2} and 3d_{3/2} are identified as 486.7 and 495.2 eV, respectively.¹⁴³ The wideband shown in Figure 4.9c can be subdivided into four XPS peaks centered at 284.4, 285.2, 286.2, and 288.9 eV, corresponding to C-C/C=C, C-O, C-O-C/C=O, and O-C=C groups of rGO, respectively.¹⁴⁴ Figure 4.9d shows the O 1s spectrum of the SnO₂-rGO#Wet1 sample. The O 1s XPS peak can be decomposed into three Gaussian components centered at about 530.6, 531.8, and 533.1 eV, respectively; the above three components can be indexed to O²⁻ ions in SnO₂ lattice (O_L), ions in oxygen-deficient regions (O_V), and chemisorbed oxygen (O_C) species and -OH groups, respectively.¹⁴⁵ Table 4.2 indicates the atomic percentage of each element in these three samples. The variation of the atomic percentage of Sn element within these three samples is less than 1%.

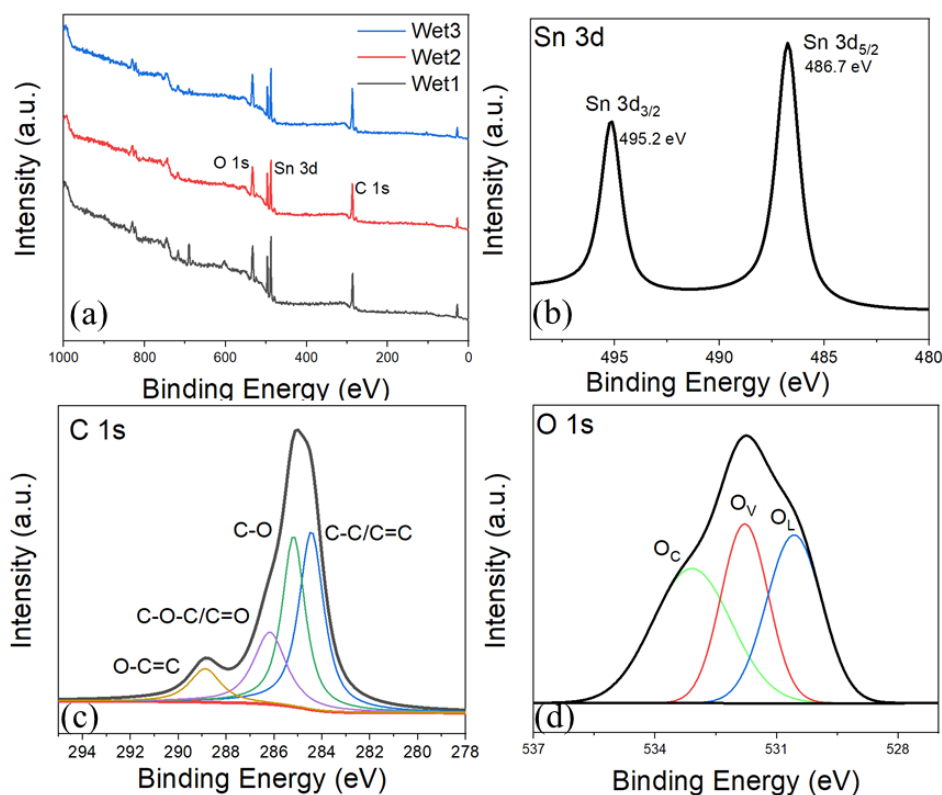


Figure 4.9 XPS spectra of SnO₂-rGO: (a) survey scan of three samples, (b) Sn 3d of SnO₂-rGO#Wet1, (c) C 1s of SnO₂-rGO#Wet1, (d) O 1s of SnO₂-rGO#Wet1.

Table 4.2 Atomic % of three SnO₂-rGO samples

Atomic %	C	O	Sn
SnO ₂ -rGO#Wet1	69	26.4	4.6
SnO ₂ -rGO#Wet2	71.7	23.2	5.1
SnO ₂ -rGO#Wet3	72.1	23.9	4.0

The survey spectra of three NiO-rGO samples are shown in Figure 4.10a. The sharp peaks of O 1s and C 1s are located at around 530 eV and 285 eV, respectively. The spectra of C 1s are shown in Figure 4.10b, with four main peaks at 284.3, 285.4, 286.9, and 288.4 eV associated with C-C, C-O, C=O, and O-C=C groups, respectively.¹⁴⁶ As shown in high-resolution XPS of NiO-rGO#2 (Fig. 4.10c), the Ni 2p_{3/2} and Ni 2p_{1/2} spin-orbit of NiO were observed at 856 eV and 873 eV, respectively.¹⁴⁶

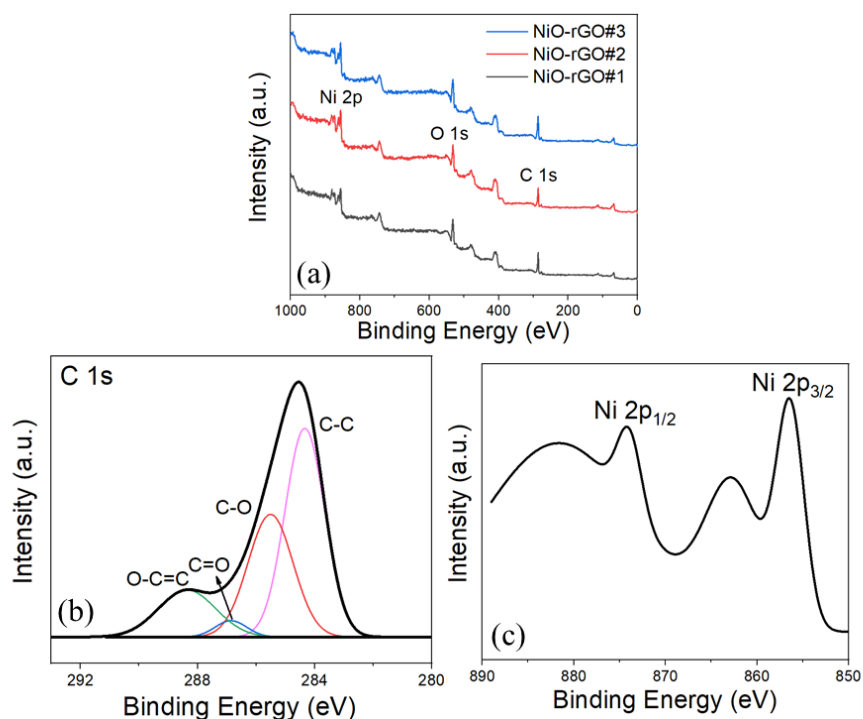


Figure 4.10 XPS spectra of NiO-rGO: (a) survey scan of three samples, (b) C 1s of NiO-rGO#2, (c) Ni 2p of NiO-rGO#2.

4.2.3.3 Sulfur dioxide sensing results and discussion

The sulfur dioxide sensing curves of SnO₂-rGO are shown in Figure 4.11a-c. SnO₂-rGO#Wet1 sensor shows a higher response against 5 ppm SO₂ than the other two samples but indicates partially recovered performance. They all indicate a typical p-type response as the resistance increased while sulfur dioxide was injected. There are no obvious differences in the lower concentration sensing curves among all three samples. This could be related to the small Sn component variations among these samples, as shown in Table 4.3.

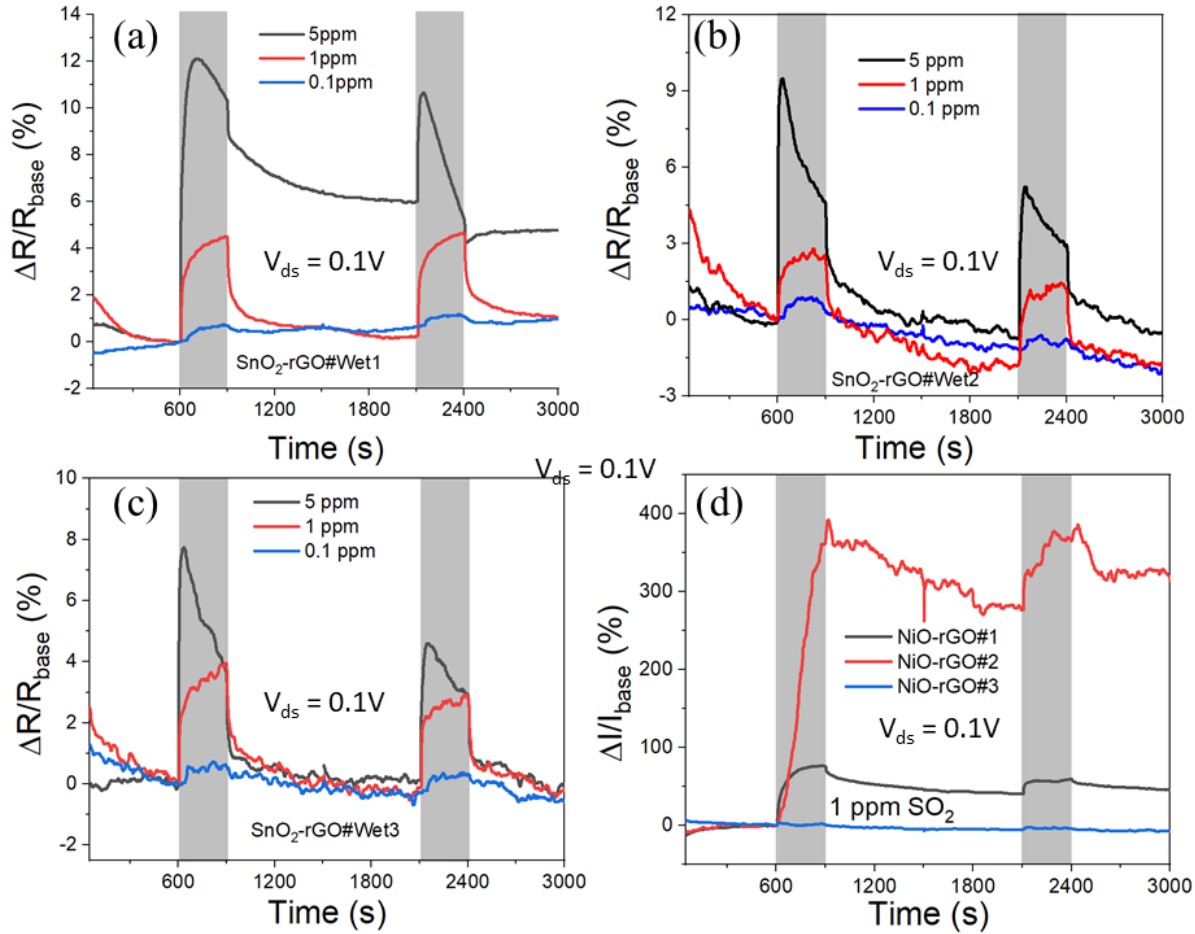


Figure 4.11 SO₂ sensing performance of (a) SnO₂-rGO#Wet1, (b) SnO₂-rGO#Wet2, (c) SnO₂-rGO#Wet3, and (d) NiO-rGO.

Figure 4.11d shows the typical sensing curve of three NiO-rGO samples against 1 ppm SO₂. The NiO-rGO#2 sensors, which contain a higher amount of Ni indicate extraordinary response during the sensing cycle. The sensitivity reaches around 400% at room temperature. This result is quite promising for NiO doped sensors to achieve a ppb level detection limit with further optimization.

4.2.4 SnO₂-rGO based ternary nanocomposites gas sensor

4.2.4.1 Material synthesis and sensor fabrication

We synthesized two types of ternary nanocomposites and fabricated the associated sensors for sulfur dioxide sensing. For NiO-SnO₂/rGO nanocomposites, we synthesized the SnO₂-rGO first

through the facile wet chemistry method, as we mentioned before. Then we drop cast tiny amounts of purchased NiO nanoparticles (Sigma) onto the sensor surface.

The Ni/SnO₂-rGO ternary nanocomposite was prepared through a direct hydrothermal synthesis process. 500 mg of Ni (Ac)₂•4H₂O, 360 mg of SnCl₂•2H₂O, and 1.125 g of urea were dissolved in 30 ml of DI water by vigorous stirring to form a clear solution. The resulting compound was transferred into a Teflon-lined stainless-steel autoclave and maintained at 100 °C for 6 h. The product was collected by centrifugation and rinsed with DI water, then dried overnight. Then, the powder product was annealed in the tube furnace at 600 °C in Ar atmosphere for 5 h. Finally, 100 mg of the final product (Ni/SnO₂) was dissolved in 10 ml DI water and 2 µl of sample was drop cast on the rGO sensor (Ni/SnO₂-rGO#1), which was fabricated through cysteamine (AET) functionalization. The 10 mg/ml NiO-SnO₂ dissolution was further diluted to 0.1 mg/ml (Ni/SnO₂-rGO#2) and 0.001 mg/ml (Ni/Sn O₂-rGO#3) for drop casting as the control sample.

4.2.4.2 Characterization and discussion

The pure monolayered rGO nanosheet bridging the gold fingers is shown in Figure 4.12a. Figure 4.12b demonstrates the SnO₂-rGO synthesized through the wet chemistry method. The two-dimensional property of the rGO remained after the SnO₂ doping. Figure 4.12c-d shows the different loading amounts of Ni/SnO₂ nanocomposite doped on the rGO surface. We could observe a nearly porous layer of Ni/SnO₂ was formed between the gold fingers with the highest loading amount in Figure 4.12d.

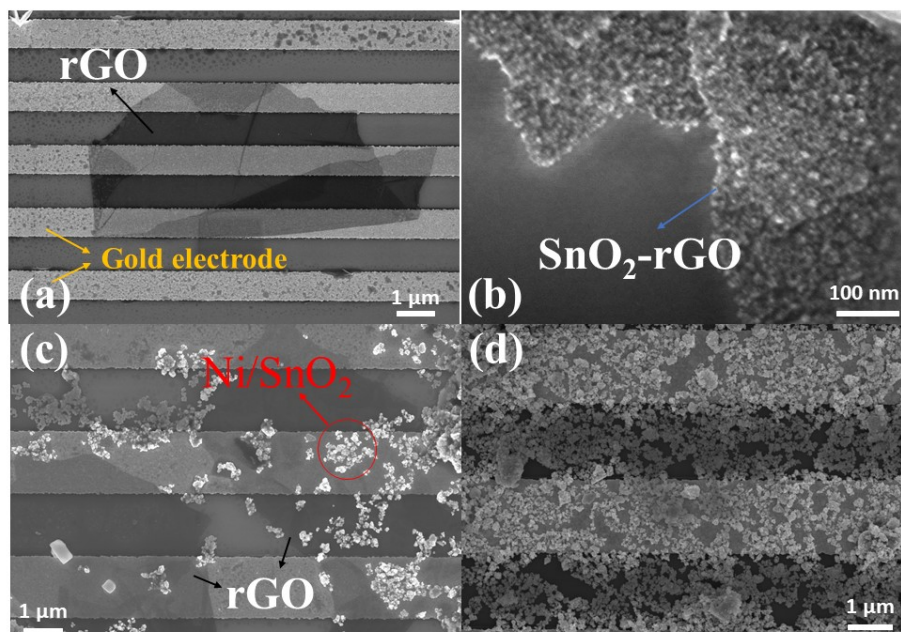


Figure 4.12 SEM images of a) pure rGO nanosheet, b) SnO_2 -rGO, c) Ni/ SnO_2 -rGO#2, and d) Ni/ SnO_2 -rGO#1.

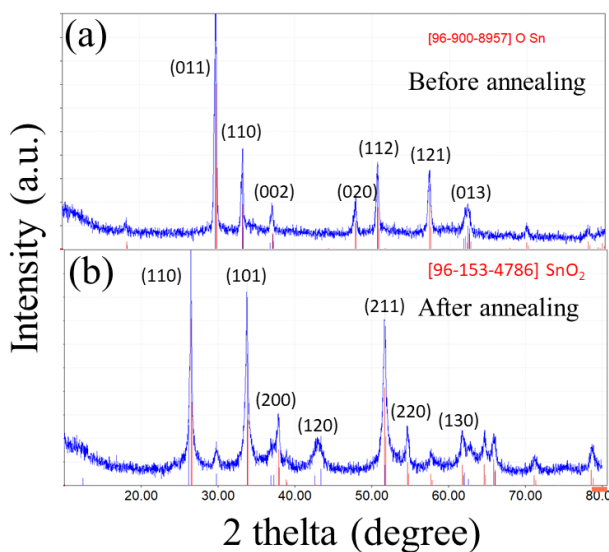


Figure 4.13 XRD patterns of a) NiSn composite before annealing, b) NiSn composite after annealing.

The XRD results of NiSn nanocomposite before and after annealing are shown in Figure 4.13. All intensive peaks in Figure 4.13a can be well indexed to SnO (COD: 96-900-8957). The XRD pattern shown in Figure 4.13b suggests the formation of SnO_2 (COD: 96-153-4786), which indicates the

oxidation of tin oxide during annealing. There is no feature peak of Ni shown in the pattern; this may suggest the unsuccessful crystallization of nickel oxide.

The EDS spectra of Ni/SnO₂-rGO#2 sensors shown in Figure 4.14 indicate the existence of nickel element and no other impurity in the sensing layer. Table 4.4 indicates the relative atomic % of each element on the sensor surface. The signal of silicon comes from the surface silicon oxide layer of the electrode.

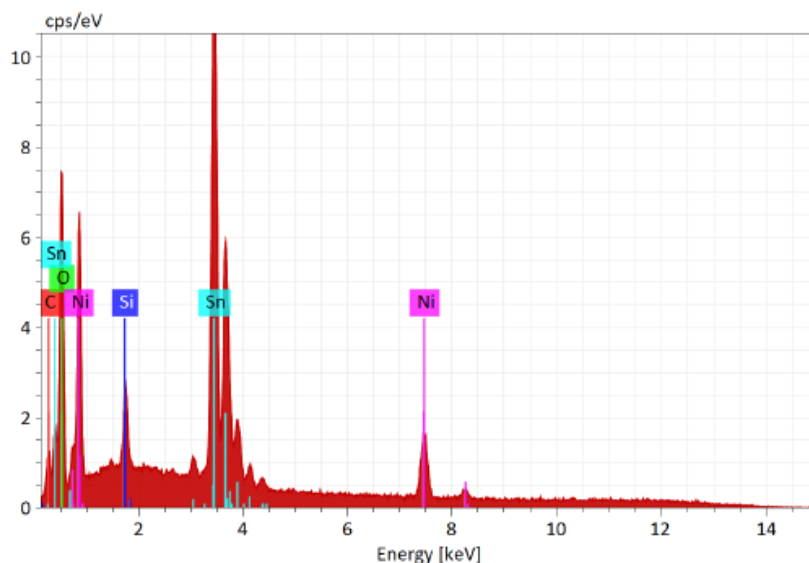


Figure 4.14 EDS spectra of Ni/SnO₂-rGO#1 sensors

Table 3.3 Atomic % of Ni/SnO₂-rGO#1

Atomic %	Silicon	Carbon	Oxygen	Tin	Nickel
Ni/SnO ₂ -rGO#1	2.67	11.93	57.91	17.79	9.7

4.2.4.3 Sensing results and discussion

Figure 4.15a shows the typical sensing curve of NiO-SnO₂/rGO ternary nanocomposite sensors. The response % slightly decreased after NiO nanoparticle drop-casting compared with the pure SnO₂-rGO sensors. This phenomenon may be explained as the competing sensing mechanism between the p-type NiO and n-type SnO₂, which generated opposite current change in rGO. The

dynamic response curves of three Ni/SnO₂-rGO samples against 0.1 ppm sulfur dioxide are shown in Figure 4.15b. The Ni/SnO₂-rGO#1 with the porous layer morphology demonstrates considerable enhancement in the sensing response (~5%). This enhancement may be due to the large surface-to-volume ratio and more adsorption sites on the surface offered by the porous structure. Figure 4.15c shows the multi-cycle response of Ni/SnO₂-rGO#1 against 4 ppb SO₂, which indicates the excellent stability of the sensor even at the ppb level.

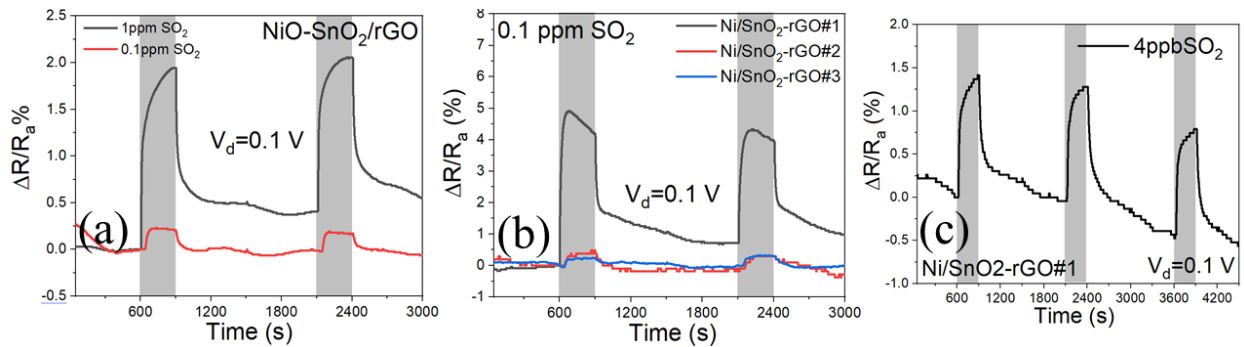


Figure 4.15 Sulfur dioxide sensing performance of a) NiO-SnO₂/rGO, b) Ni/SnO₂-rGO samples, and c) multi-cycle sensing of Ni/SnO₂-rGO sensor against 4 ppb SO₂.

Figure 4.16a indicates the dynamic response of SnO₂-rGO against sulfur dioxide and ammonia gas separately. The response to 0.1 ppm SO₂ is ~0.8%, and the response to 10 ppm NH₃ is ~0.1%, which gives the R_{SO_2} to R_{NH_3} selectivity ratio of 7.2. The dynamic response % of Ni/SnO₂-rGO#1 sensor against 0.1 ppm SO₂ is ~4.9%, and 10 ppm NH₃ is ~0.4%. The R_{SO_2}/R_{NH_3} ratio increases to 13.8 (Fig. 4.16b), which suggests the potential improvement in the sulfur dioxide selectivity provided by the nickel element.

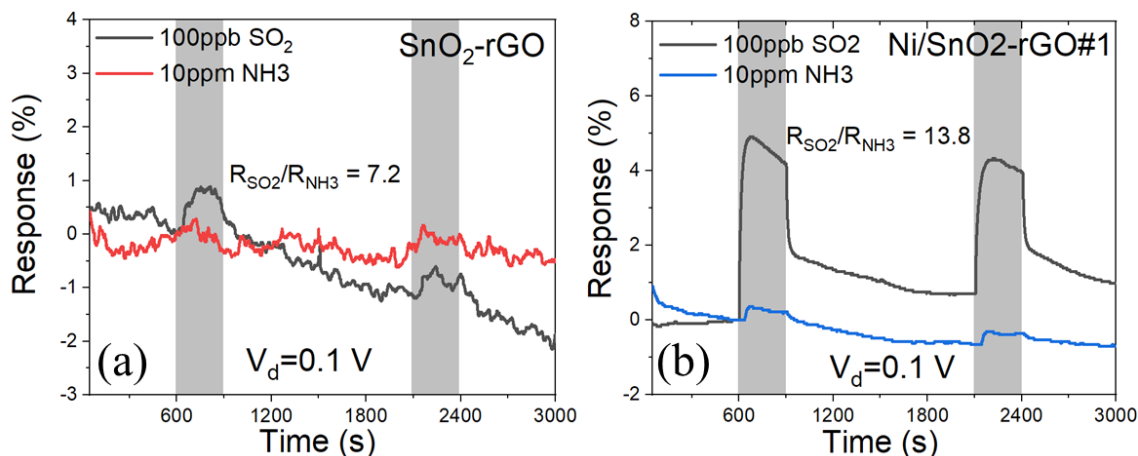


Figure 4.16 Sensing response against 0.1 ppm SO₂ and 10 ppm NH₃ of a) SnO₂-rGO, and b) Ni/SnO₂-rGO#1 sensors.

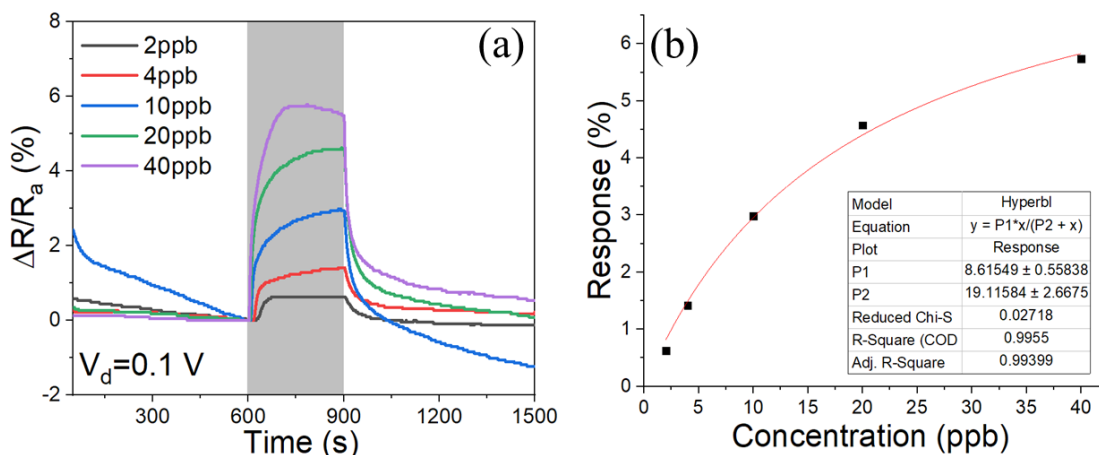


Figure 4.17 a) Dynamic response curves of Ni/SnO₂-rGO#1 sample to SO₂ with varying concentrations from 2 ppb to 40 ppb, b) Calibration curve of Ni/SnO₂-rGO#1 sensor.

The sulfur dioxide concentration-related dynamic response curves and the calibration curves are indicated in Figure 4.17 a-b. Figure 4.17b is well fitted by the Langmuir isotherm,

$$S = \frac{P_1 C}{C + P_2}$$

where P_1 is a constant equal to 8.6155 without unit, and P_2 is another constant equal to 19.116 having the same unit as the concentration (ppb). This can be explained by the relationship between the monolayer surface coverage and the gas partial pressure in the Langmuir isotherm.

4.3 Humidity Effect on the Graphene-based Gas Sensor

4.3.1 Introduction and motivation

The influence of environmental humidity on the sensing performance of chemiresistive gas sensors could not be ignored.⁷⁶ The water molecules may decrease the response to other analytes by consuming the adsorbed oxygen ions or occupying the adsorption sites on the metal oxide surface. The existing surface vacancies and remaining hydrophilic functional groups like the carboxylic groups could facilitate water molecule adsorption from the environment.¹⁴⁷ A vast number of graphene-based humidity sensors were proposed and investigated due to the properties mentioned above.¹⁴⁷⁻¹⁵¹

On the other hand, investigating the humidity effect on rGO-based and SnO₂-based sensor activity is quite necessary for the sulfur dioxide sensing platform presented here. The role of NiO additives in reducing the impact of humidity on the sensing properties of SnO₂-based gas sensors was reported by Barsan et al.¹⁵² The reduced and sluggish CO gas response due to the humidity effect was recovered after a small amount of NiO loading. DRIFTS results suggested that NiO acted as a vital water molecule absorber and protected the hierarchical SnO₂ from humidity poisoning.

A microheater was integrated into the SnO₂/rGO-based gas sensors to suppress the response to humidity.¹⁵³ It was revealed the sensitivity of SnO₂/rGO to humidity deteriorated at an elevated temperature of 54 °C. The decoration of the sieving layer (MOF etc.) also was demonstrated as an effective method to improve the immunity to humidity.⁶⁹

4.3.2 Material synthesis and sensor fabrication

The preparation of NiO/SnO₂-rGO ternary nanocomposites was similar as we mentioned before. 2/3/1 mmol of Ni(Ac)₂•4H₂O, 2/1/3 mmol of SnCl₂•2H₂O, and 1.5 g of urea were dissolved in 30

ml of DI water by vigorous stirring for 1 hour. The resulting compound was transferred into a Teflon-lined stainless-steel autoclave and maintained at 100 °C for 6 h. The products were collected by centrifugation and rinsed with DI water, then dried overnight. Then, the powder products were annealed in the tube furnace at 600 °C in air atmosphere for 5 h, separately. Finally, 100 mg of the final products (NiO/SnO₂) was dissolved in 10 ml DI water and 2 µl of sample was drop cast on the rGO sensor, which was fabricated through cysteamine (AET) functionalization. The three types of sensors with different Ni/Sn ratios were Ni1Sn1-rGO, Ni3Sn1-rGO, and Ni1Sn3-rGO.

4.3.3 Characterization and discussion

The XRD patterns of all three nanocomposites suggest the formation of cassiterite SnO₂. Only Ni3Sn1 indicated the typical peaks of NiO, as shown in Figure 4.18, due to the highest amount of nickel contained in the precursor.

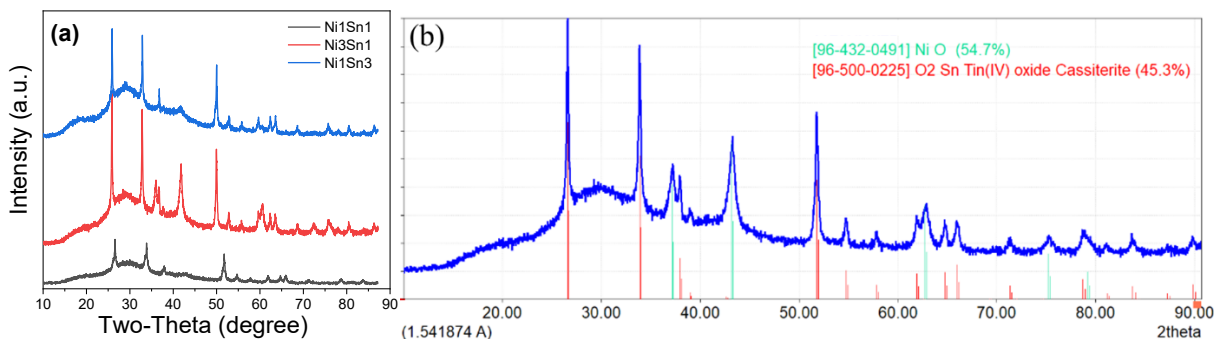


Figure 4.18 XRD patterns of a) Ni_xSn_y nanocomposites, b) Ni3Sn1 nanocomposites.

The atomic ratio of nickel to tin was revealed through XPS. The ratio of nickel to tin was 1:5, 1:1, and 1:15 relative to the 1:1, 3:1, and 1:3 in the precursors. The atomic ratio of nickel to tin in sample Ni3Sn1 was in good agreement with the XRD results.

We characterized the morphology and elemental distribution information through SEM and EDS after applying probe sonication. The SEM figures suggested the well-dispersed nanoparticles of the metal oxides. The EDS results indicated that the well-mixed nickel with tin elements within the nanocomposites. The quantified EDS elemental analysis results suggested the nickel to tin ratios highly agreed with the proportions in the precursors.

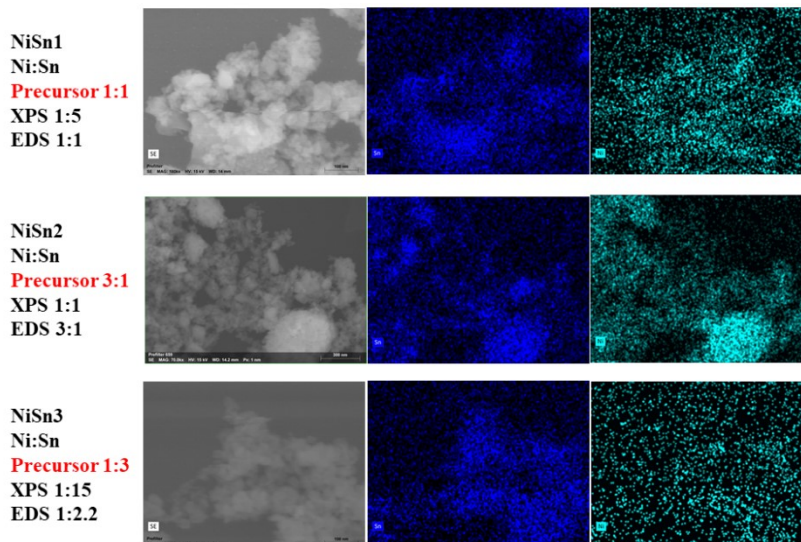


Figure 4.19 SEM and EDS images of the three NiO/SnO₂ nanocomposites.

4.3.4 Sensing results and discussion

First, we investigated the response of our current sensing materials against different levels of humid air. As shown in Figure 4.20a, the sensitivity of pure rGO against 40% relative humidity (RH), 60% RH, and 80% RH is 0.8%, 1.0%, and 1.3%, respectively, which is slightly higher than the sensitivity to 1ppm SO₂ (0.5%). The water molecules acted as electron donors and reduced the conductivity of rGO once attached to the surface.

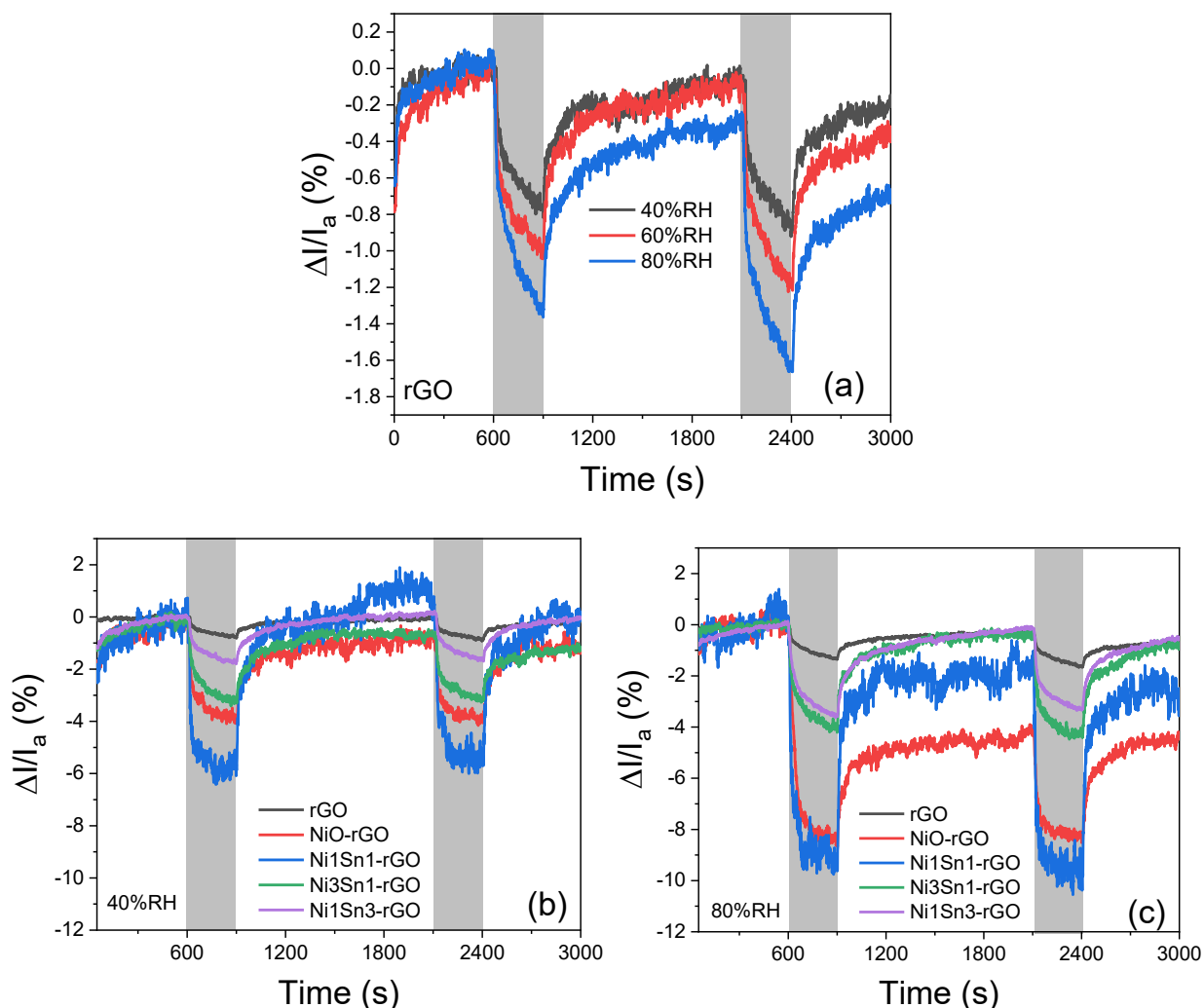


Figure 4.20 Dynamic response curves of a) rGO against 40% RH, 60% RH and 80% RH humid air, different sensing materials against b) 40% RH, c) 80% RH humid air.

Metal oxide dopants significantly enhanced the response of the sensors against humid air, as shown in Figure 4.20 b-c. Among five sensing materials, Ni1Sn1-rGO indicated the highest response against the humid air at 40% RH (Figure 4.20b) and 80% RH (Figure 4.20c). Ni1Sn3-rGO sensors with the least amount of nickel showed the lowest response among three metal oxide nanocomposites doped sensors.

Considering the common coexistence nature of sulfur dioxide and water molecules in the environment, the humidity-dependent SO_2 sensing experiments were conducted on our developed NiO/SnO₂-rGO sensors.

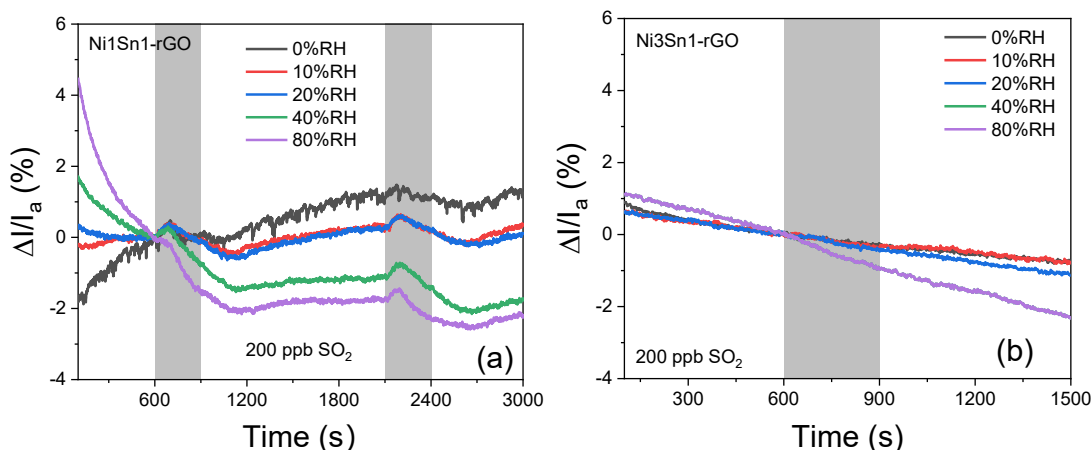


Figure 4.21 Humidity-dependent dynamic response curves of a) Ni1Sn1-rGO, b) Ni1Sn3-rGO.

The sensitivity of Ni1Sn1-rGO sensors against 200 ppb SO_2 is 0.5% under dry air conditions. Ni1Sn1-rGO sensors indicated opposite responses as the humidity level in the chamber increased. The conductivity of the sensor increased first as the SO_2 molecules were injected into the chamber. Water molecules demonstrated more competitive on binding to the sensing materials surface compared with SO_2 , which lead to the reduced conductivity after initial increasing.

The SO_2 sensing performance of Ni1Sn3-rGO sensors, which showed the least response against humid air, was investigated under different humidity levels. There were no significant responses observed within the sensing interval except the baseline drift due to the doping effect upon the adsorption of water molecules.

4.4 Conclusion

In summary, Ni-doped SnO₂-rGO ternary nanocomposites heterostructure was prepared. The Ni additives significantly improved the lower detection limit (ppb level) of the SnO₂-rGO platform. The Langmuir isotherm well fits the SO₂ concentration-dependent calibration curve. However, further research is needed to optimize the loading amount of the metal oxide nanocomposite and the ratio of nickel to tin in the nanocomposites. The humidity effect on the sensing performance was also investigated. The results suggested that current nanocomposites materials still suffer from the humidity effect. Metal oxide nanocomposites doping enhanced the SO₂ sensing but activated the adsorption of water molecules, which diminished the response to sulfur dioxide gas. An efficient water molecule sieving layer is in great demand on the sensor surface to block the water molecules and pass the dry sulfur dioxide to the sensor surface.

CHAPTER 5. TUNING THE GAS SENSING PERFORMANCE OF ORGANIC POLYMER-GO NANOCOMPOSITES SENSORS THROUGH DRAIN VOLTAGE MODULATION

5.1 Introduction

5.1.1 Organic chemiresistive gas sensor

Organic chemiresistive gas sensors made from small molecules and polymers have drawn tremendous attention due to their attractive properties such as ease of large-area fabrication, low cost and power consumption, superior selectivity, low detection limit, flexibility and biocompatibility.^{154, 155} Lu et al. fabricated a thin-film polysquaramide poly(4,4'-azodianlinesquaramide) (PADS)-based sensor to demonstrate the concept of dual hydrogen bonding for gas sensing.¹⁵⁵ The sensors showed extraordinary NH₃ (10ppt)/NO (20ppb) detection capability at room temperature. The dual hydrogen bonding between two amide H atoms in the conjugation chain and N atoms of NH₃/NO was explained as the key factor to high sensitivity and robustness. Conducting polymers (CPs) such as polyaniline (PANI), polythiophene (PTh) and polypyrrole (PPy)-based nanomaterials have been applied for gas sensing due to their low-temperature operation, short detection time and environmental stability. Used as a chemiresistor, polythiophene has been illustrated to provide good gas sensing properties to a range of gases and stable operation in an air ambient environment while combined with carbon-based nanomaterials.¹⁵⁶ Dr. Zang and his group selected Poly[3-(6-carboxyhexyl)thiophene-2,5-diyl] (P3CT) to functionalize carbon nanotubes. The carboxylic acid group in the polymer acts as a binder of organic amines via acid-base interaction. The P3CT-CNT sensors indicated good

sensitivity to methylphenethylamine (NMPEA) at the ppb level. The sensors could also distinguish NMPEA from two other amine compounds, various volatile organic compounds (VOCs), and water vapor. A highly sensitive and selective ethanol sensor based on PTh/graphene nanocomposite with lower detection limit down to 400 ppm at room temperature was demonstrated by Dr. Mohammad et al. The significantly improved conductivity and sensitivity was explained as the charge hopping from PTh to graphene due to its extraordinary charge mobility as well as the π - π interaction between PTh and graphene nanosheets that provide abrupt movability of polarons along with the π -conjugated system of graphene nanosheets.¹⁵⁷ Dr. Lu et al. fabricated a flexible humidity sensor based on a Pt/PTh/RGO ternary nanocomposite film. This flexible humidity sensor exhibited good sensitivity and acceptable linearity between the logarithmic impedance ($\log Z$) and RH within the range of 10% to 90% RH.¹⁵⁸ Dr. Li et al. successfully synthesized the RGO-PTh hybrids through in situ chemical oxidation polymerization. The sensors based on the hybrids indicated enhanced NO₂ sensing performance at room temperature ascribe to the complementary and synergistic effect between rGO and PTh.¹⁵⁹

However, there are limited reports about composites based on polythiophene and graphene or its derivatives for gas sensing. Most of the reports required a complex synthesis method for fabricating the polymer-based composites. A facile method for composite synthesis such as spin-coating would facilitate the fabrication. Furthermore, functionalized conducting polymers with specific functional groups such as carboxylic groups could improve gas sensing properties. Katz and his group demonstrated a carboxylated thiophene polymer-based chemiresistive device in a field-effect transistor (FET) configuration with remarkably high responses to nitrogen dioxide (NO₂) and ammonia (NH₃).¹⁶⁰ The enhanced NO₂ sensitivity was attributed to the incorporation of carboxylic acid groups (COOH) in the p-type alkylthiophene polymer. The remote gate detection

platform was utilized to explore the sensing mechanism. Proton conduction contributes significantly to the high sensitivity of the carboxylic acid to NO₂.

5.1.2 Signal processing for gas sensing application

To recognize gas with enhanced selectivity and specificity on a single sensor is the long-term bottleneck of traditional chemiresistive gas sensors due to the limited sensing parameters, which caused insufficient degrees of freedoms for pattern recognition. The assembly of sensors to be cross-reactive sensor arrays has been demonstrated as an effective route to achieving high selectivity.¹⁶¹ The multivariate responses obtained by chemical sensor arrays require signal and data processing to carry out the fundamental tasks of odor identification (classification), concentration estimation (regression), and grouping of similar odors (clustering).¹⁶²

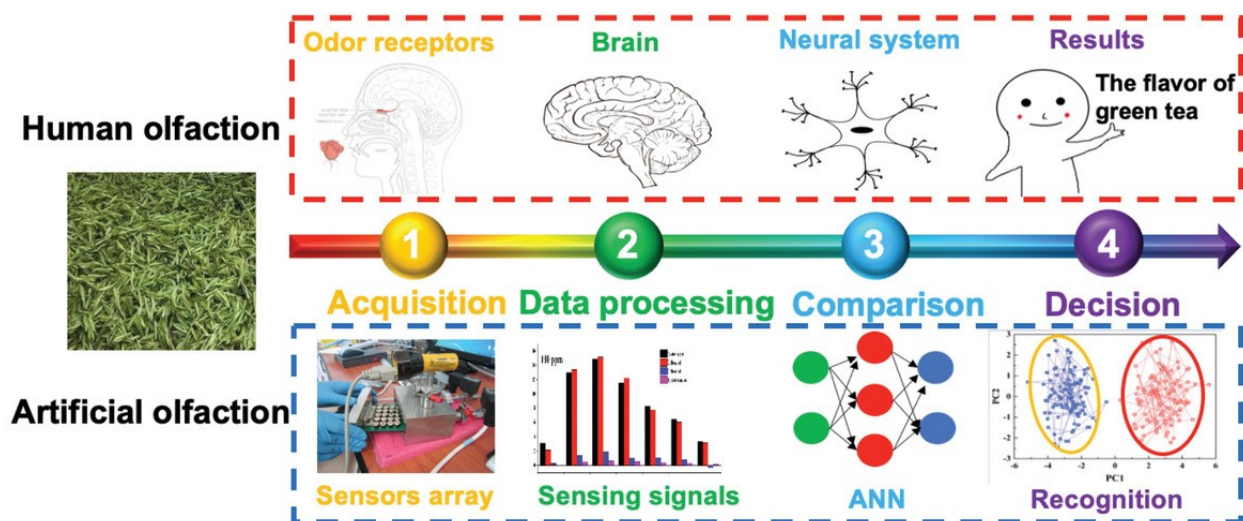


Figure 5.1 Schematic diagram of the working principle of the human and artificial olfaction.¹⁶¹ Copyright 2018 WILEY-VCH.

The artificial devices that combine arrays of chemical sensors with pattern recognition techniques commonly termed “electronic nose” (e-nose), have been explored for distinguishing different gaseous components, as shown in Figure 5.1. The typical process of signal processing for gas sensing application is shown in Figure 5.2. Feature selection and extraction is a dimensionality

reduction approach extracting a certain number of features from the large raw sensing data for further analysis. The pattern recognition and classification techniques play an important role in the e-nose system for distinguishing different types of gases based on the extracted features. Conventionally, the statistical methods can work alone to deal with the sensing data and are still a popular way for pattern recognition. Recently, Artificial Intelligence (AI) techniques have successfully solved many problems in the fields of pattern recognition, similar to with the function of human brain in the olfaction.

Principle component analysis (PCA) finds projection weights for sensor response data that maximize the total response variance in principal components. A xylene isomer vapor sensor was developed based on an ambipolar polymer poly(diketopyrrolopyrrole-terthiophene) (PDPPHD-T3).¹⁶³ The sensing data from a single PDPPHD-T3 device was treated with a statistical signal processing method. Each of the structurally similar xylene isomers was clearly distinguished through principal component analysis.

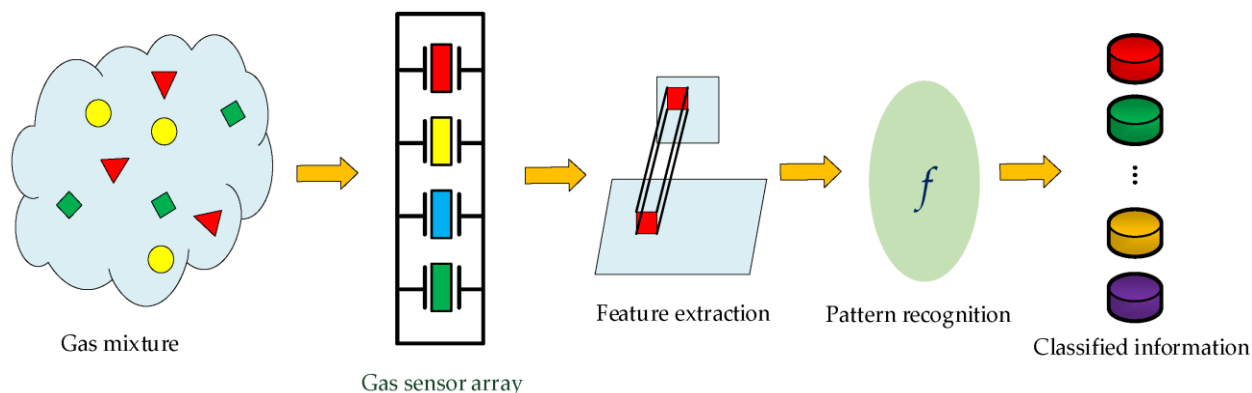


Figure 5.2 Schematic of the gas sensor signal processing.

Li et al. fabricated a chemiresistive graphene chemical vapor sensor with an unmodified surface. The capability of the sensor to distinguish different compounds was evaluated by PCA, which exhibited impressive separation between different vapors.¹⁶⁴ Kim and his group developed porous $\text{SnO}_2/\text{CoO}_x$ heterogenous nanosheets as highly sensitive and selective HCHO -sensing materials.

PCA was conducted based on the response values. The seven interfering gases were explicitly classified with HCHO gas.¹⁶⁵

5.2 Experimental Methods and Results

5.2.1 Material preparation and sensor fabrication

PT-COOH powder (Rieke Metals) and GO (Matexcel) were directly used as purchased. First, PT-COOH powder was dissolved in DMF with a 10 mg/ml concentration and placed on a hot plate at 60 °C overnight before increasing the temperature to 120 °C for 20 minutes. The solution was then filtered using a hydrophilic polytetrafluoroethylene (PTFE) 0.45 µm syringe membrane. The PT-COOH solution was spin-coated on the clean wafers with fabricated electrodes at 1600 rpm for 320 seconds. The wafers were then baked at 60 °C overnight in a vacuum oven to outgas any residual solvent present. Figure 5.3a illustrates the structure of the pure PT-COOH sensors. The carboxylic acid groups (COOH) were incorporated in a p-type alkylthiophene polymer, as shown in Figure 5.3b.

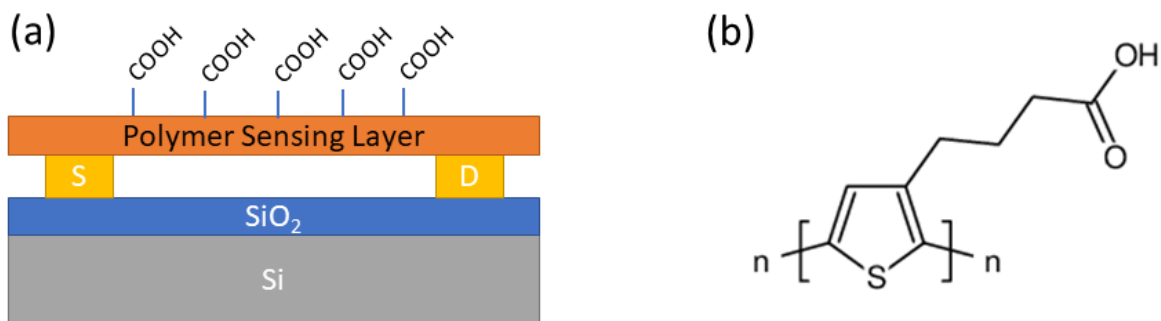


Figure 5.3 a) Schematic architecture of the pure PT-COOH gas sensing device, b) Molecular structures of PT-COOH.

PT-COOH-GO sensors were fabricated based on pure PT-COOH devices. GO was dissolved in DI water with a concentration of 100 mg/L and sonicated for 15 minutes. Then, the GO solution

was spin-coated on the PT-COOH sensors directly. The fabricated sensors were baked at 80 °C for 10 minutes.

5.2.2 Material characterization

The morphology and surface condition were investigated through SEM (Hitachi S4800) and atomic force microscopy (AFM) (Agilent Technologies). Figure 5.4a shows the surface morphology of the pure PT-COOH device. Some large, aggregated islands could be found with the size in the range of 1~3 μm which agrees well with the SEM images (Figure 5.4bc). The thickness of these islands is around 40 nm.

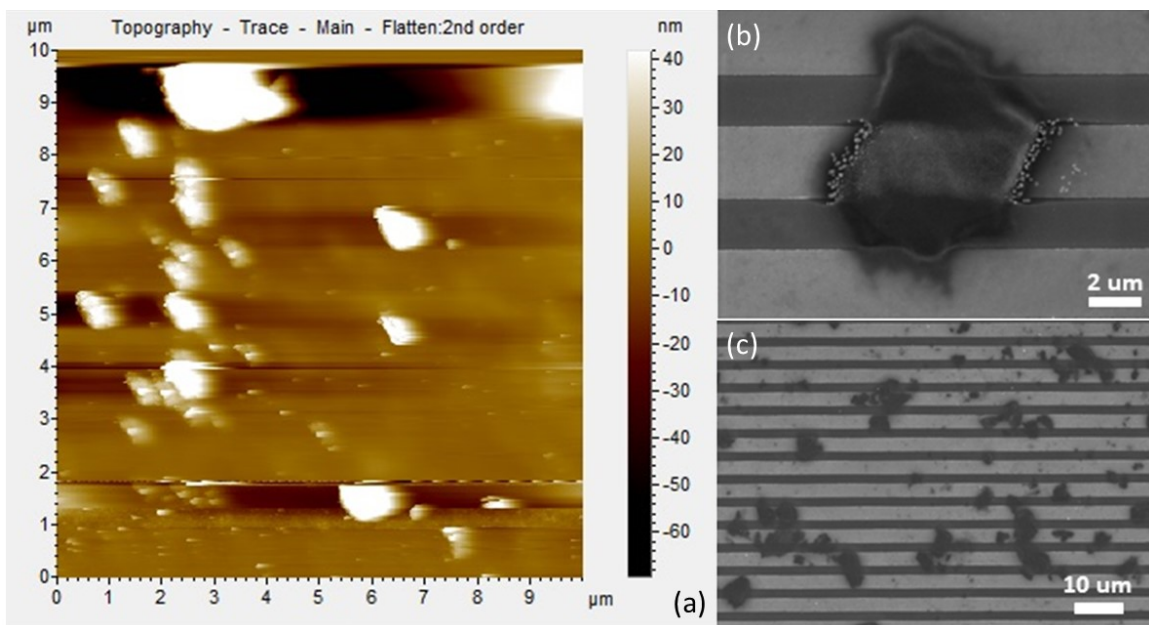


Figure 5.4 a) AFM, b-c) SEM images of the PT-COOH devices.

The SEM images of the PT-COOH-GO devices suggest the formation of a continuous film coated on the electrode fingers. This could be correlated to the spin-coated high concentration of graphene oxide nanosheets.

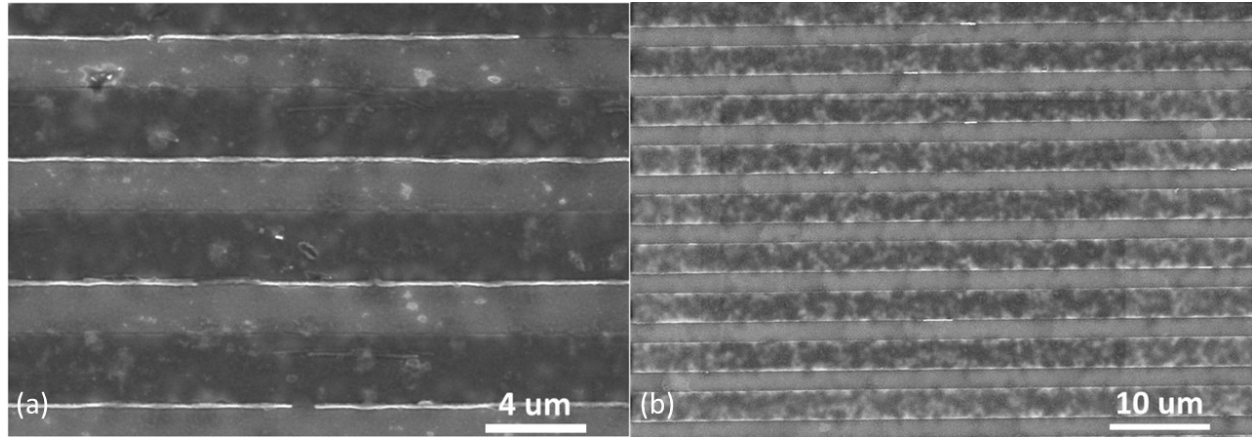


Figure 5.5 SEM images of PT-COOH-GO devices in different scales.

5.2.3 Gas sensing test

A typical gas sensing test cycle had three steps. The first step was the introduction of clean carrier gas into the sensing chamber and was used to obtain a baseline measurement. The typical preset time for this step was 10 minutes or until the baseline became stable. The second step was adding various target gases being injected through the flowmeter into the test chamber with the same flow rate as the first step to generate the sensing signal. The exposure time for the target gas was 1 or 5 minutes. Finally, in the third step involved the target gas was turned off and a 100% composition of the carrier gas was introduced again for sensor recovery. The third step lasted for at least 10 minutes. The compressed air was selected as the carrier gas.

It was found that the PTh-based sensors exhibited the p-type semiconductor behavior during the gas sensing experiment.¹⁵⁹ The drain current of PT-COOH sensors increased upon exposure to oxidizing gas of NO₂,¹⁶⁰ decreased upon exposure to reducing gas of NH₃. Therefore, the response

(R) for oxidizing gases NO₂, SO₂ is defined as $R_{(NO_2, SO_2)} = \frac{(I_{gas} - I_{air})}{I_{air}} \times 100\%$, whereas that for

reducing gases is defined as $R_{(NH_3, CO)} = \frac{(R_{gas} - R_{air})}{R_{air}} \times 100\%$.

5.3 Gas Sensing Results and Discussion

5.3.1 PT-COOH gas sensor

Figure 5.6a displays the output characteristics of pure PT-COOH devices. The conductivity increased along with the increase of the negative gate voltage applied to the bottom of the devices, which exhibited the typical p-type channel behavior. The transfer curve (Figure 5.6b) under -4 V drain voltage also supports the p-type behavior of pure PT-COOH devices.

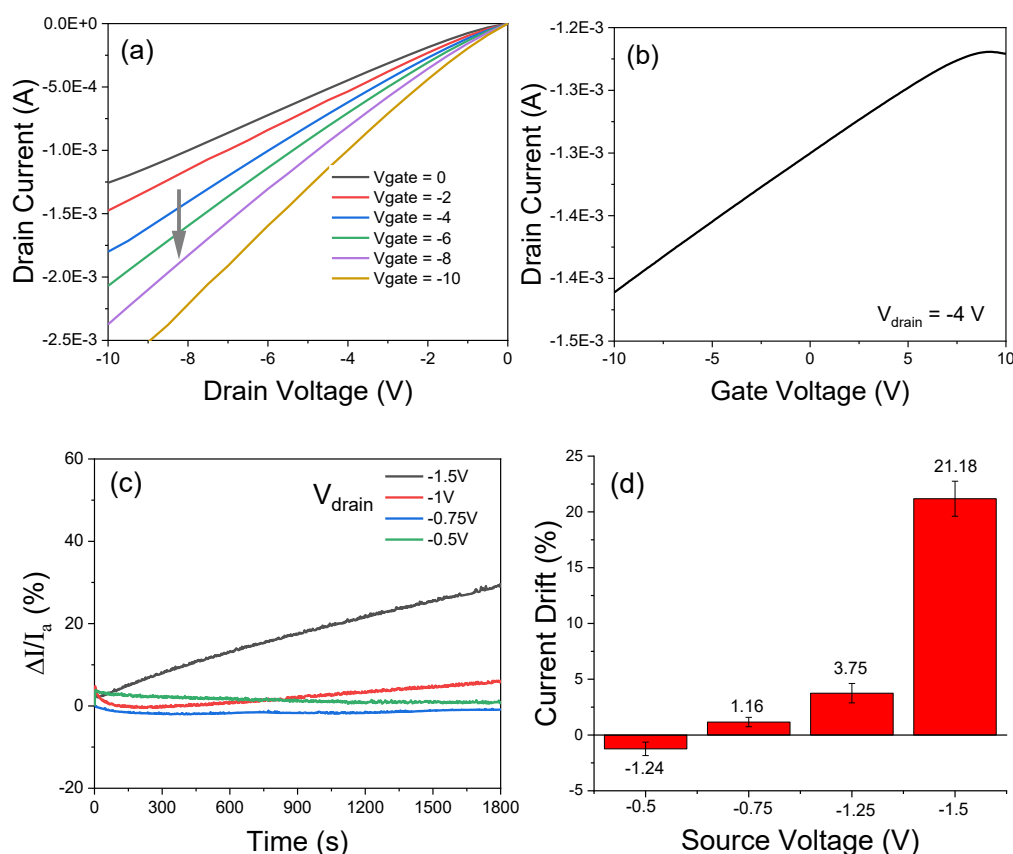


Figure 5.6 Pure PT-COOH devices a) gate voltage-dependent output curves, b) transfer curve under -4 V drain voltage, c) drain voltage-dependent current drift curves, d) statistic bar chart of current drift.

Drain voltage-dependent current drift is one of the typical phenomena we observed from the PT-COOH based devices. We tested the percentage of current drift in 30 minutes under different drain voltages applied between the source and drain electrodes. The average current drift values of 10

devices related to different drain voltages are shown in Figure 5.6d. The higher drain voltage induced more significant current drift in the devices. This may be explained as the charging effect of the conducting polymers.

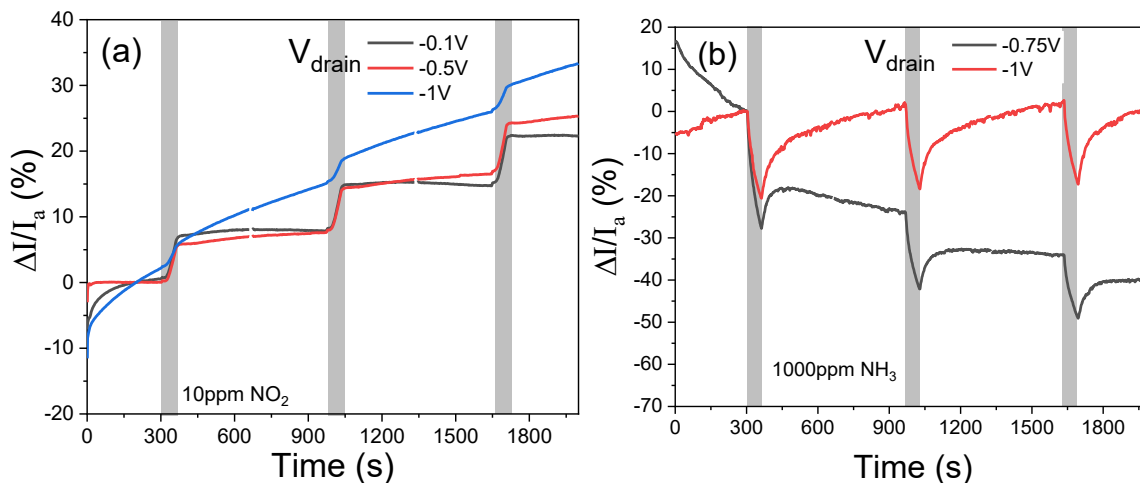


Figure 5.7 Sensing properties of pure PT-COOH against 10 ppm NO_2 (a) and 1,000 ppm NH_3 (b).

Then we investigated the sensing properties of pure PT-COOH sensors. Since -0.5 V drain voltage provided the most stable current baseline, the PT-COOH was tested against 10 ppm NO_2 under -0.5 V drain voltage first. The current increased around 5.5% after exposure to NO_2 for 60 seconds. However, no recovery was observed after the sensing interval. After that, we applied -1 V drain voltage and tested the sensing performance. The current baseline kept upward drifting with minor sensitivity exhibited within the sensing interval, which is consistent with the current drift curves. Then, the drain voltage was decreased to -0.1 V. We could find the direction of the current drift switched downward compared to -0.5 V, but still cannot fully compensate for the increase in the sensing interval.

The sensing performance to NH_3 was also investigated. With -0.75 V drain voltage applied, PT-COOH sensors exhibited partial recovery from the decreased current induced by reducing gas NH_3 .

The consistent and stable multi-cycle NH_3 sensing was achieved with -1 V drain voltage. The increasing drain voltage-induced current drift fully compensated the NH_3 induced current decrease. This interesting sensing performance demonstrated the potential of tuning gas sensing through drain voltage modulation on the PT-COOH based sensors. Typically, many organic field-effect transistors suffer from current baseline drifts upon gate voltage application which could be attributed to a shift in the threshold voltage.¹⁶⁶ However, the baseline drift phenomenon we observed was more drain voltage-dependent than gate voltage-dependent.

5.3.2 PT-COOH-GO gas sensor

The output characteristics of PT-COOH-GO devices are shown in Figure 5.8a. PT-COOH-GO also exhibited typical p-type semiconductor behavior (agree with transfer curves Figure 5.8b) with much higher conductivity than pure PT-COOH. The significant increase in conductivity of PT-COOH-GO nanocomposites may be attributed to several reasons: (1) forming an efficient network in PT-COOH aggregated islands connected by continuous graphene oxide nanosheets film. (2) Higher hole mobility of GO nanosheets in comparison to PT-COOH leading to the hopping of charge carriers from PT-COOH to GO through π - π interaction between PT-COOH and GO.¹⁵⁷

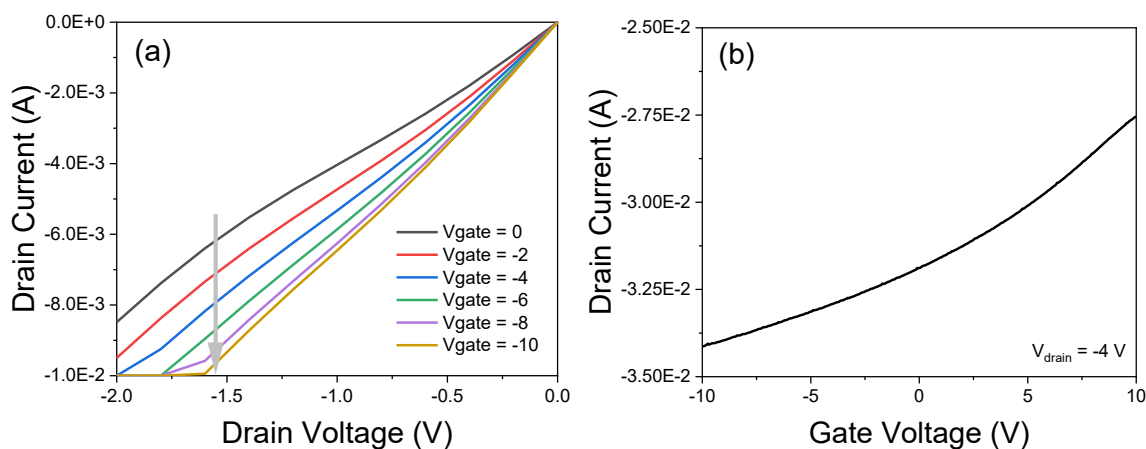


Figure 5.8 PT-COOH-GO a) output and b) transfer curves.

The drain voltage-dependent current drift property of PT-COOH-GO nanocomposites was also investigated, as shown in Figure 5.9. The current drifted downward when -0.01 V and -0.1 V drain voltage were applied. The drift direction switched when the drain voltage reached -0.5 V. After further increasing the drain voltage to -2 V, the current drift curve indicated the most significant slope from the beginning and then reached the saturation region after 15 minutes. Noteworthy, the current drift became milder once the drain voltage further increased to -4 V and -6 V. The oversaturation situation seems achieved under higher drain voltages. The drain voltage-dependent current drift might be related to the charging effect at the source-drain electrodes/polymer interface, similar to the gating effect from the gate electrode for FET devices.^{167, 168}

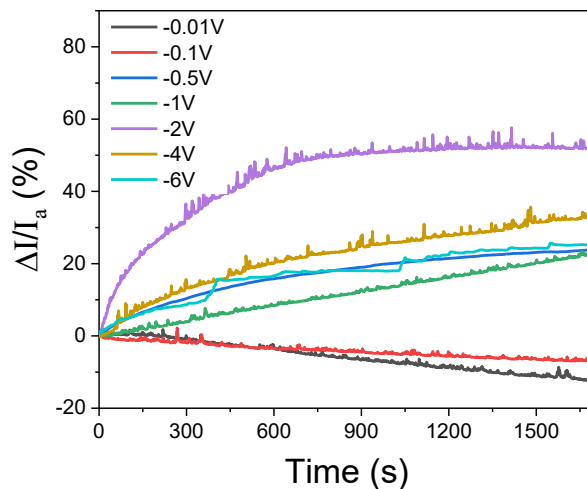


Figure 5.9 Drain voltage-dependent baseline drift curves of PT-COOH-GO.

We conducted the gas sensing test against NO₂, NH₃, and SO₂ with -6 V drain voltage applied to confirm the proposed oversaturation situation under a high drain voltage. The sensitivity to 0.5 ppm, 1 ppm, and 2 ppm NO₂ is 7.5%, 23%, and 45.9%, respectively. PT-COOH-GO sensors exhibited enhanced sensing performance compared to pure PT-COOH sensors with higher

sensitivity and full recovery performance. The full recovery performance is demonstrated in NO₂ sensing and in NH₃ and SO₂, which revealed the modulation effect from the drain voltage.

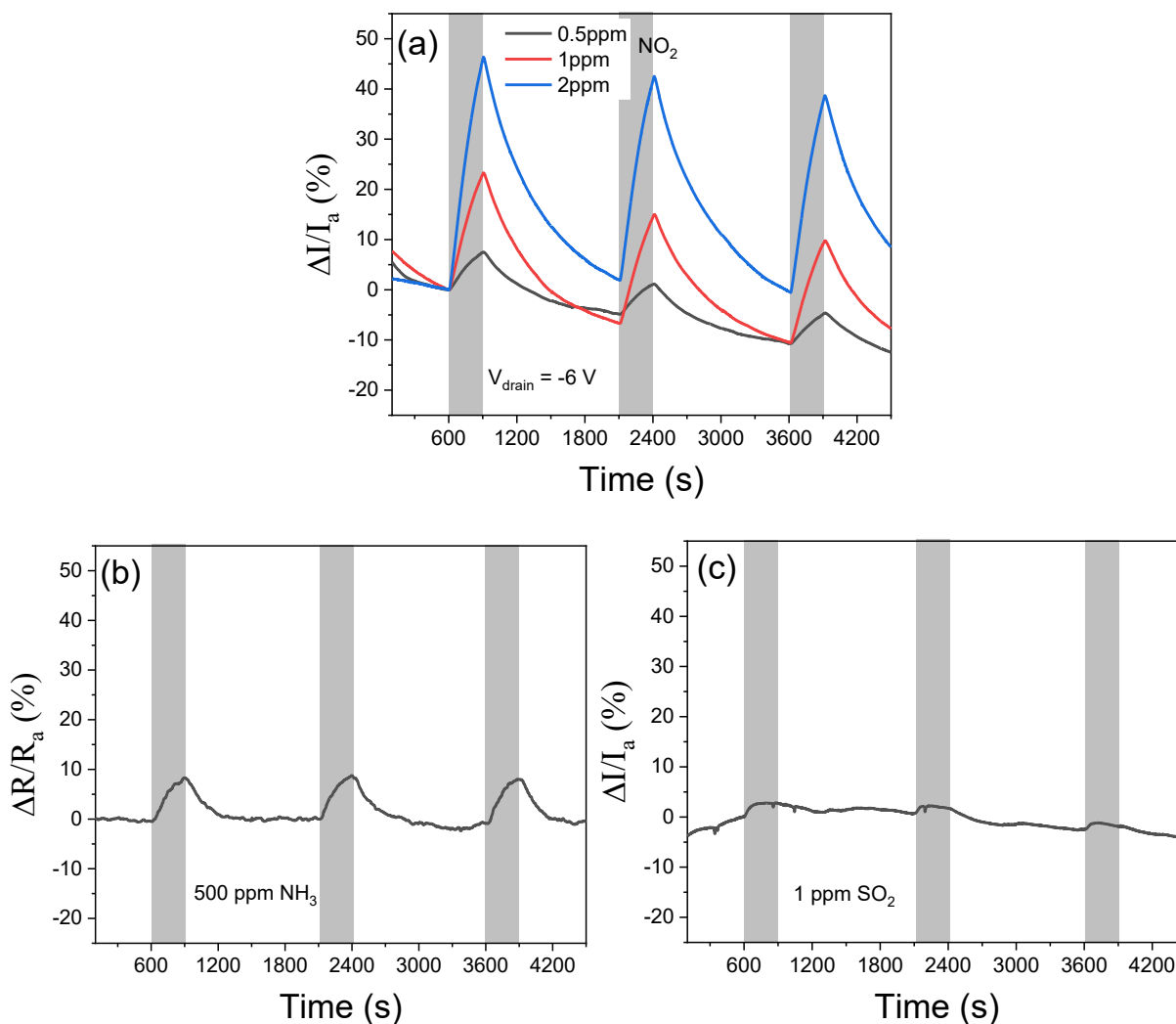


Figure 5.10 Sensing performance of PT-COOH-GO under -6 V drain voltage a) varying concentrations of NO₂, b) 500 ppm NH₃, c) 1 ppm SO₂.

The long-term sensing experiment was conducted to illustrate the stability of the sensors under different situations and analyte gases. Figure 5.11a indicates the slow but unsaturated current drift under -0.01 V drain voltage within 50 sensing cycles against 1ppm CO. The baseline current under -0.5 V drain voltage exhibited opposite drift direction with exposure to NO₂ (Figure 5.11c) and NH₃ (Figure 5.11b). This could be ascribed to the doping effect from the oxidizing gas NO₂ and

reducing gas NH_3 molecules. The current baseline of these two experiments all took around 12,000 seconds to become stable.

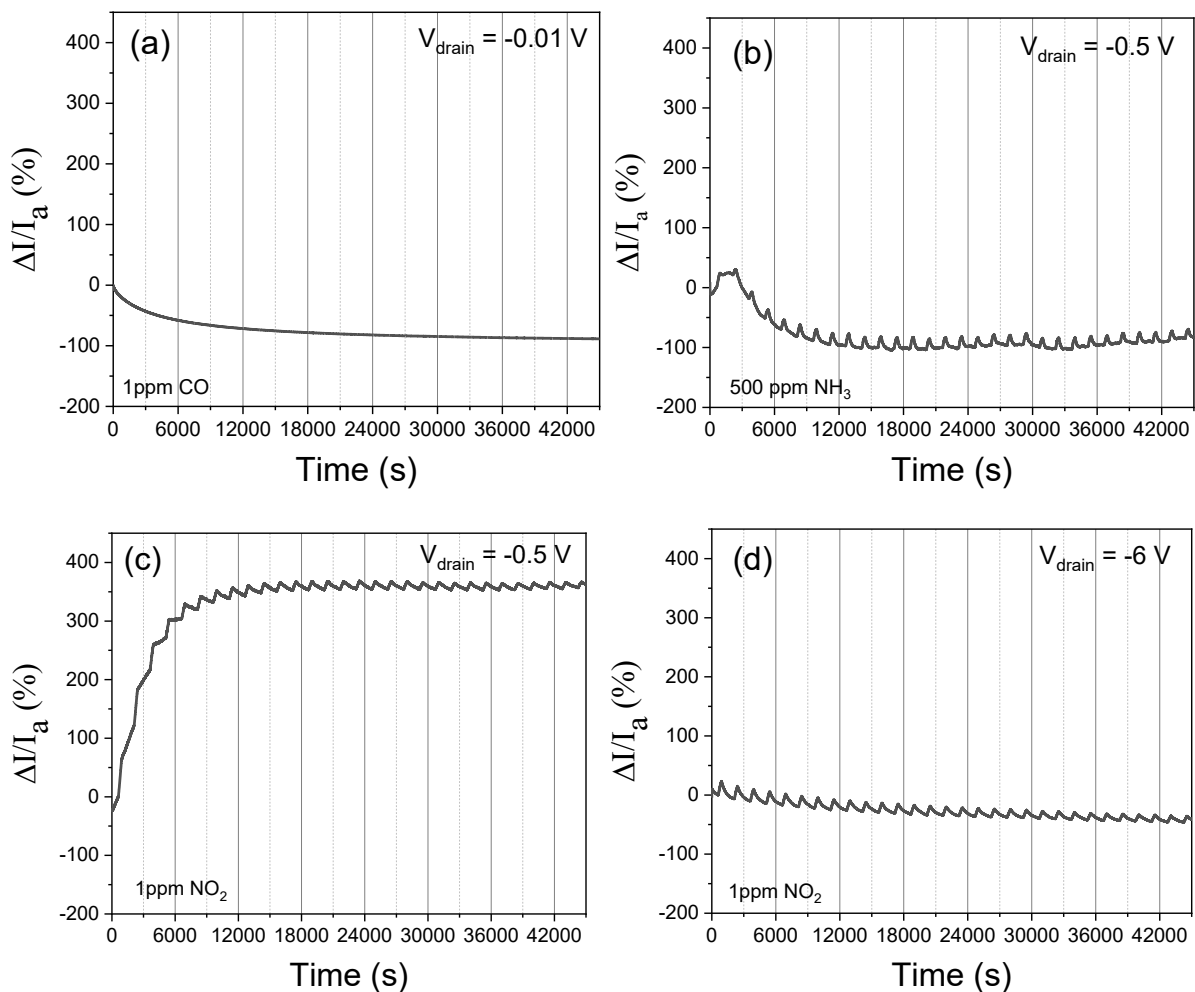


Figure 5.11 Drain voltage-dependent 50 cycles response curves a) 1 ppm CO under -0.01 V, b) 500 ppm NH_3 under -0.5 V, c) 1 ppm NO_2 under -0.5 V, d) 1 ppm NO_2 under -6 V.

Figure 5.11d shows the optimal sensing performance among all the test conditions. The PT-COOH-GO sensors indicated a stable and consistent sensing response against 1 ppm NO_2 for 50 cycles.

Typically, the sensing mechanism of the pure PT-COOH and PT-COOH-GO nanocomposites could be described as a simple adsorption-desorption mechanism. In the presence of analytes, the

gas molecules adsorbed on the sensing materials and induced the charge carrier transfer within the materials, which led to the change in the conductance.¹⁵⁷

The enhanced NO₂ sensing performance of the PT-COOH-GO nanocomposites could be ascribed to several plausible reasons: (1) larger sensing area offered by the GO film instead of isolated PT-COOH islands, (2) The π - π interaction between PT-COOH and GO causes a charge carrier transfer rate increase during the process of NO₂ sensing. (3) The required energy of electrons to delocalize along the PTh chain could decrease, which allows NO₂ to capture electrons from nanocomposites more easily.¹⁵⁹ To identify the dominant sensing mechanism, more characterization or simulation need to be conducted such as BET measurements and, DFT calculations.

5.3.3 Statistical sensing signal analysis

We randomly picked 10 NH₃ sensing cycles, 7 NO₂ sensing cycles, and 2 SO₂ sensing cycles for signal processing. The features were directly calculated from the sensing cycles. We selected the maximum of six features for pattern recognition: sensitivity, initial response slope within 100 seconds, end response slope within 100 seconds, initial recovery slope within 100 seconds, initial response slope within 20 seconds, and initial recovery slope within 20 seconds. To evaluate the importance of each feature, we conducted three pattern recognition processes with only first four features selected (Figure 5.12a), five features selected (Figure 5.12b), and all six features selected (Figure 5.12c).

With the four features selected, the input data was a 4×18 matrix (four selected features and a total of eighteen sensing cycles). This 4×18 matrix was performed with principal component analysis (PCA) using the Originlab software. A similar process was conducted for the rest two treatments. The results of the statistical signal processing are illustrated in Figure 5.12. The first

five features exhibited good gas discrimination capability as the clear grouped separation among these three analyte gases. With the inclusion of the last feature, initial recovery slope within 20 seconds, the data points in Figure 5.12c seem more scattered between different gases and within the same type of gas, which indicated poor discrimination result.

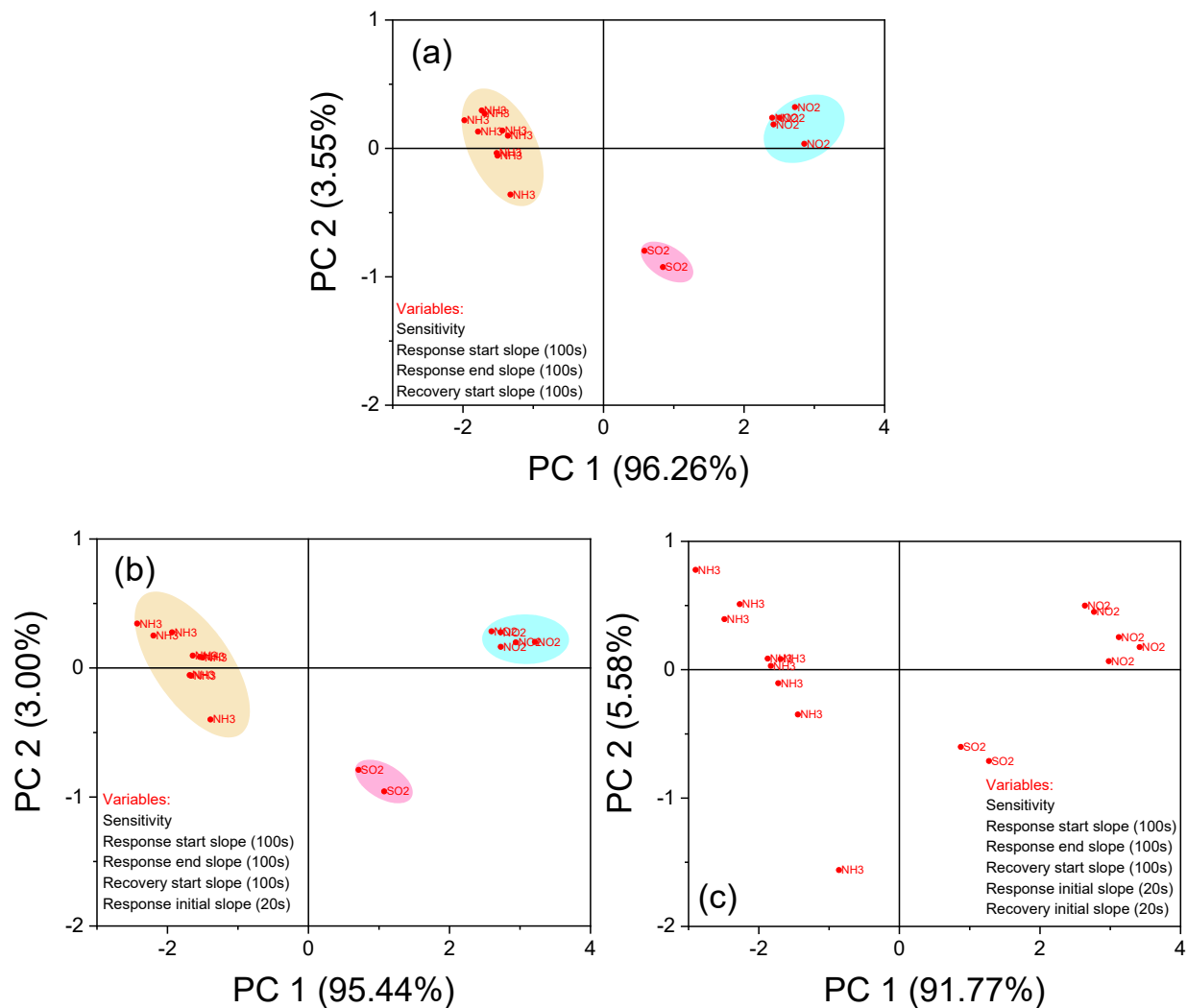


Figure 5.12 PCA plots showing PT-COOH-GO nanocomposites with PC1 and PC2 using response of 3 gases (NH₃: 500ppm, NO₂: 1ppm, SO₂: 1ppm) as input data for feature calculation, a) first four features, b) first five features, and c) all six features.

5.4 Conclusion

In summary, the PT-COOH and PT-COOH-GO sensors were successfully fabricated. The gas sensing properties were investigated toward NO₂, NH₃, SO₂, and CO. The PT-COOH based sensors exhibited tunable sensing performance, especially in recovery through drain voltage modulation. PT-COOH-GO sensors indicated enhanced NO₂ sensing performance with good sensitivity, recovery, and stable response. The drain voltage-dependent current drift might be related to the charging effect at the source-drain electrodes/polymer interface, similar to the gating effect from the gate electrode for FET devices. The enhanced NO₂ sensing performance of the PT-COOH-GO nanocomposites could be ascribed to several plausible reasons: (1) larger sensing area offered by the GO film instead of isolated PT-COOH islands, (2) The π - π interaction between PT-COOH and GO causes a charge carrier transfer rate increase during the process of NO₂ sensing, (3) The required energy of electrons to delocalize along the PTh chain could decrease, which allows NO₂ to capture electrons from nanocomposites more easily. To identify the dominant sensing mechanism, more characterization or simulation need to be conducted such as BET measurements and, DFT calculations. The statistical signal analysis was conducted to obtain proof-of-concept results for gas discrimination through signal processing.

CHAPTER 6. SUMMARY AND FUTURE WORK

6.1 Summary

Owing to the strong chemical or electronic interaction between closely packed interfaces, heterostructures show superior and tunable sensing performances compared with single structures. However, the sensing mechanisms of heterostructure-based gas sensors remain unclear. In this dissertation research, we investigated the sensing mechanisms through several in-situ characterization methods and analysis under real operating conditions, which provided more comprehensive understanding on the mechanisms of the heterostructure gas sensors.

Composite heterostructure materials can be easily attained through mechanically mixing various components. We have first fabricated NiO-WO₃ multi-nanowires heterostructures via a facile, sonication-based solution mixing method. The resulting heterojunction effect was maximally observed for W3N1 (75 mol% WO₃-25 mol% NiO) and confirmed by observation of the increase in resistance due to the formation of diode-like p-n junctions at the WO₃-NiO interface. The H₂S sensing performances of different heterostructures with various component ratios were revealed through the combination of DC and impedance measurements and in situ XRD characterization. The excellent sensing performance for W3N1 is attributed to the p-n junction effect, sulfurization by H₂S (formation of WS_{2-x} and NiS_{1-x}), and the ideal ratio of the NiO component in the composite. The formation of reactive semi-metallic products due to sulfurization was confirmed by XRD analyses for H₂S adsorbed on the sensor surface. Further investigations from in-situ impedance measurements and RC equivalent circuit analyses during gas sensing were performed to evaluate the effects of the grain-grain boundary and the p-n junction on sensing performance. It was found that for the pure WO₃ and W3N1 samples, these contributing effects are in the same direction,

resulting in a cooperating and highly sensitive performance, whereas other samples (W1N1, W1N3, and N) exhibited competitive influences, resulting in a lower sensitivity.

Because rGO-based gas sensors offer room-temperature sensing properties, we have synthesized various rGO-based heterostructures towards different gas analytes. We investigated the noble metal-metal oxide-rGO models and fabricated the Au-SnO₂/rGO ternary nanohybrids through a combination of hydrothermal and sputter coating methods. The room-temperature sensing performances toward H₂ were obviously enhanced after Au nanoparticle deposition. The sputtered Au nanoparticles enhanced both sensitivity and recovery of the SnO₂-rGO template. Such an enhancement was attributed to the increased surface area and the oxygen spillover effect of loaded Au nanoparticles. The catalytic effect of Au nanoparticles for hydrogen adsorption and desorption was then revealed through the temperature-dependent sensing test and Arrhenius analysis. A better balance between sensitivity and recovery can be further achieved in the future by tuning the deposition conditions of Au nanoparticles.

We also fabricated Ni-doped SnO₂-rGO ternary nanohybrids for SO₂ sensing. The Ni additives significantly improved the lower detection limit (down to the ppb level) of the SnO₂-rGO platform. The SO₂ concentration calibration curve is well fitted by the Langmuir isotherm. The humidity effect on the sensing performance was also investigated. The results suggested that current nanocomposites materials still suffer from the humidity effect. Metal oxide nanocomposites doping enhanced the SO₂ sensing and activated the adsorption of water molecules, which diminished the response to sulfur dioxide gas.

Finally, the sensing performance of an organic polymer-GO nanocomposite was investigated. We fabricated PT-COOH and PT-COOH-GO sensors and investigated the gas sensing proprieties. The gas sensing properties were investigated toward NO₂, NH₃, SO₂, and CO at room temperature. The

PT-COOH based sensors exhibited tunable sensing performance through drain voltage modulation. PT-COOH-GO sensors indicated enhanced NO₂ sensing performance with good sensitivity, recovery, and stable response. The drain voltage-dependent current drift may be related to the modulation of the carrier injection barrier height at the electrode/polymer interface. The enhanced NO₂ sensing performance of the PT-COOH-GO nanocomposites could be ascribed to several plausible reasons: (1) larger sensing area offered by the GO film instead of isolated PT-COOH islands, (2) The π - π interaction between PT-COOH and GO causes a charge carrier transfer rate increase during the process of NO₂ sensing.,(3) The required energy of electrons to delocalize along the PTh chain could decrease, which allows NO₂ to capture electrons from nanocomposites more easily. To identify the dominant sensing mechanism, more characterization or simulation need to be conducted, such as BET measurement and DFT calculations. The statistical signal analysis was conducted to obtain proof-of-concept results for gas discrimination through signal processing.

6.2 Future work

Humidity is an essential factor that could significantly influence the sensing performance of chemiresistive gas sensors, especially at room temperature. The water molecules may decrease the response to target analytes by consuming the adsorbed oxygen ions or occupying the adsorption sites on the metal oxide surface. The existing surface vacancies and remaining hydrophilic functional groups like the carboxylic groups could facilitate water molecule adsorption from the environment. The results of the humidity-dependent gas sensing experiments indicated non-ideal humidity-resist properties of NiO/SnO₂-rGO sensors. Future research is needed to optimize the loading amount of the nanocomposites and the ratio of tin to nickel for SO₂ sensing. There is also

an opportunity to investigate the water molecules' sieving layer to remove the humidity effect on sensor performance.

Organic material is another widely explored resistive gas sensing material. Typically, organic field-effect transistors suffer from current baseline drifts upon gate voltage application, which could be attributed to the shift in the threshold voltage. However, the baseline drift phenomenon observed in this study was more drain voltage-dependent than gate voltage-dependent. The drain voltage-dependent current drift might be related to the modulation of the carrier injection barrier height. Further research is warranted to change the dimension of the conducting channel or the electrode materials to understand the influences of the barrier height on the current drift modulation. The PT-COOH-GO gas sensor has indicated promising responses to NO₂ at room temperature through drain voltage modulation. The enhanced NO₂ sensing performance of the PT-COOH-GO nanocomposites could be ascribed to several plausible reasons: (1) larger sensing area offered by the GO film instead of isolated PT-COOH islands, (2) The π - π interaction between PT-COOH and GO causes a charge carrier transfer rate increase during the process of NO₂ sensing, (3) The required energy of electrons to delocalize along the PTh chain could decrease, which allows NO₂ to capture electrons from nanocomposites more easily. More characterization or simulation needs to be conducted to identify the dominant sensing mechanism through BET characterization and DFT calculations. Different fabrication processes and conditions such as PT-COOH on top of GO and different GO concentrations for spin coating can be explored.

To recognize gas with enhanced selectivity and specificity on a single sensor or even sensor arrays is the long-term bottleneck of traditional chemiresistive gas sensors due to the limited sensing parameters, which caused insufficient degrees of freedom for pattern recognition. This research has demonstrated the proof-of-concept results in the statistical signal processing for gas

discrimination. More work is needed to improve the feature extraction through wavelet analysis and pattern recognition of the sensor data in the future. Furthermore, exciting opportunities exist in the exploration of the neural network model to demonstrate gas discrimination through machine learning.

The drastic developments toward in situ and operando characterization techniques were remarkable in the last decades. Up to date, various spectroscopy techniques were modified for the operando study of chemical information related to gas sensing. More research is needed to explore in situ and operando characterization methods such as in situ TEM and FTIR with a proper gas chamber and to understand heterostructure's sensing mechanisms more comprehensively.

REFERENCES

1. Yang, S.; Jiang, C.; Wei, S.-h., Gas sensing in 2D materials. *Applied Physics Reviews* **2017**, *4* (2).
2. FRENSLEY, W. R., Heterostructure and Quantum Well Physics. In *Heterostructures and Quantum Devices*, Academic Press Inc.: 1994.
3. KOLASINSKI, K. W., *Surface Science Foundations of Catalysis and Nanoscience*. John Wiley & Sons, Ltd.: 2012.
4. Hunger, M.; Weitkamp, J., In situ IR, NMR, EPR, and UV/Vis spectroscopy: Tools for new insight into the mechanisms of heterogeneous catalysis. *Angewandte Chemie International Edition* **2001**, *40* (16), 2954-2971.
5. Haw, J.; Jentoft, F., In-Situ Spectroscopy in Heterogeneous Catalysis. *ANGEWANDTE CHEMIE* **2003**, *115* (3), 266-267.
6. Weckhuysen, B. M., In-situ spectroscopy of catalysts. **2004**.
7. Bañares, M. A.; Guerrero-Pérez, M. O.; Fierro, J. L. G.; Cortez, G. G., Raman spectroscopy during catalytic operations with on-line activity measurement (operando spectroscopy): a method for understanding the active centres of cations supported on porous materials. *Journal of Materials Chemistry* **2002**, *12* (11), 3337-3342.
8. Gurlo, A.; Riedel, R., In situ and operando spectroscopy for assessing mechanisms of gas sensing. *Angew Chem Int Ed Engl* **2007**, *46* (21), 3826-48.
9. Degler, D. Spectroscopic Insights in the Gas Detection Mechanism of Tin Dioxide Based Gas Sensors. Eberhard Karls Universität Tübingen, 2017.
10. Macdonald, J. R., *Impedance Spectroscopy, Theory Experiment and Applications*. Second ed.; 2005.
11. Schipani, F.; Miller, D. R.; Ponce, M. A.; Aldao, C. M.; Akbar, S. A.; Morris, P. A., Electrical Characterization of Semiconductor Oxide-Based Gas Sensors Using Impedance Spectroscopy: A Review. *Reviews in Advanced Sciences and Engineering* **2016**, *5* (1), 86-105.
12. Balasubramani, V.; Sureshkumar, S.; Rao, T. S.; Sridhar, T. M., Impedance Spectroscopy-Based Reduced Graphene Oxide-Incorporated ZnO Composite Sensor for H₂S Investigations. *Acs Omega* **2019**, *4* (6), 9976-9982.
13. Sureshkumar, S.; Venkatachalapathy, B.; Sridhar, T. M., Enhanced H₂S gas sensing properties of Mn doped ZnO nanoparticles—an impedance spectroscopic investigation. *Materials Research Express* **2019**, *6* (7).
14. Suresh Kumar, S.; Venkatachalapathy, B.; Sujatha, L.; Subba Rao, T.; Sridhar, T. M., Influence of H₂S Concentration on Mn Sensitized Tin Dioxide Nanoparticles Based Sensor—An Impedance Spectroscopic Investigation. *Sensor Letters* **2016**, *14* (9), 949-954.
15. Al-Hardan, N.; Abdullah, M. J.; Aziz, A. A., Impedance spectroscopy of undoped and Cr-doped ZnO gas sensors under different oxygen concentrations. *Applied Surface Science* **2011**, *257* (21), 8993-8997.
16. Navale, Y. H.; Navale, S. T.; Ramgir, N. S.; Stadler, F. J.; Gupta, S. K.; Aswal, D. K.; Patil, V. B., Zinc oxide hierarchical nanostructures as potential NO₂ sensors. *Sensors and Actuators B: Chemical* **2017**, *251*, 551-563.
17. Schipani, F.; Miller, D. R.; Ponce, M. A.; Aldao, C. M.; Akbar, S. A.; Morris, P. A.; Xu, J. C., Conduction mechanisms in SnO₂ single-nanowire gas sensors: An impedance spectroscopy study. *Sensors and Actuators B: Chemical* **2017**, *241*, 99-108.
18. Balasubramani, V.; Chandraleka, S.; Rao, T. S.; Sasikumar, R.; Kuppusamy, M. R.; Sridhar, T. M., Review—Recent Advances in Electrochemical Impedance Spectroscopy Based Toxic Gas Sensors Using Semiconducting Metal Oxides. *Journal of The Electrochemical Society* **2020**, *167* (3).
19. Roduner, E., Understanding catalysis. *Chem Soc Rev* **2014**, *43* (24), 8226-39.

20. Okumura, M.; Tsubota, S.; Haruta, M., Preparation of supported gold catalysts by gas-phase grafting of gold acetylacetonate for low-temperature oxidation of CO and of H₂. *Journal of Molecular Catalysis A: Chemical* **2003**, *199* (1-2), 73-84.
21. Korotcenkov, G.; Ivanov, M.; Blinov, I.; Stetter, J. R., Kinetics of indium oxide-based thin film gas sensor response: The role of "redox" and adsorption/desorption processes in gas sensing effects. *Thin Solid Films* **2007**, *515* (7-8), 3987-3996.
22. Bharti, D. C.; Mukherjee, K.; Majumder, S. B., Wet chemical synthesis and gas sensing properties of magnesium zinc ferrite nano-particles. *Mater Chem Phys* **2010**, *120* (2-3), 509-517.
23. Fowler, J. D.; Allen, M. J.; Tung, V. C.; Yang, Y.; Kaner, R. B.; Weiller, B. H., Practical chemical sensors from chemically derived graphene. *ACS Nano* **2009**, *3* (2), 301-6.
24. Johnson, J. L.; Behnam, A.; Pearton, S. J.; Ural, A., Hydrogen sensing using pd-functionalized multi-layer graphene nanoribbon networks. *Adv Mater* **2010**, *22* (43), 4877-80.
25. Hubner, M.; Koziej, D.; Grunwaldt, J. D.; Weimar, U.; Barsan, N., An Au clusters related spill-over sensitization mechanism in SnO₂-based gas sensors identified by operando HERFD-XAS, work function changes, DC resistance and catalytic conversion studies. *Phys Chem Chem Phys* **2012**, *14* (38), 13249-54.
26. Degler, D.; Wicker, S.; Weimar, U.; Barsan, N., Identifying the Active Oxygen Species in SnO₂ Based Gas Sensing Materials: An Operando IR Spectroscopy Study. *The Journal of Physical Chemistry C* **2015**, *119* (21), 11792-11799.
27. Zappa, D.; Galstyan, V.; Kaur, N.; Munasinghe Arachchige, H. M. M.; Sisman, O.; Comini, E., "Metal oxide -based heterostructures for gas sensors"- A review. *Anal Chim Acta* **2018**, *1039*, 1-23.
28. Tang, H.; Yan, M.; Zhang, H.; Li, S.; Ma, X.; Wang, M.; Yang, D., A selective NH₃ gas sensor based on Fe₂O₃-ZnO nanocomposites at room temperature. *Sensors and Actuators B: Chemical* **2006**, *114* (2), 910-915.
29. Choi, S. W.; Park, J. Y.; Kim, S. S., Synthesis of SnO₂-ZnO core-shell nanofibers via a novel two-step process and their gas sensing properties. *Nanotechnology* **2009**, *20* (46), 465603.
30. Liang, J.; Yang, R.; Zhu, K.; Hu, M., Room temperature acetone-sensing properties of branch-like VO₂ (B)/ZnO hierarchical hetero-nanostructures. *Journal of Materials Science: Materials in Electronics* **2017**, *29* (5), 3780-3789.
31. Solis-Fernandez, P.; Bissett, M.; Ago, H., Synthesis, structure and applications of graphene-based 2D heterostructures. *Chem Soc Rev* **2017**, *46* (15), 4572-4613.
32. Schedin, F.; Geim, A. K.; Morozov, S. V.; Hill, E. W.; Blake, P.; Katsnelson, M. I.; Novoselov, K. S., Detection of individual gas molecules adsorbed on graphene. *Nat Mater* **2007**, *6* (9), 652-5.
33. Choi, Y. R.; Yoon, Y.-G.; Choi, K. S.; Kang, J. H.; Shim, Y.-S.; Kim, Y. H.; Chang, H. J.; Lee, J.-H.; Park, C. R.; Kim, S. Y.; Jang, H. W., Role of oxygen functional groups in graphene oxide for reversible room-temperature NO₂ sensing. *Carbon* **2015**, *91*, 178-187.
34. Peng, Y.; Li, J., Ammonia adsorption on graphene and graphene oxide: a first-principles study. *Frontiers of Environmental Science & Engineering* **2013**, *7* (3), 403-411.
35. Liu, X.; Ma, T.; Pinna, N.; Zhang, J., Two-Dimensional Nanostructured Materials for Gas Sensing. *Advanced Functional Materials* **2017**, *27* (37).
36. Mao, S.; Cui, S.; Lu, G.; Yu, K.; Wen, Z.; Chen, J., Tuning gas-sensing properties of reduced graphene oxide using tin oxide nanocrystals. *Journal of Materials Chemistry* **2012**, *22* (22).
37. Zhang, H.; Feng, J.; Fei, T.; Liu, S.; Zhang, T., SnO₂ nanoparticles-reduced graphene oxide nanocomposites for NO₂ sensing at low operating temperature. *Sensors and Actuators B: Chemical* **2014**, *190*, 472-478.
38. Wang, Z.; Han, T.; Fei, T.; Liu, S.; Zhang, T., Investigation of Microstructure Effect on NO₂ Sensors Based on SnO₂ Nanoparticles/Reduced Graphene Oxide Hybrids. *ACS Appl Mater Interfaces* **2018**, *10* (48), 41773-41783.

39. Tyagi, P.; Sharma, A.; Tomar, M.; Gupta, V., A comparative study of RGO-SnO₂ and MWCNT-SnO₂ nanocomposites based SO₂ gas sensors. *Sensors and Actuators B: Chemical* **2017**, *248*, 980-986.
40. Bhati, V. S.; Hojamberdiev, M.; Kumar, M., Enhanced sensing performance of ZnO nanostructures-based gas sensors: A review. *Energy Reports* **2020**, *6*, 46-62.
41. Singh, G.; Choudhary, A.; Haranath, D.; Joshi, A. G.; Singh, N.; Singh, S.; Pasricha, R., ZnO decorated luminescent graphene as a potential gas sensor at room temperature. *Carbon* **2012**, *50* (2), 385-394.
42. Huang, Q.; Zeng, D.; Li, H.; Xie, C., Room temperature formaldehyde sensors with enhanced performance, fast response and recovery based on zinc oxide quantum dots/graphene nanocomposites. *Nanoscale* **2012**, *4* (18), 5651-8.
43. Su, P. G.; Peng, S. L., Fabrication and NO₂ gas-sensing properties of reduced graphene oxide/WO₃ nanocomposite films. *Talanta* **2015**, *132*, 398-405.
44. Jeevitha, G.; Abhinayaa, R.; Mangalaraj, D.; Ponpandian, N.; Meena, P.; Mounasamy, V.; Madanagurusamy, S., Porous reduced graphene oxide (rGO)/WO₃ nanocomposites for the enhanced detection of NH₃ at room temperature. *Nanoscale Advances* **2019**, *1* (5), 1799-1811.
45. Deng, S.; Tjoa, V.; Fan, H. M.; Tan, H. R.; Sayle, D. C.; Olivo, M.; Mhaisalkar, S.; Wei, J.; Sow, C. H., Reduced graphene oxide conjugated Cu₂O nanowire mesocrystals for high-performance NO₂ gas sensor. *J Am Chem Soc* **2012**, *134* (10), 4905-17.
46. Zhang, J.; Zeng, D.; Zhao, S.; Wu, J.; Xu, K.; Zhu, Q.; Zhang, G.; Xie, C., Room temperature NO₂ sensing: what advantage does the rGO-NiO nanocomposite have over pristine NiO? *Phys Chem Chem Phys* **2015**, *17* (22), 14903-11.
47. Li, X.; Zhao, Y.; Wang, X.; Wang, J.; Gaskov, A. M.; Akbar, S. A., Reduced graphene oxide (rGO) decorated TiO₂ microspheres for selective room-temperature gas sensors. *Sensors and Actuators B: Chemical* **2016**, *230*, 330-336.
48. Luo, Y.; Zhang, C.; Zheng, B.; Geng, X.; Debliquy, M., Hydrogen sensors based on noble metal doped metal-oxide semiconductor: A review. *International Journal of Hydrogen Energy* **2017**, *42* (31), 20386-20397.
49. Su, P.-G.; Yang, L.-Y., NH₃ gas sensor based on Pd/SnO₂/RGO ternary composite operated at room-temperature. *Sensors and Actuators B: Chemical* **2016**, *223*, 202-208.
50. Peng, Y.; Zheng, L.; Zou, K.; Li, C., Enhancing performances of a resistivity-type hydrogen sensor based on Pd/SnO₂/RGO nanocomposites. *Nanotechnology* **2017**, *28* (21), 215501.
51. Sun, Y. e.; Zhang, D.; Chang, H.; Zhang, Y., Fabrication of palladium–zinc oxide–reduced graphene oxide hybrid for hydrogen gas detection at low working temperature. *Journal of Materials Science: Materials in Electronics* **2016**, *28* (2), 1667-1673.
52. Jyoti; Varma, G. D., Enhanced room temperature sensitivity of Ag-CuO nanobrick/reduced graphene oxide composite for NO₂. *Journal of Alloys and Compounds* **2019**, *806*, 1469-1480.
53. Conner, W. C.; Falconer, J. L., Spillover in Heterogeneous Catalysis. *Chemical Reviews* **1995**, *95* (3), 759-788.
54. Karim, W.; Spreafico, C.; Kleibert, A.; Gobrecht, J.; VandeVondele, J.; Ekinici, Y.; van Bokhoven, J. A., Catalyst support effects on hydrogen spillover. *Nature* **2017**, *541* (7635), 68-71.
55. Wang, H. T.; Kang, B. S.; Ren, F.; Tien, L. C.; Sadik, P. W.; Norton, D. P.; Pearton, S. J.; Lin, J., Detection of hydrogen at room temperature with catalyst-coated multiple ZnO nanorods. *Applied Physics A* **2005**, *81* (6), 1117-1119.
56. Tsang, S. C.; Bulpitt, C. D. A.; Mitchell, P. C. H.; Ramirez-Cuesta, A. J., Some new insights into the sensing mechanism of palladium promoted tin (IV) oxide sensor. *J Phys Chem B* **2001**, *105* (24), 5737-5742.
57. Li, X. S.; Li, W. Z.; Chen, Y. X.; Wang, H. L., Enhancement of Hydrogen Spillover by Surface Labile Oxygen Species on Oxidized Pt/TiO₂ Catalyst. *Catal Lett* **1995**, *32* (1-2), 31-42.

58. Degler, D.; Rank, S.; Müller, S.; Pereira de Carvalho, H. W.; Grunwaldt, J.-D.; Weimar, U.; Barsan, N., Gold-Loaded Tin Dioxide Gas Sensing Materials: Mechanistic Insights and the Role of Gold Dispersion. *ACS Sensors* **2016**, *1* (11), 1322-1329.
59. Yang, Z.; Luo, G.; Lu, Z.; Hermansson, K., Oxygen vacancy formation energy in Pd-doped ceria: a DFT+U study. *J Chem Phys* **2007**, *127* (7), 074704.
60. Jian, Y.; Hu, W.; Zhao, Z.; Cheng, P.; Haick, H.; Yao, M.; Wu, W., Gas Sensors Based on Chemi-Resistive Hybrid Functional Nanomaterials. *Nano-Micro Letters* **2020**, *12* (1).
61. Song, Z.; Wei, Z.; Wang, B.; Luo, Z.; Xu, S.; Zhang, W.; Yu, H.; Li, M.; Huang, Z.; Zang, J.; Yi, F.; Liu, H., Sensitive Room-Temperature H₂S Gas Sensors Employing SnO₂ Quantum Wire/Reduced Graphene Oxide Nanocomposites. *Chemistry of Materials* **2016**, *28* (4), 1205-1212.
62. Zou, C.; Hu, J.; Su, Y.; Shao, F.; Tao, Z.; Huo, T.; Zhou, Z.; Hu, N.; Yang, Z.; Kong, E. S.-W.; Zhang, Y., Three-Dimensional Fe₃O₄@Reduced Graphene Oxide Heterojunctions for High-Performance Room-Temperature NO₂ Sensors. *Frontiers in Materials* **2019**, *6*.
63. Han, L.; Wang, D.; Cui, J.; Chen, L.; Jiang, T.; Lin, Y., Study on formaldehyde gas-sensing of In₂O₃-sensitized ZnO nanoflowers under visible light irradiation at room temperature. *Journal of Materials Chemistry* **2012**, *22* (25).
64. Wu, C.; Zhang, J.; Wang, X.; Xie, C.; Shi, S.; Zeng, D., Effect of Heterointerface on NO₂ Sensing Properties of In-Situ Formed TiO₂ QDs-Decorated NiO Nanosheets. *Nanomaterials (Basel)* **2019**, *9* (11).
65. Wang, Z.; Gao, S.; Fei, T.; Liu, S.; Zhang, T., Construction of ZnO/SnO₂ Heterostructure on Reduced Graphene Oxide for Enhanced Nitrogen Dioxide Sensitive Performances at Room Temperature. *ACS Sens* **2019**, *4* (8), 2048-2057.
66. Staerz, A.; Gao, X.; Cetmi, F.; Ming, Z.; Weimar, U.; Zhang, T.; Barsan, N., Dominant Role of Heterojunctions in Gas Sensing with Composite Materials. *ACS Appl Mater Interfaces* **2020**, *12* (18), 21127-21132.
67. Wu, J.; Tao, K.; Guo, Y.; Li, Z.; Wang, X.; Luo, Z.; Feng, S.; Du, C.; Chen, D.; Miao, J.; Norford, L. K., A 3D Chemically Modified Graphene Hydrogel for Fast, Highly Sensitive, and Selective Gas Sensor. *Adv Sci (Weinh)* **2017**, *4* (3), 1600319.
68. Liu, W.; Xu, L.; Sheng, K.; Chen, C.; Zhou, X.; Dong, B.; Bai, X.; Zhang, S.; Lu, G.; Song, H., APTES-functionalized thin-walled porous WO₃ nanotubes for highly selective sensing of NO₂ in a polluted environment. *Journal of Materials Chemistry A* **2018**, *6* (23), 10976-10989.
69. Nair, S. S.; Illyaskutty, N.; Tam, B.; Yazaydin, A. O.; Emmerich, K.; Steudel, A.; Hashem, T.; Schöttner, L.; Wöll, C.; Kohler, H.; Gliemann, H., ZnO@ZIF-8: Gas sensitive core-shell hetero-structures show reduced cross-sensitivity to humidity. *Sensors and Actuators B: Chemical* **2020**, *304*.
70. Beauchamp, R. O., Jr.; Bus, J. S.; Popp, J. A.; Boreiko, C. J.; Andjelkovich, D. A., A critical review of the literature on hydrogen sulfide toxicity. *Crit Rev Toxicol* **1984**, *13* (1), 25-97.
71. Choi, K. J.; Jang, H. W., One-dimensional oxide nanostructures as gas-sensing materials: review and issues. *Sensors (Basel)* **2010**, *10* (4), 4083-99.
72. Solis, J. L.; Hoel, A.; Kish, L. B.; Granqvist, C. G.; Saukko, S.; Lantto, V., Gas-Sensing Properties of Nanocrystalline WO₃ Films Made by Advanced Reactive Gas Deposition. *Journal of the American Ceramic Society* **2004**, *84* (7), 1504-1508.
73. Antonik, M. D.; Schneider, J. E.; Wittman, E. L.; Snow, K.; Vetelino, J. F.; Lad, R. J., Microstructural effects in WO₃ gas-sensing films. *Thin Solid Films* **1995**, *256* (1-2), 247-252.
74. Solis, J. L.; Saukko, S.; Kish, L.; Granqvist, C. G.; Lantto, V., Semiconductor gas sensors based on nanostructured tungsten oxide. *Thin Solid Films* **2001**, *391* (2), 255-260.
75. Vuong, N. M.; Kim, D.; Kim, H., Porous Au-embedded WO₃ Nanowire Structure for Efficient Detection of CH₄ and H₂S. *Sci Rep* **2015**, *5*, 11040.
76. Wang, C.; Yin, L.; Zhang, L.; Xiang, D.; Gao, R., Metal oxide gas sensors: sensitivity and influencing factors. *Sensors (Basel)* **2010**, *10* (3), 2088-106.

77. Xue, X.; Xing, L.; Chen, Y.; Shi, S.; Wang, Y.; Wang, T., Synthesis and H₂S Sensing Properties of CuO–SnO₂ Core/Shell PN-Junction Nanorods. *The Journal of Physical Chemistry C* **2008**, *112* (32), 12157-12160.
78. Ramgir, N. S.; Goyal, C. P.; Sharma, P. K.; Goutam, U. K.; Bhattacharya, S.; Datta, N.; Kaur, M.; Debnath, A. K.; Aswal, D. K.; Gupta, S. K., Selective H₂S sensing characteristics of CuO modified WO₃ thin films. *Sensors and Actuators B: Chemical* **2013**, *188*, 525-532.
79. Park, S.; Park, S.; Jung, J.; Hong, T.; Lee, S.; Kim, H. W.; Lee, C., H₂S gas sensing properties of CuO-functionalized WO₃ nanowires. *Ceramics International* **2014**, *40* (7), 11051-11056.
80. Wang, Y.; Qu, F.; Liu, J.; Wang, Y.; Zhou, J.; Ruan, S., Enhanced H₂S sensing characteristics of CuO-NiO core-shell microspheres sensors. *Sensors and Actuators B: Chemical* **2015**, *209*, 515-523.
81. Choi, S.-W.; Katoch, A.; Kim, J.-H.; Kim, S. S., Prominent Reducing Gas-Sensing Performances of n-SnO₂ Nanowires by Local Creation of p–n Heterojunctions by Functionalization with p-Cr₂O₃ Nanoparticles. *Acs Appl Mater Inter* **2014**, *6* (20), 17723-17729.
82. Na, C. W.; Woo, H.-S.; Kim, I.-D.; Lee, J.-H., Selective detection of NO₂ and C₂H₅OH using a Co₃O₄-decorated ZnO nanowire network sensor. *Chem Commun* **2011**, *47* (18).
83. Lou, Z.; Li, F.; Deng, J.; Wang, L.; Zhang, T., Branch-like hierarchical heterostructure (alpha-Fe₂O₃/TiO₂): a novel sensing material for trimethylamine gas sensor. *ACS Appl Mater Interfaces* **2013**, *5* (23), 12310-6.
84. Lu, Q.; Liu, S.; Ren, M.; Song, L.; Zhao, G., Preparation and characterization of hollow In₂O₃/Co₃O₄ heterostructured microribbons by electrospinning process. *Journal of Sol-Gel Science and Technology* **2011**, *61* (1), 169-174.
85. Mazeina, L.; Picard, Y. N.; Prokes, S. M., Controlled Growth of Parallel Oriented ZnO Nanostructural Arrays on Ga₂O₃ Nanowires. *Crystal Growth & Design* **2009**, *9* (2), 1164-1169.
86. Mao, S.; Cui, S.; Yu, K.; Wen, Z.; Lu, G.; Chen, J., Ultrafast hydrogen sensing through hybrids of semiconducting single-walled carbon nanotubes and tin oxide nanocrystals. *Nanoscale* **2012**, *4* (4), 1275-9.
87. Xu, L.; Zheng, R.; Liu, S.; Song, J.; Chen, J.; Dong, B.; Song, H., NiO@ZnO heterostructured nanotubes: coelectrospinning fabrication, characterization, and highly enhanced gas sensing properties. *Inorg Chem* **2012**, *51* (14), 7733-40.
88. Xu, L.; Song, H.; Dong, B.; Wang, Y.; Chen, J.; Bai, X., Preparation and bifunctional gas sensing properties of porous In₂O₃-CeO₂ binary oxide nanotubes. *Inorg Chem* **2010**, *49* (22), 10590-7.
89. Wang, Y. Room Temperature Gas Sensing Using Pure and Modified Metal Oxide. University of Wisconsin-Milwaukee, 2016.
90. Kaur, M.; Jain, N.; Sharma, K.; Bhattacharya, S.; Roy, M.; Tyagi, A. K.; Gupta, S. K.; Yakhmi, J. V., Room-temperature H₂S gas sensing at ppb level by single crystal In₂O₃ whiskers. *Sensors and Actuators B: Chemical* **2008**, *133* (2), 456-461.
91. Kaur, M.; Bhattacharya, S.; Roy, M.; Deshpande, S. K.; Sharma, P.; Gupta, S. K.; Yakhmi, J. V., Growth of nanostructures of Zn/ZnO by thermal evaporation and their application for room-temperature sensing of H₂ S gas. *Applied Physics A* **2007**, *87* (1), 91-96.
92. Asad, M.; Sheikhi, M. H.; Pourfath, M.; Moradi, M., High sensitive and selective flexible H₂S gas sensors based on Cu nanoparticle decorated SWCNTs. *Sensors and Actuators B: Chemical* **2015**, *210*, 1-8.
93. Asad, M.; Sheikhi, M. H., Highly sensitive wireless H₂ S gas sensors at room temperature based on CuO-SWCNT hybrid nanomaterials. *Sensors and Actuators B: Chemical* **2016**, *231*, 474-483.
94. Tian, J.; Pan, F.; Xue, R.; Zhang, W.; Fang, X.; Liu, Q.; Wang, Y.; Zhang, Z.; Zhang, D., A highly sensitive room temperature H₂S gas sensor based on SnO₂ multi-tube arrays bio-templated from insect bristles. *Dalton Trans* **2015**, *44* (17), 7911-6.

95. Mendoza, F.; Hernández, D. M.; Makarov, V.; Febus, E.; Weiner, B. R.; Morell, G., Room temperature gas sensor based on tin dioxide-carbon nanotubes composite films. *Sensors and Actuators B: Chemical* **2014**, *190*, 227-233.
96. Cui, G.; Zhang, M.; Zou, G., Resonant tunneling modulation in quasi-2D Cu₂O/SnO₂ p-n horizontal-multi-layer heterostructure for room temperature H₂S sensor application. *Sci Rep-Uk* **2013**, *3* (1).
97. Li, Z.; Niu, X.; Lin, Z.; Wang, N.; Shen, H.; Liu, W.; Sun, K.; Fu, Y. Q.; Wang, Z., Hydrothermally synthesized CeO₂ nanowires for H₂S sensing at room temperature. *Journal of Alloys and Compounds* **2016**, *682*, 647-653.
98. Zhou, L.; Shen, F.; Tian, X.; Wang, D.; Zhang, T.; Chen, W., Stable Cu₂O nanocrystals grown on functionalized graphene sheets and room temperature H₂S gas sensing with ultrahigh sensitivity. *Nanoscale* **2013**, *5* (4), 1564-9.
99. Prabakaran Shankar, J. B. B. R., Gas sensing mechanism of metal oxides: The role of ambient atmosphere, type of semiconductor and gases - A review. *Science Letters Journal* **2015**, *4*.
100. Shao, F.; Hoffmann, M. W. G.; Prades, J. D.; Zamani, R.; Arbiol, J.; Morante, J. R.; Varechkina, E.; Rumyantseva, M.; Gaskov, A.; Giebelhaus, I.; Fischer, T.; Mathur, S.; Hernández-Ramírez, F., Heterostructured p-CuO (nanoparticle)/n-SnO₂ (nanowire) devices for selective H₂S detection. *Sensors and Actuators B: Chemical* **2013**, *181*, 130-135.
101. Wang, T.-S.; Wang, Q.-S.; Zhu, C.-L.; Ouyang, Q.-Y.; Qi, L.-H.; Li, C.-Y.; Xiao, G.; Gao, P.; Chen, Y.-J., Synthesis and enhanced H₂S gas sensing properties of α -MoO₃/CuO p-n junction nanocomposite. *Sensors and Actuators B: Chemical* **2012**, *171-172*, 256-262.
102. O'Hare, P. A. G.; Hubbard, W. N.; Johnson, G. K.; Flotow, H. E., Calorimetric measurements of the low-temperature heat capacity, standard molar enthalpy of formation at 298.15 K, and high-temperature molar enthalpy increments relative to 298.15 K of tungsten disulfide (WS₂), and the thermodynamic properties to 1500 K. *The Journal of Chemical Thermodynamics* **1984**, *16* (1), 45-59.
103. Sayago, I.; Terrado, E.; Lafuente, E.; Horrillo, M. C.; Maser, W. K.; Benito, A. M.; Navarro, R.; Urriolabeitia, E. P.; Martinez, M. T.; Gutierrez, J., Hydrogen sensors based on carbon nanotubes thin films. *Synthetic Met* **2005**, *148* (1), 15-19.
104. Sundaram, R. S.; Gómez-Navarro, C.; Balasubramanian, K.; Burghard, M.; Kern, K., Electrochemical Modification of Graphene. *Advanced Materials* **2008**, *20* (16), 3050-3053.
105. Huang, H.; Gong, H.; Chow, C. L.; Guo, J.; White, T. J.; Tse, M. S.; Tan, O. K., Low-Temperature Growth of SnO₂Nanorod Arrays and Tunable n-p-n Sensing Response of a ZnO/SnO₂Heterojunction for Exclusive Hydrogen Sensors. *Advanced Functional Materials* **2011**, *21* (14), 2680-2686.
106. Kim, J. H.; Katoch, A.; Kim, H. W.; Kim, S. S., Realization of ppm-level CO detection with exceptionally high sensitivity using reduced graphene oxide-loaded SnO₂ nanofibers with simultaneous Au functionalization. *Chem Commun (Camb)* **2016**, *52* (19), 3832-5.
107. Zeng, X. Q.; Latimer, M. L.; Xiao, Z. L.; Panuganti, S.; Welp, U.; Kwok, W. K.; Xu, T., Hydrogen gas sensing with networks of ultrasmall palladium nanowires formed on filtration membranes. *Nano Lett* **2011**, *11* (1), 262-8.
108. Koo, W. T.; Qiao, S.; Ogata, A. F.; Jha, G.; Jang, J. S.; Chen, V. T.; Kim, I. D.; Penner, R. M., Accelerating Palladium Nanowire H₂ Sensors Using Engineered Nanofiltration. *ACS Nano* **2017**, *11* (9), 9276-9285.
109. Pan, Y. T.; Yin, X.; Kwok, K. S.; Yang, H., Higher-order nanostructures of two-dimensional palladium nanosheets for fast hydrogen sensing. *Nano Lett* **2014**, *14* (10), 5953-9.
110. Hong, J.; Lee, S.; Seo, J.; Pyo, S.; Kim, J.; Lee, T., A highly sensitive hydrogen sensor with gas selectivity using a PMMA membrane-coated Pd nanoparticle/single-layer graphene hybrid. *ACS Appl Mater Interfaces* **2015**, *7* (6), 3554-61.

111. Russo, P. A.; Donato, N.; Leonardi, S. G.; Baek, S.; Conte, D. E.; Neri, G.; Pinna, N., Room-temperature hydrogen sensing with heteronanostructures based on reduced graphene oxide and tin oxide. *Angew Chem Int Ed Engl* **2012**, *51* (44), 11053-7.
112. Haidry, A. A.; Ebach-Stahl, A.; Saruhan, B., Effect of Pt/TiO₂ interface on room temperature hydrogen sensing performance of memristor type Pt/TiO₂/Pt structure. *Sensors and Actuators B: Chemical* **2017**, *253*, 1043-1054.
113. Wang, Y.; Zhao, Z.; Sun, Y.; Li, P.; Ji, J.; Chen, Y.; Zhang, W.; Hu, J., Fabrication and gas sensing properties of Au-loaded SnO₂ composite nanoparticles for highly sensitive hydrogen detection. *Sensors and Actuators B: Chemical* **2017**, *240*, 664-673.
114. Li, X.; Zhou, X.; Guo, H.; Wang, C.; Liu, J.; Sun, P.; Liu, F.; Lu, G., Design of Au@ZnO yolk-shell nanospheres with enhanced gas sensing properties. *ACS Appl Mater Interfaces* **2014**, *6* (21), 18661-7.
115. Katoch, A.; Byun, J.-H.; Choi, S.-W.; Kim, S. S., One-pot synthesis of Au-loaded SnO₂ nanofibers and their gas sensing properties. *Sensors and Actuators B: Chemical* **2014**, *202*, 38-45.
116. Cabot, A.; Arbiol, J.; Morante, J. R.; Weimar, U.; Barsan, N.; Gopel, W., Analysis of the noble metal catalytic additives introduced by impregnation of as obtained SnO₂ sol-gel nanocrystals for gas sensors. *Sensor Actuat B-Chem* **2000**, *70* (1-3), 87-100.
117. Wang, C.-T.; Chen, H.-Y.; Chen, Y.-C., Gold/vanadium-tin oxide nanocomposites prepared by co-precipitation method for carbon monoxide gas sensors. *Sensors and Actuators B: Chemical* **2013**, *176*, 945-951.
118. Korotcenkov, G.; Brinzari, V.; Gulina, L. B.; Cho, B. K., The influence of gold nanoparticles on the conductivity response of SnO₂-based thin film gas sensors. *Applied Surface Science* **2015**, *353*, 793-803.
119. Chang, J. B.; Pu, H. H.; Wells, S. A.; Shi, K. Y.; Guo, X. R.; Zhou, G. H.; Sui, X. Y.; Ren, R.; Mao, S.; Chen, Y. T.; Hersam, M. C.; Chen, J. H., Semi-quantitative design of black phosphorous field-effect transistor sensors for heavy metal ion detection in aqueous media. *Mol Syst Des Eng* **2019**, *4* (3), 491-502.
120. Wang, Z.; Zhang, Y.; Liu, S.; Zhang, T., Preparation of Ag nanoparticles-SnO₂ nanoparticles-reduced graphene oxide hybrids and their application for detection of NO₂ at room temperature. *Sensors and Actuators B: Chemical* **2016**, *222*, 893-903.
121. Wang, L.; Wang, D.; Dong, Z.; Zhang, F.; Jin, J., Interface chemistry engineering for stable cycling of reduced GO/SnO₂ nanocomposites for lithium ion battery. *Nano Lett* **2013**, *13* (4), 1711-6.
122. Wang, S.; Zhao, Y.; Huang, J.; Wang, Y.; Ren, H.; Wu, S.; Zhang, S.; Huang, W., Low-temperature CO gas sensors based on Au/SnO₂ thick film. *Applied Surface Science* **2007**, *253* (6), 3057-3061.
123. Pei, S.; Cheng, H.-M., The reduction of graphene oxide. *Carbon* **2012**, *50* (9), 3210-3228.
124. Venkatesan, A.; Rathi, S.; Lee, I. Y.; Park, J.; Lim, D.; Kang, M.; Joh, H. I.; Kim, G. H.; Kannan, E. S., Molybdenum disulfide nanoparticles decorated reduced graphene oxide: highly sensitive and selective hydrogen sensor. *Nanotechnology* **2017**, *28* (36), 365501.
125. Palmisano, V.; Weidner, E.; Boon-Brett, L.; Bonato, C.; Harskamp, F.; Moretto, P.; Post, M. B.; Burgess, R.; Rivkin, C.; Buttner, W. J., Selectivity and resistance to poisons of commercial hydrogen sensors. *International Journal of Hydrogen Energy* **2015**, *40* (35), 11740-11747.
126. Hübert, T.; Boon-Brett, L.; Black, G.; Banach, U., Hydrogen sensors – A review. *Sensors and Actuators B: Chemical* **2011**, *157* (2), 329-352.
127. Ruhland, B.; Becker, T.; Muller, G., Gas-kinetic interactions of nitrous oxides with SnO₂ surfaces. *Sensor Actuat B-Chem* **1998**, *50* (1), 85-94.
128. Cui, S. M.; Pu, H. H.; Lu, G. H.; Wen, Z. H.; Mattson, E. C.; Hirschmugl, C.; Gajdardziska-Josifovska, M.; Weinert, M.; Chen, J. H., Fast and Selective Room-Temperature Ammonia Sensors Using Silver Nanocrystal-Functionalized Carbon Nanotubes. *Acs Appl Mater Inter* **2012**, *4* (9), 4898-4904.
129. Zhang, D.; Sun, Y. e.; Jiang, C.; Zhang, Y., Room temperature hydrogen gas sensor based on palladium decorated tin oxide/molybdenum disulfide ternary hybrid via hydrothermal route. *Sensors and Actuators B: Chemical* **2017**, *242*, 15-24.

130. Asama N. Naje, A. S. N., Abdulla M. Suhail, Preparation and Characterization of SnO₂ Nanoparticles. *Int. J. Innov. Res. Sci. Eng. Technol* **2013**, 12, 7068-7072.
131. Bo, Z.; Yuan, M.; Mao, S.; Chen, X.; Yan, J.; Cen, K., Decoration of vertical graphene with tin dioxide nanoparticles for highly sensitive room temperature formaldehyde sensing. *Sensors and Actuators B: Chemical* **2018**, 256, 1011-1020.
132. Lu, G.; Ocola, L. E.; Chen, J., Room-Temperature Gas Sensing Based on Electron Transfer between Discrete Tin Oxide Nanocrystals and Multiwalled Carbon Nanotubes. *Advanced Materials* **2009**, 21 (24), 2487-2491.
133. Nugroho, F. A. A.; Darmadi, I.; Cusinato, L.; Susarrey-Arce, A.; Schreuders, H.; Bannenberg, L. J.; da Silva Fanta, A. B.; Kадkhodazadeh, S.; Wagner, J. B.; Antosiewicz, T. J.; Hellman, A.; Zhdanov, V. P.; Dam, B.; Langhammer, C., Metal-polymer hybrid nanomaterials for plasmonic ultrafast hydrogen detection. *Nat Mater* **2019**, 18 (5), 489-495.
134. Tyagi, P.; Sharma, A.; Tomar, M.; Gupta, V., Metal oxide catalyst assisted SnO₂ thin film based SO₂ gas sensor. *Sensors and Actuators B: Chemical* **2016**, 224, 282-289.
135. Tyagi, P.; Sharma, A.; Tomar, M.; Gupta, V., SnO₂ thin film sensor having NiO catalyst for detection of SO₂ gas with improved response characteristics. *Sensors and Actuators B: Chemical* **2017**, 248, 998-1005.
136. Lee, S. C.; Hwang, B. W.; Lee, S. J.; Choi, H. Y.; Kim, S. Y.; Jung, S. Y.; Ragupathy, D.; Lee, D. D.; Kim, J. C., A novel tin oxide-based recoverable thick film SO₂ gas sensor promoted with magnesium and vanadium oxides. *Sensors and Actuators B: Chemical* **2011**, 160 (1), 1328-1334.
137. Kumar, R.; Avasthi, D. K.; Kaur, A., Fabrication of chemiresistive gas sensors based on multistep reduced graphene oxide for low parts per million monitoring of sulfur dioxide at room temperature. *Sensors and Actuators B: Chemical* **2017**, 242, 461-468.
138. Zhang, D.; Liu, J.; Jiang, C.; Li, P.; Sun, Y. e., High-performance sulfur dioxide sensing properties of layer-by-layer self-assembled titania-modified graphene hybrid nanocomposite. *Sensors and Actuators B: Chemical* **2017**, 245, 560-567.
139. Chen, A.; Liu, R.; Peng, X.; Chen, Q.; Wu, J., 2D Hybrid Nanomaterials for Selective Detection of NO₂ and SO₂ Using "Light On and Off" Strategy. *ACS Appl Mater Interfaces* **2017**, 9 (42), 37191-37200.
140. Zhang, D.; Wu, J.; Li, P.; Cao, Y., Room-temperature SO₂ gas-sensing properties based on a metal-doped MoS₂ nanoflower: an experimental and density functional theory investigation. *Journal of Materials Chemistry A* **2017**, 5 (39), 20666-20677.
141. Li, Q.; Wu, J.; Huang, L.; Gao, J.; Zhou, H.; Shi, Y.; Pan, Q.; Zhang, G.; Du, Y.; Liang, W., Sulfur dioxide gas-sensitive materials based on zeolitic imidazolate framework-derived carbon nanotubes. *Journal of Materials Chemistry A* **2018**, 6 (25), 12115-12124.
142. Nisar, J.; Topalian, Z.; De Sarkar, A.; Osterlund, L.; Ahuja, R., TiO₂-based gas sensor: a possible application to SO₂. *ACS Appl Mater Interfaces* **2013**, 5 (17), 8516-22.
143. Rong, X.; Chen, D.; Qu, G.; Li, T.; Zhang, R.; Sun, J., Effects of graphene on the microstructures of SnO₂@rGO nanocomposites and their formaldehyde-sensing performance. *Sensors and Actuators B: Chemical* **2018**, 269, 223-237.
144. Zhang, J.; Wu, J.; Wang, X.; Zeng, D.; Xie, C., Enhancing room-temperature NO₂ sensing properties via forming heterojunction for NiO-rGO composited with SnO₂ nanoplates. *Sensors and Actuators B: Chemical* **2017**, 243, 1010-1019.
145. Yuan, Y.; Wang, Y.; Wang, M.; Liu, J.; Pei, C.; Liu, B.; Zhao, H.; Liu, S.; Yang, H., Effect of Unsaturated Sn Atoms on Gas-Sensing Property in Hydrogenated SnO₂ Nanocrystals and Sensing Mechanism. *Sci Rep* **2017**, 7 (1), 1231.
146. Ngo, Y.-L. T.; Hur, S. H., Low-temperature NO₂ gas sensor fabricated with NiO and reduced graphene oxide hybrid structure. *Mater Res Bull* **2016**, 84, 168-176.

147. Zhang, D.; Tong, J.; Xia, B., Humidity-sensing properties of chemically reduced graphene oxide/polymer nanocomposite film sensor based on layer-by-layer nano self-assembly. *Sensors and Actuators B: Chemical* **2014**, *197*, 66-72.
148. Park, S. Y.; Lee, J. E.; Kim, Y. H.; Kim, J. J.; Shim, Y.-S.; Kim, S. Y.; Lee, M. H.; Jang, H. W., Room temperature humidity sensors based on rGO/MoS₂ hybrid composites synthesized by hydrothermal method. *Sensors and Actuators B: Chemical* **2018**, *258*, 775-782.
149. Yu, X.; Chen, X.; Ding, X.; Chen, X.; Yu, X.; Zhao, X., High-sensitivity and low-hysteresis humidity sensor based on hydrothermally reduced graphene oxide/nanodiamond. *Sensors and Actuators B: Chemical* **2019**, *283*, 761-768.
150. Park, S. Y.; Kim, Y. H.; Lee, S. Y.; Sohn, W.; Lee, J. E.; Kim, D. H.; Shim, Y.-S.; Kwon, K. C.; Choi, K. S.; Yoo, H. J.; Suh, J. M.; Ko, M.; Lee, J.-H.; Lee, M. J.; Kim, S. Y.; Lee, M. H.; Jang, H. W., Highly selective and sensitive chemoresistive humidity sensors based on rGO/MoS₂ van der Waals composites. *Journal of Materials Chemistry A* **2018**, *6* (12), 5016-5024.
151. Zhao, X.; Long, Y.; Yang, T.; Li, J.; Zhu, H., Simultaneous High Sensitivity Sensing of Temperature and Humidity with Graphene Woven Fabrics. *ACS Appl Mater Interfaces* **2017**, *9* (35), 30171-30176.
152. Kim, H.-R.; Haensch, A.; Kim, I.-D.; Barsan, N.; Weimar, U.; Lee, J.-H., The Role of NiO Doping in Reducing the Impact of Humidity on the Performance of SnO₂-Based Gas Sensors: Synthesis Strategies, and Phenomenological and Spectroscopic Studies. *Advanced Functional Materials* **2011**, *21* (23), 4456-4463.
153. Wu, J.; Wu, Z.; Ding, H.; Wei, Y.; Huang, W.; Yang, X.; Li, Z.; Qiu, L.; Wang, X., Three-Dimensional Graphene Hydrogel Decorated with SnO₂ for High-Performance NO₂ Sensing with Enhanced Immunity to Humidity. *ACS Appl Mater Interfaces* **2020**.
154. Wang, Z.; Huang, L.; Chi, L., Organic Semiconductor Field-Effect Transistors Based on Organic-2D Heterostructures. *Frontiers in Materials* **2020**, *7*.
155. Zhou, J.; Lin, H.; Cheng, X.-F.; Shu, J.; He, J.-H.; Li, H.; Xu, Q.-F.; Li, N.-J.; Chen, D.-Y.; Lu, J.-M., Ultrasensitive and robust organic gas sensors through dual hydrogen bonding. *Materials Horizons* **2019**, *6* (3), 554-562.
156. Chang, J. B.; Liu, V.; Subramanian, V.; Sivula, K.; Luscombe, C.; Murphy, A.; Liu, J.; Fréchet, J. M. J., Printable polythiophene gas sensor array for low-cost electronic noses. *Journal of Applied Physics* **2006**, *100* (1).
157. Husain, A.; Ahmad, S.; Mohammad, F., Synthesis, characterisation and ethanol sensing application of polythiophene/graphene nanocomposite. *Mater Chem Phys* **2020**, *239*.
158. Tsai, M.-S.; Su, P.-G.; Lu, C.-J., Fabrication of a highly sensitive flexible humidity sensor based on Pt/polythiophene/reduced graphene oxide ternary nanocomposite films using a simple one-pot method. *Sensors and Actuators B: Chemical* **2020**, *324*.
159. Bai, S.; Guo, J.; Sun, J.; Tang, P.; Chen, A.; Luo, R.; Li, D., Enhancement of NO₂-Sensing Performance at Room Temperature by Graphene-Modified Polythiophene. *Industrial & Engineering Chemistry Research* **2016**, *55* (19), 5788-5794.
160. Wagner, J.; Jang, H.-J.; Han, J.; Katz, H. E., Enhanced and unconventional responses in chemiresistive sensing devices for nitrogen dioxide and ammonia from carboxylated alkylthiophene polymers. *Materials Horizons* **2020**, *7* (5), 1358-1371.
161. Hu, W.; Wan, L.; Jian, Y.; Ren, C.; Jin, K.; Su, X.; Bai, X.; Haick, H.; Yao, M.; Wu, W., Electronic Noses: From Advanced Materials to Sensors Aided with Data Processing. *Advanced Materials Technologies* **2018**.
162. Marco, S.; Gutierrez-Galvez, A., Signal and Data Processing for Machine Olfaction and Chemical Sensing: A Review. *IEEE Sensors Journal* **2012**, *12* (11), 3189-3214.
163. Wang, B.; Huynh, T. P.; Wu, W.; Hayek, N.; Do, T. T.; Cancilla, J. C.; Torrecilla, J. S.; Nahid, M. M.; Colwell, J. M.; Gazit, O. M.; Puniredd, S. R.; McNeill, C. R.; Sonar, P.; Haick, H., A Highly Sensitive

Diketopyrrolopyrrole-Based Ambipolar Transistor for Selective Detection and Discrimination of Xylene Isomers. *Adv Mater* **2016**, 28 (21), 4012-8.

164. Nallon, E. C.; Schnee, V. P.; Bright, C.; Polcha, M. P.; Li, Q., Chemical Discrimination with an Unmodified Graphene Chemical Sensor. *ACS Sensors* **2015**, 1 (1), 26-31.

165. Jang, J. S.; Lee, S. E.; Choi, S. J.; Koo, W. T.; Kim, D. H.; Shin, H.; Park, H. J.; Kim, I. D., Heterogeneous, Porous 2D Oxide Sheets via Rapid Galvanic Replacement: Toward Superior HCHO Sensing Application. *Advanced Functional Materials* **2019**, 29 (42).

166. Zhang, C.; Chen, P.; Hu, W., Organic field-effect transistor-based gas sensors. *Chem Soc Rev* **2015**, 44 (8), 2087-107.

167. Koch, N.; Elschner, A.; Schwartz, J.; Kahn, A., Organic molecular films on gold versus conducting polymer: Influence of injection barrier height and morphology on current–voltage characteristics. *Applied Physics Letters* **2003**, 82 (14), 2281-2283.

168. Bürgi, L.; Richards, T. J.; Friend, R. H.; Sirringhaus, H., Close look at charge carrier injection in polymer field-effect transistors. *Journal of Applied Physics* **2003**, 94 (9), 6129-6137.

CURRICULUM VITAE

Wang, Yale

Email Address: yalewang@uwm.edu

Education

September 2016 --- present

Ph.D., Mechanical Engineering, University of Wisconsin-Milwaukee

Dissertation Topic: Understanding Heterostructure Chemiresistive Gas Sensing at Room Temperature

Advisor: Dr. Junhong Chen

September 2015 --- May 2016

M.Sc., Mechanical Engineering, University of Wisconsin-Milwaukee

Thesis Title: Room Temperature Gas Sensing Using Pure and Modified Metal Oxide Nanowires

Advisor: Dr. Junhong Chen

September 2013 --- May 2015

Certificate in Power Engineering and Thermophysics, Chongqing University

September 2009 --- May 2013

B.Sc., Thermal Energy and Power Engineering, Yangzhou University

Research Experience

March 2020 --- Present

Intern, NanoAffix Science LLC, Milwaukee, Wisconsin

September 2016 --- May 2018, September 2020 --- May 2021

Research Assistant, Nanotechnology for Sustainable Energy and Environment Laboratory,
University of Wisconsin-Milwaukee

Teaching Experience

Teaching Assistant, Mechanical Engineering, University of Wisconsin-Milwaukee
September 2018 --- May 2020

- Conducted a lab section on course ME 110 “Engineering Fundamentals I” and taught the fundamental computer skills and CAD software Creo.
- Conducted a lab section on course ME 111 “Engineering Fundamental II” and assisted student on the teamwork mechanical projects to developed assigned products.
- Conducted a lab section on course ME 360 “Mechanical Design I” and helped students got familiar with the fundamental mechanics and kinematics.

Publications

First author

- Wang, Y., Pu, H., Lu, G., Sui, X., & Chen, J. (2021). Quantitative analysis of the synergistic effect of Au nanoparticles on SnO₂-rGO nanocomposites for room temperature hydrogen sensing. *Physical Chemistry Chemical Physics*, 23(3), 2377–2383. <https://doi.org/10.1039/d0cp05701k>
- Wang, Y., Maity, A., Sui, X., Pu, H., Mao, S., Singh, N. K., & Chen, J. (2018). In Operando Impedance Spectroscopic Analysis on NiO-WO₃ Nanorod Heterojunction Random Networks for Room-Temperature H₂S Detection. *ACS Omega*, 3(12), 18685–18693. <https://doi.org/10.1021/acsomega.8b01981>

Co-author

- 2021, “Design and Stability Improvement of Pectin-based Red Blood Cell-mimicking Microcapsules for Oxygen Therapeutics”, *Journal of Biomedical Nanotechnology*, Accepted

- Sui, X., Huang, X., Pu, H., Wang, Y., & Chen, J. (2021). Tailoring MOF-derived porous carbon nanorods confined red phosphorous for superior potassium-ion storage. *Nano Energy*, 83(January), 105797. <https://doi.org/10.1016/j.nanoen.2021.105797>
- Sui, X., Pu, H., Maity, A., Chang, J., Jin, B., Lu, G., ... Chen, J. (2020). Field-Effect Transistor Based on Percolation Network of Reduced Graphene Oxide for Real-Time ppb-Level Detection of Lead Ions in Water. *ECS Journal of Solid State Science and Technology*, 9(11), 115012. <https://doi.org/10.1149/2162-8777/abaaf4>
- Zhou, G., Jin, B., Wang, Y., Dong, Q., Maity, A., Chang, J., ... Chen, J. (2020). Ultrasensitive sensors based on aluminum oxide-protected reduced graphene oxide for phosphate ion detection in real water. *Molecular Systems Design and Engineering*, 5(5), 936–942. <https://doi.org/10.1039/c9me00156e>
- Huang, X., Sui, X., Ji, W., Wang, Y., Qu, D., & Chen, J. (2020). From phosphorus nanorods/C to yolk-shell P@hollow C for potassium-ion batteries: High capacity with stable cycling performance. *Journal of Materials Chemistry A*, 8(16), 7641–7646. <https://doi.org/10.1039/d0ta01576h>
- Johnson, D. L., Wang, Y., Stealey, S. T., Alexander, A. K., Kaltchev, M. G., Chen, J., & Zhang, W. (2020). Biosynthesis of silver nanoparticles using upland cress: Purification, characterisation, and antimicrobial activity. *Micro and Nano Letters*, 15(2), 110–113. <https://doi.org/10.1049/mnl.2019.0528>
- Cherwin, A., Namen, S., Rapacz, J., Kusik, G., Anderson, A., Wang, Y., ... Zhang, W. (2019). Design of a novel oxygen therapeutic using polymeric hydrogel microcapsules mimicking red blood cells. *Pharmaceutics*, 11(11). <https://doi.org/10.3390/pharmaceutics11110583>
- Johnson, D. L., Ziemba, R. M., Shebesta, J. H., Lipscomb, J. C., Wang, Y., Wu, Y., ... Zhang, W. (2019). Design of pectin-based bioink containing bioactive agent-loaded microspheres for bioprinting. *Biomedical Physics and Engineering Express*, 5(6). <https://doi.org/10.1088/2057-1976/ab4dbc>
- Kim, H., Huang, X., Guo, X., Wang, Y., Cui, S., Wen, Z., & Chen, J. (2019). Novel hybrid Si film/highly branched graphene nanosheets for anode materials in lithium-ion batteries. *Journal of Physics D: Applied Physics*, 52(34). <https://doi.org/10.1088/1361-6463/ab20a8>

- Ocola, L. E., Wang, Y., Divan, R., & Chen, J. (2019). Multifunctional UV and gas sensors based on vertically nanostructured zinc oxide: Volume versus surface effect. *Sensors* (Switzerland), 19(9). <https://doi.org/10.3390/s19092061>
- Ren, R., Zhao, H., Sui, X., Guo, X., Huang, X., Wang, Y., ... Chen, J. (2019). Exfoliated molybdenum disulfide encapsulated in a metal organic framework for enhanced photocatalytic hydrogen evolution. *Catalysts*, 9(1), 1–9. <https://doi.org/10.3390/catal9010089>

Honors

- Chancellor's Graduate Student Award, University of Wisconsin-Milwaukee, 2016; 2018
- Outstanding Graduate Award, Yangzhou University, 2013
- Chancellor Scholarship, Yangzhou University, 2010; 2012